Development of Cathode Air Filters for PEM Fuel Cells Using Microfibrous Entrapped Sorbents

by

Abhijeet Gajanan Phalle

A dissertation submitted to the Graduate Faculty of
Auburn University
in partial fulfillment of the
requirements for the Degree of
Doctor of Philosophy

Auburn, Alabama
December 14, 2013

Keywords: PEM Fuel Cell, Adsorptive filtration, SO_2 and NO_x removal, Microfibrous media, Composite bed

Approved by

Bruce J. Tatarchuk, Chair, Professor of Chemical Engineering
Yoon Y. Lee, Professor of Chemical Engineering
William Ashurst, Associate Professor of Chemical Engineering
Jeffrey W. Fergus, Professor of Materials Engineering

Abstract

The performance of Proton Exchange Membrane Fuel Cell (PEMFC) is degraded significantly as a result of poisoning of the cathode catalyst by trace levels of contaminants present in the cathode air. Three of the most common air contaminants present in the operating environments of PEMFC, and which have major negative effects on the performance of PEMFC, are SO_2 and NO_x (both NO and NO_2). Most of these contaminants get chemisorbed on the surface of the precious platinum catalyst layer in PEM fuel cell and this leads to decrease in the active sites available for oxygen reduction reaction on the surface of the platinum. One option to mitigate this problem is to develop contaminant tolerant electrocatalysts for PEMFC. However, developing new catalysts seems to be difficult, time consuming and possibly expensive because of the presence of a variety of contaminants in the air. Another route to solve this problem is the removal of gaseous impurities from the cathode air by adsorptive filtration. This second option appears to be more effective and cheaper. The main parameters for an adsorptive air filter are saturation capacity of the sorbents, single pass removal efficiency and pressure drop across the filter.

The research work in this dissertation thus deals with the design and construction of different configurations of adsorptive air filters that will have high adsorption capacity and high contacting efficiency for the effective removal of SO_2 and NO_x at ambient conditions. This work also involves the comparative study of the pressure drop performances of three possible configurations for the cathode air filter to select the optimal configuration of the cathode air filter for a given application.

Several sorbents impregnated with oxides of different transition metals (Zn, Cu, Mn, Ni, Fe) and caustic chemicals (like KOH) were tested for their SO_2 adsorption capacity to find out a high capacity sorbent for SO_2 removal. $MnO_x(SO_4$ route)/Al_2O_3 prepared by a deposition precipitation route with $MnSO_4$ as a precursor was found to have the highest breakthrough capacity as well as the highest saturation capacity for SO_2 removal over wide range of relative humidity (RH) and SO_2 concentrations. Effects of RH, SO_2 concentration in the challenge gas and particle size of the sorbent on the SO_2 adsorption performance of $MnO_x(SO_4$ route)/Al_2O_3 were discussed in detail. Adsorption capacity of $MnO_x(SO_4$ route)/Al_2O_3 was found to increase significantly at higher relative humidity. A working hypothesis was proposed to explain the positive effect of the moisture content on the breakthrough performance of $MnO_x(SO_4$ route)/Al_2O_3. (Chapter II)

Several sorbents supported on activated carbon as well as γ- Al_2O_3 were tested for their NO_2 adsorption performance. PICA activated carbon derived from a coconut shell showed the highest saturation capacity for NO_2 removal amongst all the sorbents tested. However generation of considerable amount of NO was also observed during NO_2 adsorption on PICA activated carbon. It was found that the surface of activated carbon partially acts as a reducing agent and converts part of NO_2 from challenge gas to NO. Addition of strong oxidizing agent like $KMnO_4/Al_2O_3$ to PICA activated carbon in the sorbent bed was found to delay the appearance of NO in the exit stream of challenge gas because of oxidation of NO to NO_2 by $KMnO_4/Al_2O_3$. Therefore, it was concluded that the mixture of three different sorbents is required for the simultaneous removal of SO_2 and NO_x from the cathode air. (Chapter III)

Microfibrous media (MFM) prepared by entrapping micron size particles in the sinter-locked network of bicomponent polymer fibers have higher contacting efficiency for removal of contaminants because of their high void fractions (> 70%) and use of smaller size particles. This microfibrous media can be pleated to accommodate many times more filter media in the same volume of filter unit. Thus microfibrous media makes it possible to construct two different configurations for the cathode air filters, namely composite bed and pleated filters. These different configurations for cathode air filters were tested for their SO_2 breakthrough capacity as well as pressure drop across them. It was found that the composite bed design increased the breakthrough capacity for SO_2 by almost 3.4 times as compared to packed bed, with little increase in the volume and pressure drop of the filter system. (Chapter IV)

Pressure drops across each of the three configurations (packed bed, composite bed and pleated filter) of cathode air filter were either found experimentally or were predicted by using model equations. Parasitic power losses were then calculated for all the three configurations of cathode air filter and all of these power losses were found to be negligible (< 0.2 W). So it was determined that the pressure drop across cathode air filter is not an important criterion for the final selection of the optimal configuration of cathode air filter. (Chapter V)

Acknowledgments

I would like to acknowledge the guidance and encouragement of my advisor Dr. Bruce Tatarchuk during this research. I would like to express my sincere gratitude to Dr. Yoon Lee, Dr. William Ashurst and Dr. Jeffrey Fergus for serving on my committee. I am grateful to Dr. Mark Barnett for his suggestions as the outside reader for this dissertation. The financial support from the US Army (TARDEC) for this research is gratefully acknowledged.

I would like to thank all current and past members of Center for Microfibrous Materials Manufacturing (CM^3); especially, Dwight Cahela, Dr. Don Cahela, Dr. Wenhua Zhu, Dr. Vivek Gaur, Mr. Ron Putt, Ms. Megan Schumacher, Ms. Kimberly Dennis, Dr. Shirish Punde, Dr. Ryan Sothen, Dr. Priyanka Dhage, Dr. Amogh Karwa, Dr. Sachin Nair, A.H.M. Hussain, Achintya Sujan among many others. I am very thankful for being associated with Dr. Hongyun Yang and Mr. Troy Barron at Intramicron Inc. and for their advice and guidance on various aspects of this work. I am grateful to Ms. Sue Allen Abner, Ms. Jennifer Harris and Ms. Karen Cochran for their administrative support. I am also thankful to Mr. Brian Scweiker for his help in the machine shop.

I am thankful to my friends in Auburn for making my stay very interesting and eventful. Special thanks go to my family and especially, my parents and my brother Satyajeet for their love and support during my graduate studies.

Table of Contents

List of Tables

List of Figures

List of Symbols

c_0 - Concentration of the challenge gas at the inlet of the reactor also denoted as C_{inlet}, ppmv

c - Concentration of the challenge gas at the exit of the reactor also referred as breakthrough concentration, ppmv

W - Weight loading of the adsorbent in the reactor, g

V - Face velocity, cm/s

D_p - Average diameter of adsorbent particles, µm

T - Temperature, ^{0}C or K

P - Pressure, Pa

ΔP - Pressure drop, Pa

ε - Void fraction of the bed, dimensionless

μ - Viscosity of the fluid

ρ - Density of the fluid

t - Time, min

t_b - Breakthrough time, min

MW - Molecular weight, g/mol

R - Universal gas constant, J/mol-K

Chapter I: Introduction and Background

I.1 Fuel Cell Technology

With the increasing worldwide consumption of fossil fuels and increasing environmental pollution, fuel cells have attracted the significant attention for a wide range of applications including automobiles, stationary power generation, uninterruptable power supplies and portable electronic products. At the beginning of the 1960s, alkaline fuel cells were used as electrical generators for Apollo space vehicles. Since then fuel cell technology has been developed and commercialized to a great extent for various civil applications. Today fuel cells are considered as environmentally friendly and high efficiency systems for the production of electricity [1]. Fuel cell operates by continuously converting the chemical energy from a fuel into electricity through a chemical reaction with oxygen or another oxidizing agent as long as both fuel and oxidant are supplied. The different fuel cell types are usually distinguished by the electrolyte that is used, though there are other important differences as well. Six classes of fuel cell have emerged as viable systems [2]. Basic information about these systems is given in table I.1.

One of the most popular types of fuel cells is Proton Exchange Membrane Fuel Cells (PEMFC) with intense focus on wide range of applications such as automobiles, uninterruptable power supplies and power source for portable electronics products. The reason for such keen interest in PEM fuel cells is because of their high power densities, low operating temperatures, quiet operation and low emissions. PEMFC works by using pure hydrogen as a fuel and water is the only byproduct as a result of reaction between hydrogen and oxygen.

Table I.1: Classification of fuel cells [2]

Fuel cell type	Mobile ion	Operating temperature	Applications
Alkaline (AFC)	OH^-	50-200°C	Used in space vehicles, e.g. Apollo
Proton exchange membrane (PEMFC)	H^+	30-100°C	Vehicles, for lower power CHP[a] systems
Direct methanol (DMFC)	H^+	20-90°C	Portable electronic systems of low power
Phosphoric acid (PAFC)	H^+	~220°C	Large number of 200-kW CHP systems
Molten Carbonate (MCFC)	CO_3^{2-}	~650°C	Medium – to large-scale CHP systems, up to MW capacity
Solid Oxide (SOFC)	O^{2-}	500-1000°C	Suitable for all sizes of CHP systems, 2kW to multi-MW

a: - CHP stands for cogeneration (or combined) heat and power

I.2 Proton Exchange Membrane Fuel Cells (PEMFC)

As mentioned earlier, a PEM fuel cell is an electrochemical cell that is fed by hydrogen, which is oxidized at the anode, and oxygen that is reduced at the cathode. The protons released during the oxidation of hydrogen are conducted through the electrolyte to the cathode. The electrolyte is an ion conduction polymer also known as the proton exchange membrane. Since the membrane is not electrically conductive, the electrons released from the hydrogen travel through a load to complete the circuit and an electric current is generated [3]. These reactions and pathways are shown schematically in figure I.1.

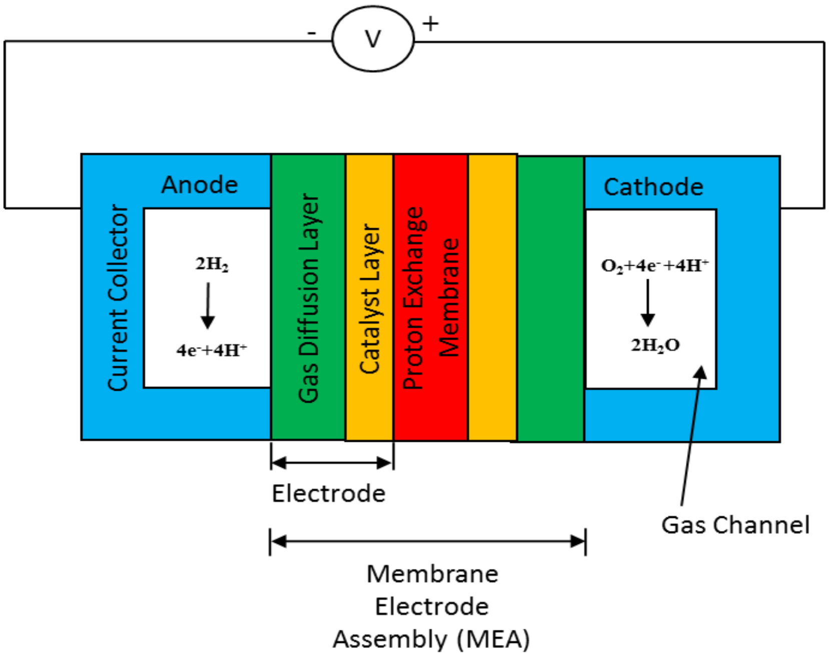

Figure I.1: Schematic of a single PEM fuel cell [3]

Both anodic and cathodic reactions in PEMFC require active catalyst sites to break the molecular bond in diatomic gaseous reactant molecules, due to low temperature operation of a PEMFC. Platinum is a good catalyst for both hydrogen oxidation reaction (HOR) and oxygen reduction reaction (ORR) at low operating temperatures of PEM fuel cell. This platinum catalyst is supported in a highly dispersed form on a conducting matrix of carbon to provide a means for electronic conduction. The electrochemical reactions taking place in the catalyst layers of PEM fuel cells are:

Hydrogen oxidation at anode: $2H_2 \longrightarrow 4H^+ + 4e^-$ $E^0 = 0.00$ V (Eq.I.1)

Oxidation reduction at cathode: $O_2 + 4H^+ + 4e^- \longrightarrow 2H_2O$ $E^0 = 1.23$ V (Eq.I.2)

Overall electrochemical reaction: $2H_2 + O_2 \longrightarrow 2H_2O$ $E_{cell} = 1.23$ V (Eq.I.3)

Where, E^0 is standard electrode potential

HOR has a relatively lower overpotential and a higher reaction rate than ORR, which leaves ORR as a source of large voltage loss in PEM fuel cell.

I.3 Effect of Air Impurities on the Performance of PEM Fuel Cell

As PEMFC technology is maturing towards large-scale commercialization; the issues of durability and reliability have become great challenges. As both polymer electrolyte membrane and platinum electrocatalyst used in PEMFC are very sensitive to chemical contamination, both fuel and oxidant supplied to PEMFC have to be of high purity. In many circumstances hydrogen for PEMFC is generated by reforming fossil fuels like natural gas or heavy hydrocarbons. This reforming process leaves many different contaminants (like CO, H_2S, COS etc.) in the hydrogen stream which must be removed before this hydrogen is supplied to the anode. There is large number of research articles available in the literature focusing on the adverse effects of fuel impurities on the PEMFC performance and purification strategies for removing these impurities.

In almost all of the PEMFC applications, an ambient air will be most likely used as a source of oxygen to make the systems economical. Beyond the required oxygen, air in an operating atmosphere may contain many impurities, such as oxides of nitrogen (NO_x which includes both NO and NO_2), carbon monoxide (CO), sulfur dioxide (SO_2), and volatile organic compounds (VOCs). The major sources of these contaminants are the automatic vehicle exhaust and industrial manufacturing processes. In special cases such as military applications, different battlefield contaminants released from both chemical warfare and normal warfare such as Sarin, sulfur mustard, cyanogen chloride, hydrogen cyanide etc. could cause significant irreversible drops in the PEMFC performance. Concentration levels of some of these air impurities can be high (few ppm for SO_2 and NO_x) for short periods of time in highly polluted environments. For a long time, cathode contamination from air impurities attracted less attention compared to anode side contamination from fuel impurities. However, in the past few years there have been growing number of studies [4-8] which are focused on the impact of such common air impurities on the performance and durability of PEMFC. Since NO_x and SO_2 are the main air pollutants, majority of published papers in the literature have emphasized the effects of these three impurities on the performance of PEMFC.

I.3.1 Effect of SO_2 on the performance of PEMFC

SO_2 resulting from fossil fuel combustion can be found in high concentration in urban areas with heavy traffic, or close to some chemical plants. SO_2 can adsorb on the platinum surface at cathode, competing with oxygen adsorption and leading to performance degradation. A trace of SO_2 can cause a significant degradation in PEMFC performance. Jing et al. [4] observed that the exposure to 1 ppm SO_2 in air for 100 hours at 70^0C at a current density of $0.5A/cm^2$ caused 35 % degradation in the cell performance with a cell voltage decrease from 0.68V to 0.44 V. The fuel cell performance degradation appears to be a function of SO_2 concentration in air stream. A 78% cell performance decrease was observed for air containing 5ppm SO_2, while a 53% decrease was observed for air containing 2.5ppm SO_2 at the same applied voltage [5].

Cyclic voltammetry (CV) study [5] revealed that there were some sulfur species on the surface of the Pt catalyst during the SO_2 poisoning process. The SO_2 adsorbed on the Pt surface was reduced electrochemically to sulfur through the formation of an SO intermediate, as shown in reactions 1.4 and 1.5 [5].

$$\mathrm{Pt} + \mathrm{SO_2} + 2\mathrm{H}^+ + 2\mathrm{e}^- \longrightarrow \mathrm{Pt\text{-}SO} + \mathrm{H_2O} \qquad \text{(Eq. I.4)}$$

$$\mathrm{Pt\text{-}SO} + 2\mathrm{H}^+ + 2\mathrm{e}^- \longrightarrow \mathrm{Pt\text{-}S} + \mathrm{H_2O} \qquad \text{(Eq. I.5)}$$

Operating a fuel cell with pure air and CV scanning after the contamination source was cut off were proven to be two ways of partially recovering the PEMFC performance [4, 5]. Performance recovery can be attributed to the electrochemical oxidation of adsorbed SO_2 at the high potential. However, complete performance recovery would not occur because the adsorbed sulfur species could not be completely desorbed by either pure air operation or CV scanning. The remaining species could still occupy the active sites of Pt electrocatalyst.

I.3.2 Effect of NO_x on the performance of PEMFC

NO_x (NO and NO_2) is one of the major air pollutants, emitted mainly from internal combustion engine vehicles. The NO_x concentration in air fluctuates, especially in an urban environment. Small amounts of NO_x can cause fuel cell performance drops. Mohtadi et al. [5] found 55% loss in current after 12 hour exposure of single PEMFC to 5 ppm NO_2. In another study [6] when NO_x concentration (NO to NO_2 ratio of 9:1) was increased from 10 to 1480 ppm, the voltage drop increased from 10% to 50%. Mohtadi et al. [5] proposed that NO_2 gets electrochemically reduced on the cathode and thus competes with O_2 for Pt sites. The product of this reduction is the formation of NH_4^+ according to reaction 1.6.

$$NO_2(g) + 8H^+ + 7e^- \longrightarrow NH_4^+ + 2H_2O \quad E^0 = +0.897 \text{ V vs. RHE} \qquad \text{(Eq. I.6)}$$

In the literature, it is generally agreed that NO_x contamination is recoverable. When the contaminant source was shut off and pure air was turned on for a certain period of time, e.g., 24 hours, fuel cell performance could be totally recovered. This recoverability reduces the concern about the NO_x contamination effect on PEMFC performance.

I.3.3 Effect of VOCs on the performance of PEMFC

VOCs (Volatile organic compounds) are a group of low-boiling-point compounds, with different chemical properties and are generally produced in the petrochemical industry, food processing, wastewater treatment etc. Another major source of VOCs is vehicle exhaust emissions. Benzene, toluene, xylene, hexane, acetone, acetaldehyde and methyl ethyl ketone are some of the examples of VOCs.

In an environment of PEMFC residential applications such as backup power supplies, some VOCs such as benzene and toluene exist due to decorative materials. For military applications, VOCs are different. In battlefields, chemical warfare can release significant amount of VOCs such as Sarin, HCN, sulfur mustard etc. [8]. Exposure to this class of VOCs was found to result in the disastrous degradation of PEMFC performance. Table I.2 gives a summary of effects of these various VOC contaminants on the PEMFC after 15 minutes of exposure, as a percentage of cell's original power output prior to the contaminant challenge [8]. These values were recorded after the exposure to these contaminants as well as after the recovery of the cell for 15 minutes by purging it with neat air free of contaminants.

Table I.2: Summary of the effects of various VOC contaminants on the fuel cell output [8]

Contaminant	Concentration	% of original output during challenge	% of original output during recovery
Benzene	50 ppm	95% (50 mA/cm^2)	95%
		93% (100 mA/cm^2)	
		72% (200 mA/cm^2)	
HCN	1780 ppm	13%	45%
Sulfur mustard	15 ppm	13%	13%
Sarin	170 ppm	30%	30%

As can be seen from table I.2, the effect of benzene contamination on cell performance is dependent on the operating current density. Fuel cell cathode contamination caused by all chemical warfare gases is catastrophic and totally unrecoverable in case of both sulfur mustard and Sarin. The mechanism of this kind of contamination is not clear. Most likely, these gases are permanently adsorbed on the Pt surface, blocking oxygen adsorption.

I.3.4 Effect of multi-contaminants on the performance of PEMFC

In real-world applications of PEMFC, ambient air contains multiple pollutants, including NO_x, SO_2, VOCs, and so forth. So, it is important to know the performance degradation of PEMFC when exposed to these muti-contaminats. In one such study reported in literature [4], the effect of mixture of 1 ppm SO_2 and 1 ppm NO_x (0.8 ppm NO_2 + 0.2 ppm NO) on the fuel cell performance is discussed. The performance obtained with these gases was found to be in the sequence of pure air > air containing 1 ppm NO_2 > air containing mixed pollutants > air containing 1 ppm SO_2. The effect of these mixed contaminants was not the sum of the effects of the individual contaminants. This phenomenon was explained by the competitive adsorption of NO_2 and SO_2 on the Pt surface, which results in the less contribution to performance degradation by SO_2 in mixed contaminants than by air containing only SO_2 [4].

I.4 Mitigation Strategies for Cathode Air Contamination

There are two main solutions to deal with the air contamination of PEMFC. First option is to develop contaminant tolerant MEA components such as electrocatalysts, membranes etc. However, because a variety of contaminants present in the air, developing new catalysts seems to be difficult, time consuming and possibly expensive. Second option is the removal of gaseous impurities from air by adsorptive filtration. This option appears to be more effective, easier and cheaper. The designing parameters of an adsorptive filter include saturation capacity, removal efficiency and pressure drop, which depend upon inlet air properties (contaminant type, concentration and air flow rate), filter design options (packed bed or pleated filter) and filter footprint (area, thickness , weight) [9]. Optimization of the filter design requires a methodology incorporating air properties, fuel cell attributes and design options.

I.5 Performance Expectations from Cathode Air Filter

1. Cathode air filter which will be developed to remove air impurities has a unique set of performance challenges. Incorporation of cathode air filter into PEM fuel cell system will result in an increase in system pressure drop due to additional pressure drop across the filter. This additional pressure drop causes an increase in the required amount of pressure-volume work that the compressor in fuel cell system has to perform. Since, this compressor is run by the power generated by the fuel cell itself, extra power needed to run the compressor with cathode air filter in place is considered as type of parasitic power loss for fuel cell system. So, pressure drop across the cathode air filter needs to be optimal to avoid parasitic power loss resulting from the use of cathode air filter being higher than power loss due to poisoning of Pt catalyst itself. An energy balance must be made between these two types of power losses.
2. Adsorbents that will be used in cathode air filter must have high breakthrough and saturation capacities for air impurities in order to extend operating life of filter.
3. Concentration of SO_2 in an ambient air can reach as high as 400 ppb [10] and that of NO_2 can go up to 500 ppb [11]. In the literature, it has been reported that 45 hours of exposure to SO_2 levels as low as 50 ppb results in 15% drop in the cell voltage. Hence, adsorbents for both SO_2 and NO_x should have high single pass removal efficiency to bring already low concentration levels of these impurities further down by one order of magnitude. If

packed bed is considered as a filter design option then the particle size of the adsorbents have to be smaller to reduce intraparticle diffusion resistance and thus to improve the contacting efficiency. However, use of such smaller particles results in much higher pressure drop as indicated by Ergun's equation (eq. I.7) for packed bed [12].

$$\frac{\Delta P}{L} = \frac{u_0}{D_p}\left(\frac{1-\varepsilon}{\varepsilon^3}\right)\left[\frac{150(1-\varepsilon)\mu}{D_p} + 1.75\rho u_0\right] \qquad \text{(Eq. I.7)}$$

where,

ΔP = Pressure drop across packed bed

L = Bed depth

u_0 = Fluid superficial velocity

ε, D_p = Voidage of the bed and Particle diameter respectively

μ, ρ = Viscosity and density of the fluid respectively

As this higher pressure drop will result in greater parasitic power loss, other filter design options which make use of small size particles (in the range of 100-200μm) and still have low pressure drop across them, such as microfibrous media (MFM) must be concerned.

4. Cathode air filter should be easily retrofitted into the existing filter slot of PEMFC system so as not to cause the expensive changes to be made in the fuel cell system just to accommodate the cathode air filter with completely different dimensions.

I.6 Microfibrous Media (MFM)

Microfibrous materials were developed and patented by CM^3 group (center for microfibrous materials manufacturing) at Auburn University. These materials consist of a sinter-locked network of micron diameter fibers made of different materials like polymer, metal or ceramic and catalyst/adsorbent particulates of smaller size (typically 100-200μm) are entrapped in this fibrous matrix (figure I.2). These materials are prepared by wet lay process of paper manufacturing and they can be made on large scale as shown in figure I.3 [13, 14]. Main features of these media are that they can be prepared with vary high voidage (up to 95%) [15] and they can be pleated easily.

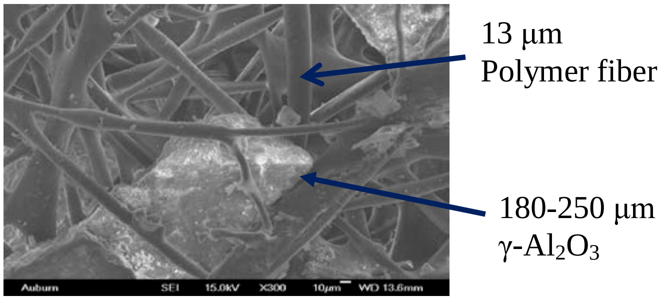

Figure I.2: SEM image of γ-Al_2O_3 entrapped in the polymer fiber matrix

Figure I.3: Large rolls of pleatable microfibrous media

These microfibrous materials are prepared by first making slurry of micro-meter diameter fibers and pulped cellulose in water and then mixing this slurry with selected adsorbent particles. This slurry is then cast into sheet known as preform by using wet lay process and this preform is then dried and thermally sintered to bond the fibers together at several contact points. Since there is no upper limit on the mass fraction of cellulose binder used in preform, sintered fiber structures with void volumes exceeding 95% can be easily obtained after sintering [15]. This high void volume of the microfibrous material reduces the intrabed heat and mass transport limitations by its ability to separate the particles resulting in reduced particle-particle contact.

Intraparticle mass transfer resistance can be reduced by decreasing the size of particles entrapped in microfibrous network.

It is known that pressure drop across any type of bed structure decreases with increase in voidage of the bed. Also, if the filter media can be pleated then many times more filter media can be accommodated in the same volume of filter unit depending on pleat factor. This increase in the filter media area in turn reduces the face velocity of air passing through the media giving lower pressure drop across pleated structure. Thus, both high voidage and pleatability features of MFM lead to their ability to use smaller size particles (~ 100-200 μm) in their structure without causing very high pressure drop across them. This ability of MFM makes them attractive design option for cathode air filter.

However, one limitation of MFM is the lower volumetric loading of adsorbent compared to a packed bed. Packed beds have high volumetric loading of sorbent (~ 60%) but have comparably lower contacting efficiency as a result of use of large size particles (~ 1 mm). On the other hand, higher contacting efficiency of MFM results in a much sharper breakthrough curve and greater sorbent utilization. These individual beneficial features of packed bed and microfibrous materials can be synergistically combined in the form a composite bed. Composite bed (figure I.5) consists of a packed bed of large size particles followed by a thin polishing layer of microfibrous media. This composite bed combines high adsorption capacity of the packed beds and high contacting efficiency of MFM in a single configuration. Bulk quantity of the contaminant is removed by the packed bed and the trace quantities of impurity breaking through the packed bed are removed efficiently by polishing layer present downstream of packed bed. This way a thinner composite bed is able to remove high logs of contaminants more efficiently than packed bed (figure I.4) alone with resulting lower pressure drop. Thus composite bed represents a more feasible design option for cathode air filter application (in which challenge gas concentrations are usually in lower ppm range) as compared to packed bed alone.

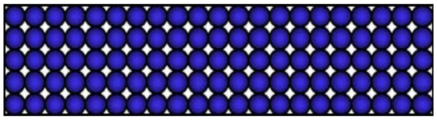

Figure I.4: Schematic of typical packed bed structure

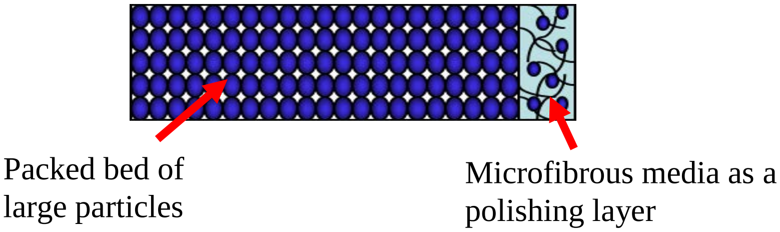

Figure I.5: Schematic of typical composite bed structure

I.7 Objectives

From the discussion so far, it was decided that the major objectives of this research work are:

1. The development of high capacity adsorbents to remove cathode air impurities, especially to remove both SO_2 and NO_x because these are the main air pollutants commonly found in many operating environments of PEMFC. Since the cathode air filter will be the first component on the cathode side of PEMFC, air at the inlet of filter will always be at ambient conditions. In most of the cases, ambient air temperature is close to room temperature and the relative humidity (RH) of ambient air can vary over a wide range (~10-90%) depending on the operating environment. Hence, the adsorbents that will be developed for cathode air filter must have high adsorption capacities at room temperature and they should retain their adsorption capacities over wide range of RH (~10-90%).

2. To incorporate these high capacity sorbents into different configurations of filters such as packed bed, composite bed and pleated filters, in order to find the optimal filter design which has high single pass and high logs removal efficiency at acceptable pressure drop.

Chapter II: Development of High Capacity Adsorbent for SO_2 Removal

II.1 Literature review

Most of the papers published in the literature on the adsorbents for SO_2 removal fall into two categories, namely SO_2 removal at high temperature (100^oC-450^oC) and low temperature (20^oC- 45^oC).

II.1.1 Adsorbents for SO_2 removal at high temperature

First category includes the studies reported on the different adsorbents for SO_2 removal at high temperature. These studies specifically focus their attention on the removal of SO_2 from combustion flue gases, for example flue gas emitted from coal-fired power plants. Temperature of such flue gas is usually in the range of 100^oC-450^oC and SO_2 concentration in the flue gas varies between 100-4000 ppm [16]. The developed technologies for emission control of SO_2 from combustion flue gases can be classified into dry and wet processes. The majority of the desulfurization processes are based on the throwaway wet scrubbing technique, using limestone as absorption agent where SO_2 is sequestered in the form of solid sulfate [17]. This wet process is quite popular because of its low capital and operating cost. But it suffers from a problem of disposal of huge amount of solid waste. Dry regenerative adsorption processes have therefore gained significant attention as the alternative to wet process. Copper oxide (CuO) dispersed on porous support such as γ-alumina has been prominently reported to be effective sorbent to remove SO_2 at such high temperatures [17, 18]. When SO_2 containing gas is brought in contact with CuO, SO_2 reacts with CuO and O_2 to form copper sulfate ($CuSO_4$) at 350-500^oC. The sulfated adsorbent can be regenerated with a reducing gas stream such as methane or carbon monoxide in the same temperature range used in the sulfation stage. Calcium oxide (CaO) sorbent dispersed both onto inorganic and carbonaceous compounds have also been reported to show significant SO_2 sorption capacity at 300°C [19].

II.1.2 Adsorbents for SO_2 removal at room temperature

Second category of published papers in the literature on the adsorbents for SO_2 removal focuses on SO_2 removal for low temperature applications such as adsorptive air filters used in buildings and automobiles. In such applications, SO_2 is required to be removed from ambient air stream which is at room temperature. Concentration of SO_2 in such ambient air stream is also usually quite low (in ppb to few ppm range). One material which has been particularly reported in the literature for SO_2 adsorption at low temperatures is activated carbon [20-27]. Activated carbon has received such significant attention because of its ability for the adsorption of many harmful gases present in low concentrations. It is due to its large surface area (~ 900-1200 m^2/g), intricate pore structure and hydrophobic features. The raw materials for activated carbon include woods such as wood chip and coconut shell, and coals such as lignite and bituminous. It has been reported that there are two types of SO_2 adsorbed on the carbon surface, one which is physically adsorbed and the other involves chemisorption of SO_2 [20-22]. In case of chemisorbed SO_2, the reaction of SO_2 with activated carbon in the presence of O_2 and H_2O at relatively low temperatures (20°C -150°C) involves a series of reactions that leads to the formation of sulfuric acid as the final product [20-22]. The quantity of chemically adsorbed SO_2 seems to be influenced by the surface groups present on the activated carbon, while the physically adsorbed SO_2 is more closely related to the general physical characteristics of the activated carbon such as surface area and pore structure [20-22, 27]. It has been concluded in many studies that in case of SO_2 adsorption on carbon, surface chemistry can be more important than the surface area and pore structure. As a result of this observation, efforts have been made to further improve the adsorption capacity of activated carbon by making its surface chemistry more favorable for SO_2 adsorption. Such improvement is carried out by impregnating the activated carbon with strategically selected chemicals. Depending on the nature of selected chemical with which porous support like activated carbon is impregnated, such adsorbents can be broadly classified into metal oxide impregnated adsorbents and basic chemical impregnated adsorbents.

In addition to activated carbon, few studies for SO_2 removal at room temperature have been reported to be carried out using γ-alumina as a porous support which is impregnated with the selected chemicals. Alumina is used as the major catalyst for the Claus process, for the oxidation of hydrogen sulfide to elemental sulfur and water using SO_2. For this reason, a number of different groups have investigated the interaction of alumina with SO_2 using infrared spectroscopy [28-30]. Karge et al. [28] observed the presence of both weakly adsorbed SO_2 and strongly adsorbed SO_2 on the surface of γ-alumina after its exposure to SO_2. Same study concluded that the interaction of SO_2 with basic sites on the surface leads to formation of chemisorbed SO_2 while adsorption at acid sites leads to the physisorbed form of $SO_{2.}$ Thus it can be seen that both acid and base sites are present on the surface of γ-alumina. In the most studies of γ-alumina supported adsorbents for SO_2 removal, γ-alumina is impregnated with the oxides of either alkali metals (Li, Na) or alkaline earth metals (Mg) [31, 32].

These types of adsorbents prepared by impregnating the porous support such as activated carbon or γ-alumina with different types of chemicals are described in the detail below.

II.1.2.1 Adsorbents impregnated with caustic chemicals

It has been reported that the basic surface groups present on activated carbon greatly enhance SO_2 adsorption [20-22]. As a result, studies on removing acidic gas like SO_2 by making the surface of activated carbon basic through impregnation of alkaline hydroxide or other such basic (same as caustic) chemicals have gained much attention. KOH is known to have excellent selective adsorption capacity for acid gases. Lee et al. [23] reported that impregnating activated carbon with 10 wt% KOH improved the adsorption capacity for SO_2 by 13.2 times. K_2CO_3 is another such basic chemical which when dispersed on activated carbon causes significant increase in the SO_2 adsorption capacity [24].

Usually, first aqueous solution of selected basic chemical is prepared and then activated carbon or some other suitable porous support is impregnated with that basic chemical by making use of incipient wetness method. Samples are then dried in an oven or under vacuum at around $100^{o}C$-$110^{o}C$ to remove the moisture and crystals of the active basic chemical are formed inside the pores of porous support. No further activation of the sample by heat treatment is needed for this group of adsorbents. Thus, preparation of this class of adsorbent involves only one heat treatment step (drying).

II.1.2.2 Adsorbents impregnated with metal oxides

It has been reported that certain metals such as iron present in the ashes of active carbons favor SO_2 sorption [26]. Studies have been reported in the literature to find out the effect of impregnating porous support such as activated carbon with different metals on SO_2 adsorption capacity. Davini [26] and Carabineiro et al. [27] both carried out SO_2 adsorption tests on activated carbon impregnated with different transition metals such as Fe, Ni, Co, Mn and Cu. These tests were performed at relatively high concentrations of SO_2 (1000-5000 ppm). At such high concentrations, all of the metal additives showed increase in SO_2 adsorption capacity to various extents with iron impregnated carbon showing the largest improvement.

Generally, aqueous solutions of salts (such as acetates or nitrates) of different metals are prepared first and then activated carbon or such other porous support is impregnated with these solutions by using incipient wetness impregnation method. These samples are then dried in an oven at 100^oC-120^oC to remove water and then they are calcined at high temperatures (~ 300^oC-500^oC) to decompose the precursor salts into the oxides of respective metals. Thus without further treatment, metal dispersed on the porous support this way is present in the metal oxide form and which is considered active for SO_2 adsorption. So, major difference in the preparation methods for basic chemical loaded sorbents and metal oxide loaded sorbents is that to prepare basic chemical loaded sorbents, second heat treatment in the form of calcination is not required.

II.1.2.3 Commercially available adsorbents from air filter manufacturers

Different types of commercial adsorbents for SO_2 removal are available in the market. These types of sorbents are usually combined with a non-woven filtration media to manufacture adsorptive air filters to remove target gaseous contaminants. However, these sorbents are sold separately also by air filter manufacturing companies such as Purafil and Camfil. Activated alumina impregnated with different wt% loadings of potassium permanganate has been found to be one of the most common commercial adsorbent for SO_2 removal. Camfil provides two such adsorbents under the trade name of Campure 4 (4 wt% $KMnO_4$) and Campure 6XL (6 wt% $KMnO_4$). Purafil also sells two such sorbents for SO_2 under the trade name of Purafil Chemisorbent (4 wt% $KMnO_4$) and Purafil Select (6 wt% $KMnO_4$). The reason for such popular use of $KMnO_4$ in commercial sorbent media can be attributed to $KMnO_4$ being a very strong oxidizing agent.

Both above-mentioned basic chemical impregnated adsorbents as well as metal oxide impregnated adsorbents were prepared in the lab and their adsorption capacities were compared for SO_2 removal. Detailed preparation methods and experimental setup used to carry out adsorption tests are mentioned in detail in next section.

II.2 Experimental Section

II.2.1 Preparation of the adsorbents

Granular Activated Carbon (PICA) obtained was derived from coconut shell and its particle size was 150-300 µm. High surface area γ-Alumina (Alfa-Aesar) was received in the form of 1/8” pellets. It was crushed in the grinder and sieved to particle size of 150-300 µm. Both these porous supports were impregnated with basic chemical KOH (Fisher Scientific) and only γ-Alumina was impregnated with $KMnO_4$ (Fisher Scientific) by using incipient wetness method. Samples were dried in convection oven at 110^oC for 7 hours. Loading of KOH on both activated carbon and and γ-Alumina was 10 wt% and that of $KMnO_4/Al_2O_3$ was 4 wt%. For Sorbents impregnated with metal oxides, γ-alumina was impregnated with nitrates of Mn, Cu, Ni, Fe, and Zn (all received from Aldrich) by using incipient wetness method. Samples were dried in convection oven at 110^oC for 7 hours and then calcined at 350^oC in air for 1 hour. In case of manganese one more sorbent was prepared by deposition-precipitation route; which was reported to have high SO_2 adsorption capacity [33, 34]. In this case, γ-alumina was impregnated with $MnSO_4$ (Sigma-Aldrich) by incipient wetness method. Sample was dried in oven at 110^oC and then it was impregnated with NaOH (Fisher Scientific) to form manganese hydroxide ($Mn (OH)_2$) inside the pores of support. After second impregnation, sample was washed with distilled water using Buckner funnel to remove Na_2SO_4 formed and any remaining traces of NaOH. Finally sample was dried in convection oven at 110^oC.

Commercial adsorbent media Campure 6XL (6 wt% $KMnO_4/Al_2O_3$) was obtained from Camfil in the form of 4×8 mesh spheres. This sorbent was then crushed in grinder and sieved to particle size range of 150-300 µm. This sorbent was also tested for SO_2 adsorption and its SO_2 breakthrough performance was then compared with the lab-prepared sorbents.

II.2.2 Characterization of supports

As described in the previous section, both activated carbon (PICA) and γ-Alumina were used as porous support in the preparation of adsorbents for SO_2 removal. The specific surface area and pore volume of both these supports were determined by an automatic volumetric sorption analyzer (Quntachrome, Autosorb 1) using N_2 adsorption at 77 K. Prior to the measurements, the sample was outgassed at 150^oC under N_2 flow for at least 3 h. The BET surface area of the samples was calculated from the N_2 adsorption isotherm by assuming the area of a N_2 molecule to be 0.162 nm^2. The values of these textural characteristics for both the supports are shown in table II.1. Bulk density of these supports is also mentioned in table II.1. This bulk density was used to calculate the adsorption capacities of the sorbents on per unit volume basis.

Table II.1: Physical characteristics of porous supports

Adsorbent	BET surface area (m^2/g)	Total Pore volume (cc/g)	Average pore diameter (nm)	Bulk density (g/cc)
PICA Activated Carbon	1255	0.60	1.9	0.43
γ-Al_2O_3	214	0.62	11.9	0.6

II.2.3 Experimental setup

The challenge gas concentration used for the adsorption studies was in the range of 5-70 ppm SO_2 in air, with a relative humidity of 0-90%. Compressed house air was used to dilute 1% SO_2 in air stream (Airgas) to attend desired challenge gas concentrations. Flow rates of house air and 1% SO_2 in air stream were measured and controlled by using two mass flow controllers (Omega FMA-A2146 and FMA-A2404 SS). House air was passed through oil filter and particulate filter before entering the mass flow controller (MFC) in order to remove the particulate contaminants. House air was then passed through a bubbler filled with distilled and deionized water for introducing moisture in the air stream. It was confirmed with the use of digital relative humidity meter (Omega Model RH30-C) that air stream coming out of bubbler is always saturated with moisture (100% RH). With this observation and few calculations, relative humidity (RH) of this air stream was adjusted by splitting the total air flow rate between the bubbler and rotameter (Omega FL-3840 ST). This moisture laden air stream was then mixed with 1% SO_2 in air stream inside the glass chamber. This challenge gas with desired RH and SO_2 concentration was then sent to the inlet of adsorption column. The adsorption column used for the experiments was made of Pyrex tube with inside diameter (ID) of ¾″. Inside the adsorption column, the adsorbent bed was rested on the inert ceramic packing and two layers of quartz wools were placed just above and below the adsorbent bed to give a support. Challenge gas was introduced at the top of the column and its flow was downwards. SO_2 concentration in the outlet gas stream of adsorber was measured using two different multigas detectors for two different concentration ranges. These detectors were MultiRAE Plus (from RAE Systems) to measure low levels of SO_2 concentrations (0-20 ppm) and GasAlertMicro 5 (from BW Technologies by Honeywell) to measure high levels of SO_2 concentrations (0-70 ppm). Both these gas detectors use plug-in electrochemical sensors to measure SO_2 concentration. Data logging interval for both the detectors can be selected between 10 seconds to 120 seconds. Before passing the challenge gas through adsorber, it was bypassed by using three way valve to measure challenge gas concentration at the inlet of adsorption column. Experimental setup described here is shown schematically in figure II.1.

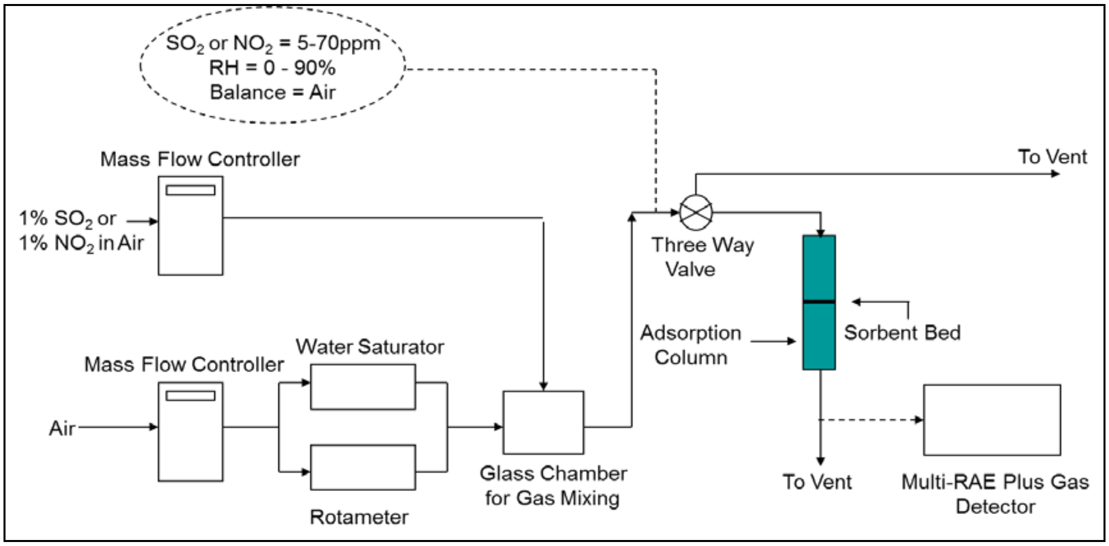

Figure II.1: Schematic of experimental setup for the breakthrough studies

II.3 Results and Discussion

SO_2 adsorption tests were carried out on both the lab prepared sorbents and the commercial sorbents in a packed bed configuration. SO_2 adsorption test was also carried out on commercial Campure 6XL sorbent for comparison purpose. All the adsorption tests were carried out under the same operating conditions to avoid the effect of change in any of these conditions affecting the SO_2 removal performance. Relative humidity of challenge gas was kept at 50% and all the tests were carried out at room temperature (~ 25^{o}C). Particle size of all the sorbents was 150-300 μm. SO_2 concentration in challenge gas was kept at 70 ppm. This concentration of SO_2 is at least one order magnitude greater than the actual concentration of SO_2 usually observed in the operating environments of PEMFC. However, such high concentration of SO_2 in the challenge gas was chosen to complete the adsorption tests of all the sorbents till their saturation points in a reasonable period of time. It is also to be noted that at this stage, all different types of sorbents were screened to find out the adsorbent with the highest adsorption capacity for SO_2. Once such adsorbent was selected, further SO_2 adsorption tests on it were carried out at lower SO_2 concentration and various RH values.

II.3.1 SO_2 adsorption tests on γ-Al_2O_3 based sorbents impregnated with metal oxides

SO_2 breakthrough curves for γ-Al_2O_3 supported metal oxide sorbents are shown in figure II.2 with the respective operating conditions.

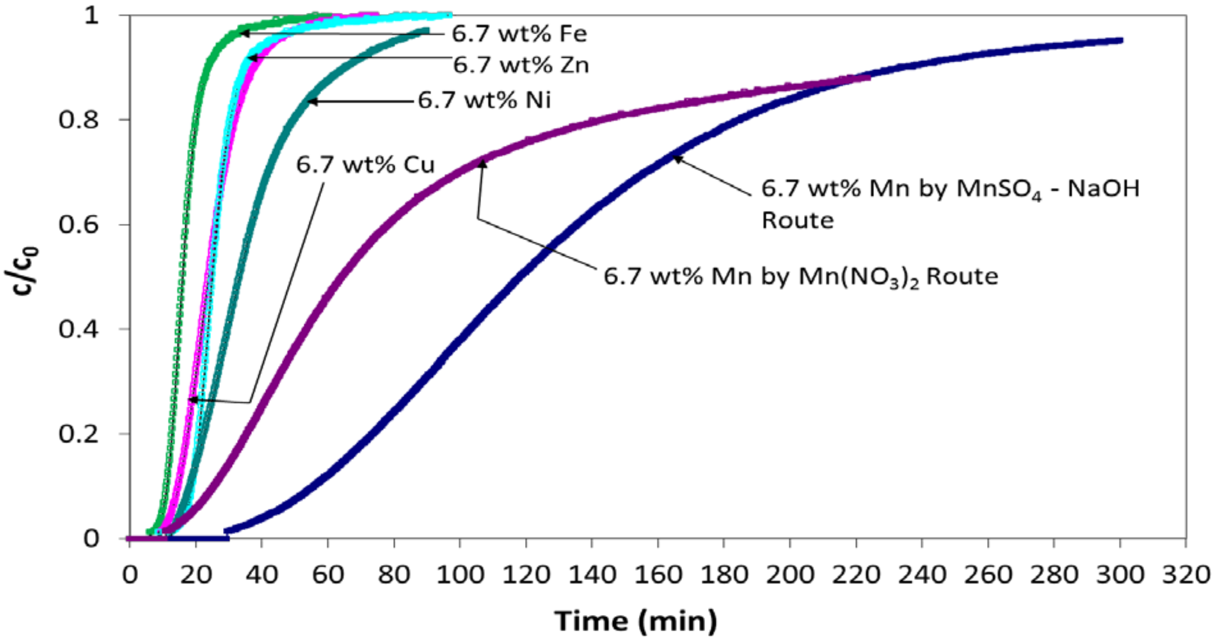

Column ID = ¾″; W = 1g; V = 50 cm/s; C_{inlet} = 70 ppm SO_2; D_p = 150-300 µm; RH = 50%; T = 25°C

Figure II.2: SO_2 breakthrough curves for γ-Al_2O_3 based sorbents impregnated with different metal oxides

Amongst all the metal oxide loaded sorbents, MnO_x/Al_2O_3 prepared by $MnSO_4$-NaOH route (denoted from here onwards as $MnO_x(SO_4$ route$)/Al_2O_3$ to distinguish it from manganese oxide loaded γ-alumina prepared by using $Mn(NO_3)_2$ as precursor which will be denoted as $MnO_x(NO_3$ route$)/Al_2O_3$) showed the highest saturation as well as the highest breakthrough capacity for SO_2. In this study, breakthrough capacity is defined as grams of SO_2 removed from the inlet gas stream per unit volume of the bed when SO_2 concentration in outlet stream (c) is 2% of challenge gas concentration (c_0) that is at c/c_0 = 2%. Breakthrough and saturation capacity of this $MnO_x(SO_4$ route$)/Al_2O_3$ was 33.7 mg of SO_2/cc and 124.1 mg of SO_2/cc respectively. Both the breakthrough capacity and the saturation capacity of all the sorbents were defined as per unit volume of sorbent bed (mg/cc) rather than per unit weight of sorbent (mg/g). This was done by considering the volume constraint that will be put on a cathode air filter in actual applications to retrofit it in the existing PEMFC system. This way adsorption capacities defined as per unit volume of bed represent the SO_2 removal performance of sorbents much better with respect to the actual design constraint of cathode air filter. The detailed calculations of this breakthrough capacity and saturation capacity are shown in appendix A.

In case of MnO_x(SO_4 route)/Al_2O_3 sorbent, x can vary between 1.5 and 2; in other words oxidation state of Mn in MnO_x(SO_4 route)/Al_2O_3 varies between 3 and 4. This is because of non-stoichiometry characteristic of most oxides of manganese; that is most oxides of manganese molecules typically contain on average less than the theoretical number of 2 oxygen atoms, with numbers more typically ranging between 1.5 to 2.0. This non-stoichiometry characteristic is thought to result from the solid-solution mixtures of two or more oxide species [35, 36]. As MnO_x(SO_4 route)/Al_2O_3 was the best performing sorbent amongst all metal oxide loaded sorbents, its capacity for SO_2 removal was next compared with sorbents impregnated with basic chemical (KOH) and $KMnO_4$ as well as with commercial Campure 6XL sorbent.

II.3.2 Comparison of SO_2 adsorption performance between MnO_x(SO_4 route)/Al_2O_3 and sorbents impregnated with KOH, $KMnO_4$

SO_2 breakthrough curves of MnO_x(SO_4 route)/Al_2O_3 and sorbents impregnated with KOH, KMnO4 are shown in figure II.3 with corresponding operating conditions. Breakthrough performance of commercial Campure 6XL sorbent (6 wt% $KMnO_4$/Al_2O_3) is also shown on the same plot for comparison purpose.

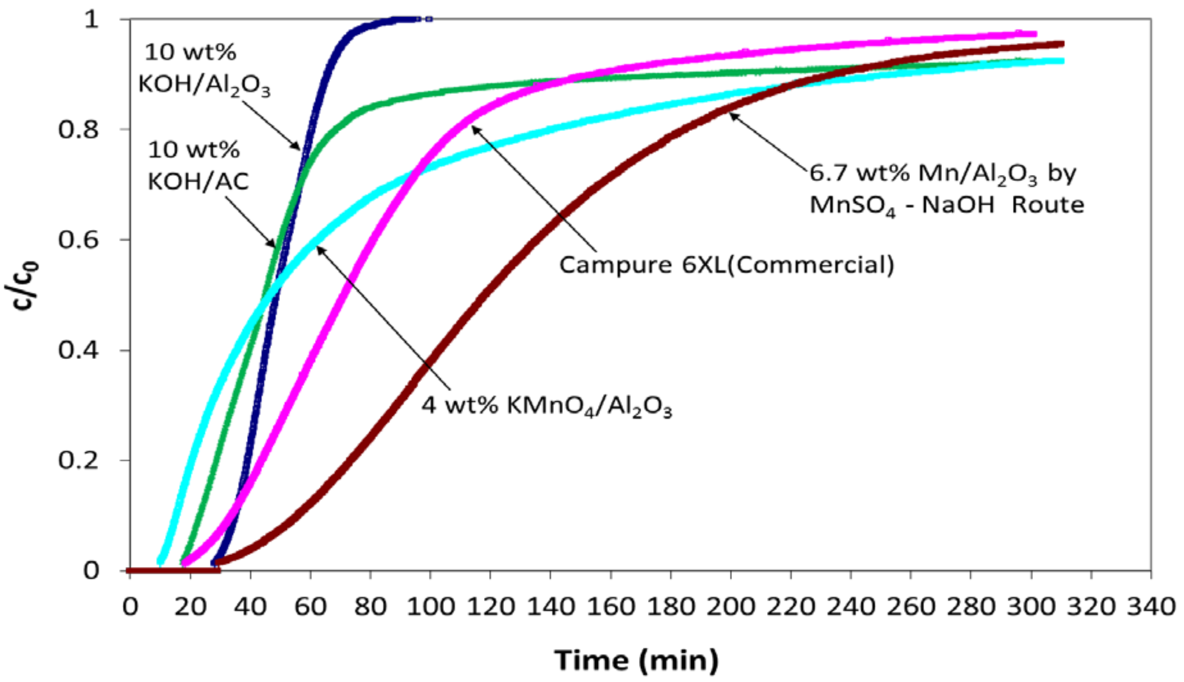

Column ID = ¾″; W = 1g; V = 50 cm/s; C_{inlet} = 70 ppm SO_2; D_p = 150-300 µm; RH = 50%; T = 25°C

Figure II.3: SO_2 breakthrough curves for MnO_x(SO_4 route)/Al_2O_3 and the sorbents impregnated with KOH, $KMnO_4$

Amongst basic chemical loaded and $KMnO_4$ loaded sorbents (including commercial Campure 6XL), KOH/Al_2O_3 showed the highest breakthrough capacity for SO_2 removal. This breakthrough capacity was almost same as that of MnO_x(SO_4 route)/Al_2O_3. However, KOH/Al_2O_3 showed much sharper breakthrough curve compared to MnO_x(SO_4 route)/Al_2O_3 and rest of the sorbents as seen in figure II.3; which indicates the fast adsorption kinetics in case of KOH/Al_2O_3. However, KOH/Al_2O_3 shows lower saturation capacity than that of MnO_x(SO_4 route)/Al_2O_3. Another observation worth mentioning here is that both breakthrough capacity and saturation capacity of MnO_x(SO_4 route)/Al_2O_3 were almost 1.5 times higher than those of commercial Campure 6XL sorbent. Breakthrough and saturation capacities of all the sorbents tested above for SO_2 removal are summarized in table II.2. All the sorbents are listed in table II.2 in the increasing order of their breakthrough capacity.

Table II.2: Adsorption capacities of the sorbents tested for SO_2 removal

Sorbents (All sorbents supported on γ-Al_2O_3)	**Breakthrough Capacity at $c/c_0=0.02$ (mg of SO_2/cc)**	**Saturation Capacity (mg of SO_2/cc)**
Fe Oxide (6.7 wt% Fe)	8.2	19.2
Cu Oxide (6.7 wt% Cu)	10.7	28.6
4 wt% $KMnO_4$	11.5	70.7
MnO_x prepared by $Mn(NO_3)_2$ Route (6.7 wt% Mn)	13.4	78
Ni Oxide (6.7 wt% Ni)	13.5	35.7
Zn Oxide (6.7 wt% Zn)	14.2	30.6
Campure 6XL commercial sorbent (6 wt% $KMnO_4$)	23.1	77.3
10 wt% KOH	29.8	52.2
MnO_x by prepared by $MnSO_4$ Route (6.7 wt% Mn)	33.7	124.1

PEM fuel cell performance has been found to be sensitive to SO_2 concentrations as low as 50 ppb [7]. Hence in real-world applications, cathode air filter should be replaced once breakthrough of gaseous impurity takes place; otherwise precious platinum electrocatalyst will get exposed to increasingly high levels of impurities. Therefore, breakthrough capacity of the adsorbent is considered to be more relevant criterion than the saturation capacity of adsorbent for its use in the cathode air filter to protect PEMFC. So taking breakthrough capacity as criterion for adsorbent selection, KOH/Al_2O_3 and MnO_x(SO_4 route)/Al_2O_3 were selected for further studies of the effects of relative humidity and concentration of SO_2 on the adsorption capacity of these sorbents.

II.3.3 Effect of relative humidity and lower SO_2 concentration on the adsorption capacity of KOH/Al_2O_3 and $MnO_x(SO_4$ route$)/Al_2O_3$

Concentration of SO_2 in many polluted environments is usually in the range of 100-400 ppb [10]. Thus, it is important to see the breakthrough performance of selected sorbents at low concentration of SO_2 to get a better idea about the SO_2 adsorption performance of these sorbents in actual operating environments of PEMFC. As cathode air filter is the first component on the cathode side of PEMFC, it will always take ambient air as an oxidant. It is known that the relative humidity of air can vary over wide range (~20-95% RH). Hence, it is also important to study the effect of varying RH on SO_2 adsorption capacity of selected sorbents.

In this study, adsorption experiments were carried out with low challenge concentration of SO_2 (5 ppm SO_2 in air) and at two different RH values (50% and 75%). Results for 50% RH and 75% RH case are shown in figure II.4 and II.5 respectively.

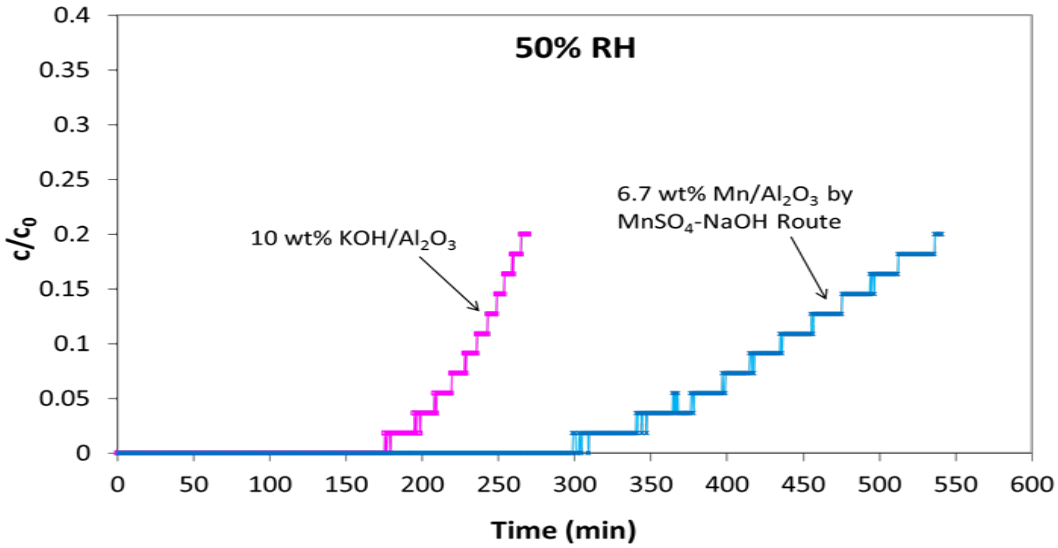

Column ID = ¾”; W = 1g; V = 100 cm/s; C_{inlet} = 5 ppm SO_2; D_p = 180-250 µm; RH = 50%; T = 25^0C

Figure II.4: SO_2 breakthrough performance of $MnO_x(SO_4$ route$)/Al_2O_3$ and KOH/Al_2O_3 for low inlet concentration of SO_2 (5 ppm) and at 50% RH

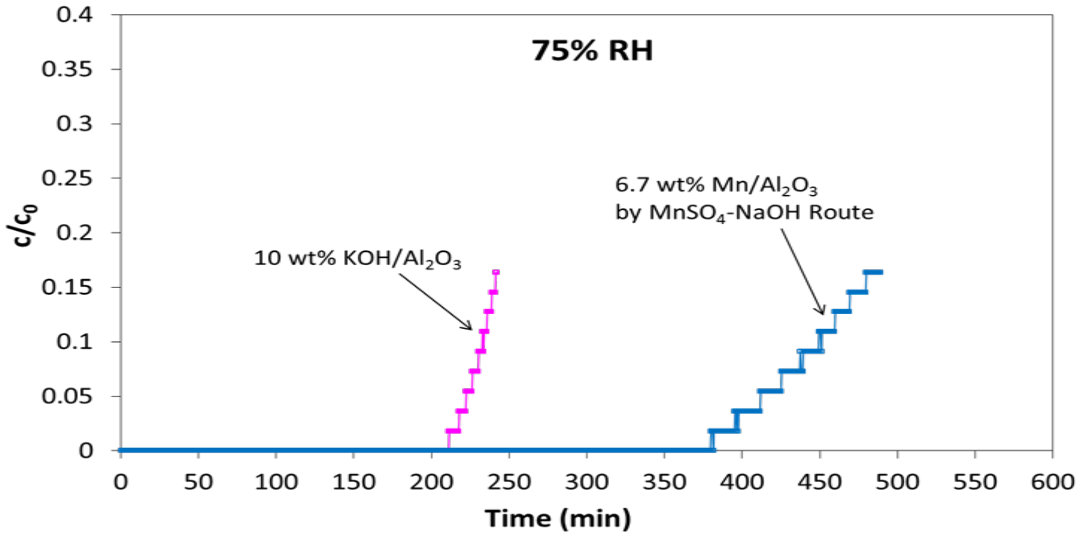

Column ID = ¾”; W = 1g; V = 100 cm/s; C_{inlet} = 5 ppm SO_2; D_p = 180-250 µm; RH = 75%; T = 25^0C

Figure II.5: SO_2 breakthrough performance of $MnO_x(SO_4$ route$)/Al_2O_3$ and KOH/Al_2O_3 for low inlet concentration of SO_2 (5 ppm) and at 75% RH

Here, breakthrough time was defined as time when concentration of SO_2 in outlet stream was 5% of the challenge gas concentration at inlet (c/c_0 = 5%). Also, breakthrough curves in both figure II.4 and figure II.5 were shown till the time when c/c_o = 0.15 to 0.2. This is because as mentioned earlier, breakthrough capacity of the sorbent was considered to be more relevant criterion at these operating conditions and so more attention was given to breakthrough times of the sorbents with focus on the initial part of the breakthrough curve. SO_2 breakthrough time of both the sorbents was found to increase significantly (~7 to 11 times) at low inlet concentration of SO_2 (5ppm) as compared to their values at high inlet SO_2 concentration (70 ppm) when relative humidity was kept constant at 50%. It is because at higher challenge concentration of gas, the driving force for adsorption is larger and hence adsorption sites get occupied by adsorbate faster causing decrease in breakthrough time of sorbent. However, it is to be noted here that when SO_2 adsorption test on 10% KOH/Al_2O_3 was carried out till saturation point for c_0 = 5ppm and 50%RH; its saturation capacity (52.4 mg SO_2/cc) was found to be almost similar to saturation capacity of the same sorbent at c_0=70 ppm and 50%RH. This shows that saturation capacity of 10% KOH/Al_2O_3 for SO_2 does not change with change in inlet SO_2 concentration in the challenge gas, although its breakthrough time was significantly increased with decrease in the SO_2 challenge concentration. This confirmed that reaction mechanism for SO_2 adsorption on KOH/Al_2O_3 did not change with change in SO_2 challenge concentration.

Referring to figure II.4, it was observed that the difference between the breakthrough times of MnO_x(SO_4 route)/Al_2O_3 (t_b=364 min, where t_b is breakthrough time) and KOH/Al_2O_3 (t_b=208 min) became much more significant at lower challenge concentration of SO_2 for the same value of RH (50%). Similar significant difference in the breakthrough times of MnO_x(SO_4 route)/Al_2O_3 (t_b=412 min) and KOH/Al_2O_3 (t_b=222 min) was also observed at c_0=5ppm and 75% RH. Moreover, breakthrough time of MnO_x(SO_4 route)/Al_2O_3 was found to be improved by almost 15%, when relative humidity of challenge gas was increased from 50% (t_b=364 min) to 75% (t_b=412 min). This indicates the positive effect of moisture on the adsorption capacity of MnO_x(SO_4 route)/Al_2O_3 for SO_2 removal.

From discussion on the SO_2 sorbents so far, MnO_x(SO_4 route)/Al_2O_3 was found to have the highest breakthrough capacity as well as the highest saturation capacity for SO_2 removal at c_0=70 ppm and 50% RH and the same sorbent showed significant improvement in its breakthrough capacity at lower SO_2 concentration of 5 ppm and at two different RH (50% and 75%). Thus it was concluded that MnO_x(SO_4 route)/Al_2O_3 showed the best performance for SO_2 adsorption over wide range of concentrations (5-70 ppm) as well as RH (50% & 75%). Hence, MnO_x(SO_4 route)/Al_2O_3 was selected as the SO_2 removal sorbent to be placed into cathode air filter.

II.3.4 Proposed mechanisms for SO_2 removal on the selected sorbents

1. Mechanism for SO_2 adsorption on KOH/Al_2O_3

In case of SO_2 adsorption on KOH/Al_2O_3, SO_2 was removed by its reaction with KOH present inside the pores of γ-Al_2O_3 support as has been reported by Lee et al. [23] in their study of SO_2 adsorption on KOH impregnated activated carbon. SO_2 removal by this reaction is more dominant than by physisorption on KOH/Al_2O_3. The reaction mechanism proposed by Lee et al. in this case is shown below.

$$2KOH + SO_2 \rightarrow K_2SO_3^* + H_2O^*$$

$$K_2SO_3^* + ½\, O_2 \rightarrow K_2SO_4^*$$

$$H_2O^* + SO_2 + ½\, O_2 \rightarrow H_2SO_4^*$$

$$2KOH + H_2SO_4^* \rightarrow K_2SO_4^* + 2H_2O^*$$

Here, * refers to the state adsorbed on the surface of porous support used.

The overall reaction between KOH and SO_2 thus can be written as shown in eq. II.1.

$$4KOH + 2SO_2 + O_2 \rightarrow 2K_2SO_4^* + 2H_2O^* \qquad \text{(Eq. II.1)}$$

Dividing above equation by 2, we get

$$2KOH + SO_2 + 1/2O_2 \rightarrow K_2SO_4^* + H_2O^* \qquad \text{(Eq. II.2)}$$

As per this reaction stoichiometry, 2 mols of KOH react with 1 mol of SO_2. Saturation capacity of 10% KOH/Al_2O_3 for SO_2 adsorption at $c_0 = 70$ ppm and 50% RH was found to be 87 mg/g. After subtracting the SO_2 saturation capacity contribution of γ-Al_2O_3 support from the total SO_2 saturation capacity of KOH/Al_2O_3, it was found that 0.48 mol of SO_2 was adsorbed per mol of KOH on this sorbent. This experimentally found value of SO_2 saturation capacity of KOH was very close to the theoretical capacity of KOH for SO_2 adsorption (0.5 mol of SO_2/mol of

KOH) as calculated from stoichiometric reaction shown in equation II.2. This shows almost complete utilization (96%) of KOH in KOH/Al_2O_3 sorbent for SO_2 removal.

Reaction shown in equation II.2 is irreversible and K_2SO_4 formed as the product is very stable. This is typical acid-base type reaction, wherein acidic SO_2 reacts easily with basic KOH present inside the pores of Al_2O_3. As KOH is a strong base, it has a high affinity for acidic gas like SO_2 and hence reaction between KOH and SO_2 is expected to take place very quickly. This explains the sharp shape of SO_2 breakthrough curve for KOH/Al_2O_3 for as seen in figure II.3.

2. Mechanism for SO_2 adsorption on MnO_x(SO_4 route)/Al_2O_3

As mentioned before, oxidation state of manganese in its oxides can vary between 3 to 4 because of non-stoichiometry characteristic of most oxides of manganese. Tikhomirov et al. [37] reported reactions between two different oxides of manganese and SO_2. These are

$MnO_2 + SO_2 \rightarrow MnSO_4$ For Mn(IV) Oxide (Eq. II.3)

$\Delta G_r = -189.3$ kJ/mol at 298 K for the above reaction II.3

$Mn_2O_3 + 2\ SO_2 + 1/2\ O_2 \rightarrow 2\ MnSO_4$ For Mn(III) Oxide (Eq. II.4)

$\Delta G_r = -216.6$ kJ/mol at 298 K for the above reaction II.4

In both the above reactions, $MnSO_4$ is the product in which Mn is present in +2 oxidation state. Thus, it can be stated that the final product of reaction between MnO_x (where x varies between 1.5 and 2) and SO_2 is always $MnSO_4$; irrespective of the oxidation state of Mn in MnO_x. Also, the change in Gibbs free energy (ΔG_r) for both the above reactions (eq.II.3 and eq. II.4) at 298 K is highly negative, suggesting that both these reactions are very spontaneous.

In the literature number of studies [38-41] have reported that the trace quantities of Mn(II) ions (in concentration $< 2.5\times10^{-5}$ M) are very active catalyst for SO_2 oxidation by using oxygen dissolved in an aqueous phase, which leads to the formation of H_2SO_4. Based on the reactions shown in eq.II.3 and eq.II.4 as well as the theory of capillary condensation, a hypothesis was proposed to explain the observed increase in the breakthrough capacity of $MnO_x(SO_4$ route)/Al_2O_3 with increase in the relative humidity from 50% RH to 75% RH. $MnSO_4$ formed as reaction product during the reaction between SO_2 and MnO_x gets dissolved in water present inside those pores of γ-Al_2O_3 where water in liquid form is present as a result of capillary condensation. This dissolved $MnSO_4$ (water solubility of 62.9 g/100 cc at 20^oC) in the form of Mn (II) ions then acts as a catalyst for SO_2 oxidation using dissolved oxygen.

The Kelvin equation relates the equilibrium vapor pressure of a liquid to the curvature of the liquid–vapour interface. It predicts that undersaturated vapors will condense in channels of sufficiently small dimensions. Thus capillary condensation occurs inside the micropores of porous support at a relative pressure below unity because the equilibrium vapor pressure over a concave surface (p) is lower than that over a plane surface (p_0) as predicted by Kelvin equation [42].Capillary condensation at a particular value of relative humidity of air occurs in all those pores which are smaller than pore radius r_k known as Kelvin radius and it is calculated by using Kelvin equation given below [42]

$$\ln\frac{p}{p_0} = \frac{-2\sigma V_m}{r_K RT} \qquad \text{(Eq. II.5)}$$

where,

V_m = Liquid molar volume

r_K = Radius of curvature or Kelvin radius

R = Universal gas constant

T = Temperature in K

σ = Surface tension

Pore size distributions of γ-Al_2O_3 and $MnO_x(SO_4$ route)/Al_2O_3 were found by using Quantachrome Autosorb-1 analyzer with N_2 as adsorbate. Desorption branch of nitrogen isotherm was used to calculate the pore size distribution of both the sorbents. Fraction of pore volume in which capillary condensation occurs was found by using Kelvin equation and with the information about pore size distribution of these two sorbents. Pore size distributions for γ-Al_2O_3 and $MnO_x(SO_4$ route)/Al_2O_3 are shown in table II.3.

Table II.3: Pore size distribution of bare γ-Al_2O_3 and $MnO_x(SO_4$ route)/Al_2O_3

γ-Al_2O_3		**$MnO_x(SO_4$ route)/Al_2O_3**	
Pore Diameter ($\overset{o}{A}$)	Cumulative Pore Volume (cc/g)	Pore Diameter ($\overset{o}{A}$)	Cumulative Pore Volume (cc/g)
18	0	18	0
23.2	0	22.9	0.002
29.2	0	28.8	0.008
36.5	0.003	36.4	0.022
46.2	0.027	46.2	0.045
61.6	0.19	61.4	0.14
89.5	0.52	89.1	0.40
156.7	0.62	160	0.53

Substituting values of σ (0.072 N/m), V_m (1.8×10^{-5} m^3/mol) for liquid water in Kelvin equation and with R = 8.314 J/mol-K and T = 298 K; it was found that around 15% of pore volume of $MnO_x(SO_4$ route)/Al_2O_3 was filled with liquid water at 75%RH because of capillary condensation, whereas almost negligible fraction of pore volume (<2%) was filled with liquid water at 50% RH. This phenomenon is shown in figure II.6.

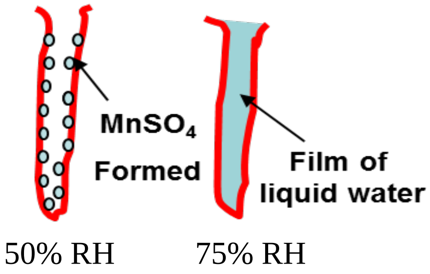

For pores with pore radius r_{pore} between Kelvin radius (r_{K}) at 50% RH and r_k at 75% RH.
$r_{k(50\%RH)} < r_{pore} < r_{k(75\%RH)}$

Figure II.6: Occurrence of the capillary condensation inside a pore of MnO_x(SO_4 route)/Al_2O_3 with the increase in relative humidity of the challenge gas

It is proposed that at 75% RH as liquid water is present in many pores (pores constituting 15% of pore volume) of MnO_x(SO_4 route)/Al_2O_3 because of capillary condensation, $MnSO_4$ formed as the product due to reaction between SO_2 and MnO_x gets dissolved in this water. These dissolved Mn(II) ions then will act as the catalyst for SO_2 oxidation by using oxygen that is dissolved in the aqueous phase and this will result in the enhanced breakthrough capacity of MnO_x(SO_4 route)/Al_2O_3 at high values of RH. This catalytic activity of dissolved Mn (II) ions can also be seen from the SO_2 breakthrough curve for MnO_x(SO_4 route)/Al_2O_3 at 75% RH and at high challenge SO_2 concentration of 70 ppm as shown in figure II.7. SO_2 breakthrough curve for 75% RH did not reach the saturation point ($c/c_0 = 1$) but got leveled at $c/c_0 = 0.48$ and concentration of SO_2 in outlet stream remained constant after that. This constant conversion of SO_2 on the sorbent is an indication of the catalytic behavior of Mn(II) ions of $MnSO_4$ dissolved in the aqueous phase.

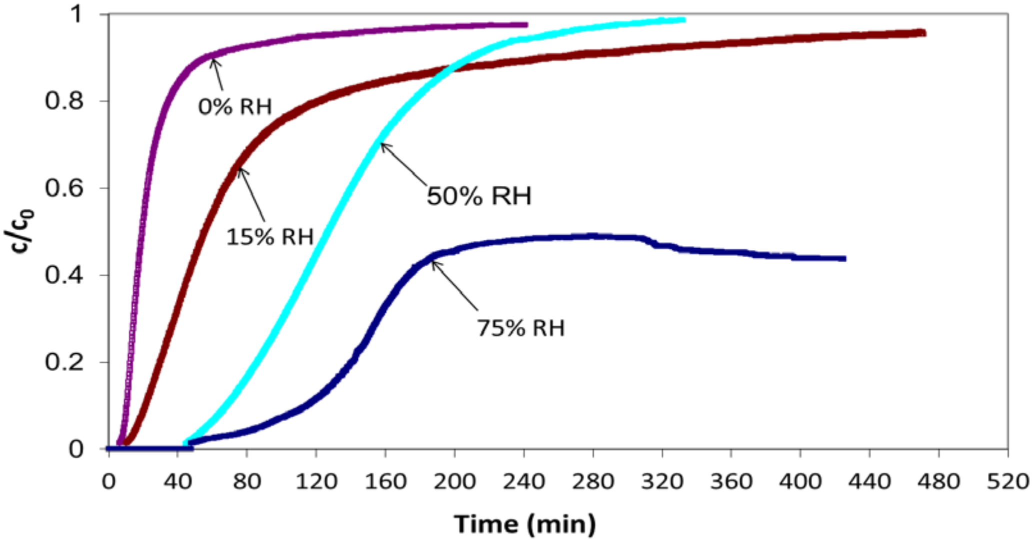

Column ID = ¾″; W = 1g; V = 50 cm/s; C_{inlet} = 70 ppm SO_2; D_p = 150-180 µm; T = 25°C

Figure II.7: SO_2 breakthrough curves for $MnO_x(SO_4$ route$)/Al_2O_3$ at different values of relative humidity (RH) of the challenge gas

II.3.5 Effect of particle size on the SO_2 breakthrough performance of $MnO_x(SO_4$ route$)/Al_2O_3$

Effect of particle size of adsorbent on the SO_2 adsorption capacity of $MnO_x(SO_4$ route$)/Al_2O_3$ was studied in order to find out whether the intraparticle diffusion resistance was significant in the adsorption of SO_2.

SO_2 breakthrough curves for the different particle sizes of $MnO_x(SO_4$ route$)/Al_2O_3$ sorbent are shown in figure II.8. It was observed that the breakthrough time increased and the breakthrough curve became sharper with decrease in the particle size of adsorbent. Two important parameters related to this observed particle size effect are the intraparticle diffusion resistance and the external surface area per unit volume of particle. As the particle size increased, both the gas film resistance and the interior diffusion path length increased, resulting in slower transfer of adsorbate from the bulk gas phase to the active sites inside the pores of sorbent. Thus larger the particle size, slower will be the diffusion of adsorbate due to relatively longer path within the adsorbent particle for adsorbate molecules to penetrate. These observations confirmed that intraparticle diffusion was the significant resistance in the overall adsorption process of SO_2 on $MnO_x(SO_4$ route$)/Al_2O_3$.

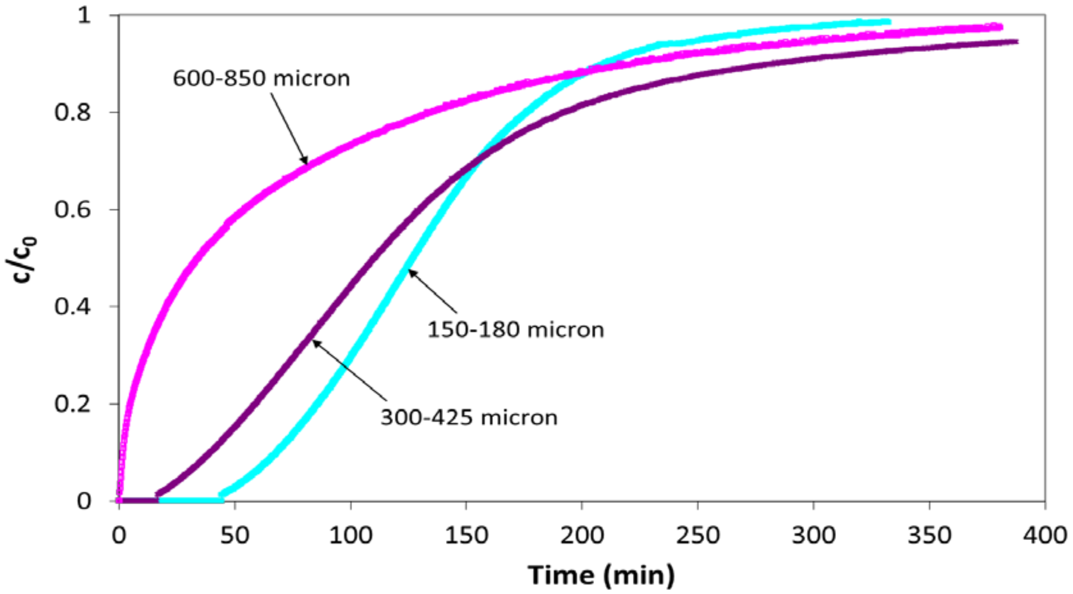

Column ID = ¾″; W = 1g; V = 50 cm/s; C_{inlet} = 70 ppm SO_2; RH = 50%; T = 25°C

Figure II.8: Effect of particle size of the sorbent on the SO_2 breakthrough performance of $MnO_x(SO_4$ route$)/Al_2O_3$

II.3.6 Effect of dilution of packed bed on the SO_2 breakthrough performance of $MnO_x(SO_4$ route$)/Al_2O_3$

Packed beds of smaller particles show increased tendency for particle cluster formation, which leads to intrabed channeling or flow maldistributions. These flow maldistributions cause an increase in axial dispersion in the packed bed of smaller particles. Bed dilution was reported to be used to mitigate the effect of axial dispersion in packed bed [43, 44]. Kalluri et al. [45] reported an increase in breakthrough time and sharpness of breakthrough curve when a packed bed of smaller particles was diluted with inerts of same particle size. In the same study it was suggested that the increase in bed dilution does not directly affect the intrabed flow misdistributions, but the resultant increase in residence time helps increase radial diffusion. This increase in radial diffusion tends to create a more uniform concentration of adsorbate across bed cross-section and thus the negative effect of flow-misdistribution is decreased, resulting in some improvement in breakthrough performance. If smaller particles of sorbent are entrapped in the polymer mictofibrous media and discs of such microfibrous media are stacked inside the adsorption column, considerable improvement in the breakthrough time and sharpness of breakthrough curve was reported for such MFM bed configuration as compared to packed bed for the same weight loading of active sorbent [45]. Such significant improvement in the breakthrough performance of MFM bed was attributed to high voidages and structural uniformity inherently present in MFM, which led to increased radial dispersion and reduced flow maldistributions in MFM bed.

From the discussion above, it was pertinent to see the effect of bed dilution on the SO_2 breakthrough performance of MnO_x(SO_4 route)/Al_2O_3 and also to compare the breakthrough performance of packed bed and stacked MFM bed for the same loading of sorbent. For this purpose, the packed bed of 180-250 microns particles of MnO_x(SO_4 route)/Al_2O_3 was diluted with the inert glass beads of same particle size (Sigma) to decrease the loading of the sorbent from 60 vol% to 20 vol%. This dilution of packed bed corresponds to bed dilution factor of 3. Bed dilution factor is the ratio of total solid volume fraction to active sorbent volume fraction. Thus the loading of active sorbent in the diluted bed was 20 vol% and that of inert glass beads was 40 vol%. Both the diluted and undiluted packed bed had the same bed voidage of 40% but diluting the bed with inerts increased the bed volume. Weight loading of MnO_x(SO_4 route)/Al_2O_3 was kept same in both the packed beds (1 g).

180-250 microns particles of γ-Al_2O_3 were entrapped in the sinter-locked network of 13 micron bicomponent polymer fibers and these γ-Al_2O_3 particles were then impregnated with MnO_x by deposition-precipitation method with $MnSO_4$ as precursor. It was calculated that 8 circular discs of 13/16″ diameter from the sheet of this MFM contain 1 g of MnO_x(SO_4 route)/Al_2O_3, which is equal to the weight loading of same sorbent in both diluted and undiluted packed beds. So 8 such discs were punched out from the sheet of polymer microfibrous media and then they were stacked in the adsorption column. Void fraction of each MFM disc was 0.79.

Both diluted and undiluted packed beds as well as MFM bed were tested at 50% RH and inlet SO_2 concentration of 70 ppm for their SO_2 breakthrough performance. Respective SO_2 breakthrough curves for all the three beds are shown in figure II.9.

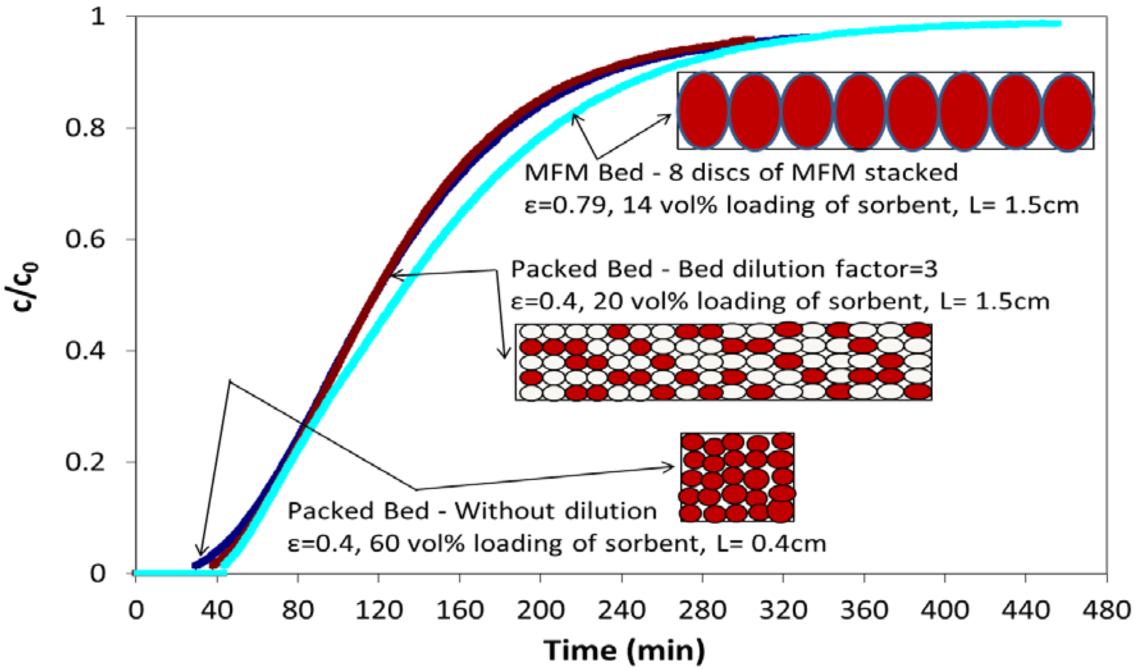

Column ID = ¾″; **W = 1g**; V = 50 cm/s; C_{inlet} = 70 ppm SO_2; D_p = 180-250 µm; RH = 50%; T = $25^{o}C$

Figure II.9: Effect of dilution of packed bed on the SO_2 breakthrough performance of MnO_x(SO_4 route)/Al_2O_3 along with SO_2 breakthrough curve for MFM bed

SO_2 breakthrough curves for diluted packed bed and undiluted packed bed were found to be almost identical as they coincide with each other in figure II.9. SO_2 breakthrough time for the diluted packed bed (t_b=41min at c/c_0=0.02) was found to be 25% higher than that for the undiluted packed bed (t_b=33min at c/c_0=0.02). However SO_2 saturation capacities for both diluted and undiluted packed bed were found to be the same (206.8 mg of SO_2/g of sorbent). SO_2 breakthrough time for the MFM bed (t_b=45min at c/c_0=0.02) was found to be 36% higher than that for the undiluted packed bed (t_b=33min at c/c_0=0.02). Also, SO_2 saturation capacity for the MFM bed (220.6 mg of SO_2/g of sorbent) was found to be 6.5% higher than that for the undiluted packed bed (206.8 mg of SO_2/g of sorbent). However shape of the SO_2 breakthrough curve for MFM bed was almost similar to that for diluted as well as undiluted packed bed.

From the discussion above, it can be confirmed that for the same weight of active sorbent (1 g), both MFM bed and diluted packed bed showed increase in the SO_2 breakthrough time as compared to undiluted packed bed. This observation was in agreement with the trend reported in the similar kind of study available in literature [45]. However improvement in the sharpness of breakthrough curves for both diluted packed bed and MFM bed was not observed when compared to undiluted packed bed. This led to the conclusion that the adsorption rates of SO_2 in all these three different beds were almost similar.

Chapter III: Development of High Capacity Adsorbents for NO_x Removal

NO_x referred in this study consists of both nitric oxide (NO) and nitrogen dioxide (NO_2). Relative proportions of NO and NO_2 in NO_x change spatially in an urban atmosphere depending on the ozone (O_3) concentration and the intensity of solar radiation [11]. This is because there exists a set of reactions taking place in the atmosphere involving both NO and NO_2 as well as ozone and solar UV radiations. These set of reactions [46] are shown below

$$NO + O_3 \rightarrow NO_2 + O_2 \qquad \text{(Eq. III.1)}$$

$$NO + HO_2 \rightarrow NO_2 + OH \qquad \text{(Eq. III.2)}$$

$$NO + RO_2 \rightarrow NO_2 + RO \qquad \text{(Eq. III.3)}$$

$$NO_2 + h\nu \rightarrow NO + O. \qquad \text{(Eq. III.4)}$$

As per above set of reactions when NO is emitted to the atmosphere, it is oxidized to NO_2 by O_3 and peroxy radicals (HO_2, RO_2). Simultaneously, NO_2 is photodissociated to NO by solar UV radiation. NO_2/NO_x ratio in air generally varies from 0.35 to 0.65 in an urban atmosphere [11].

NO and NO_2 have been reported to be equally harmful for the performance of PEMFC [7] because the same concentration of NO or NO_2 in the cathode air was reported to cause almost similar percentage drop in the performance of PEM fuel cell. Hence, it is necessary to remove both these contaminants from cathode air.

III.1 Adsorbents for Removal of NO_2

III.1.1 Experimental section

III.1.1.1 Preparation of the adsorbents

As KOH/Al_2O_3 and $MnO_x(SO_4$ route)$/Al_2O_3$ showed the two highest breakthrough capacities for SO_2 removal; these sorbents were tested for NO_2 removal. The idea behind testing these two sorbents for NO_2 adsorption was to find out if only one adsorbent with high adsorption capacity for both SO_2 and NO_2 removal can be used. In addition to above two sorbents, activated Carbon derived from coconut shell (PICA) was also tested for NO_2 removal as activated carbon has been reported to have the high adsorption capacity for NO_2 at room temperature [47-51]. Formation of both oxygen and nitrogen surface complexes was observed on the surface of activated carbon after NO_2 adsorption [48-50]. Additionally, KOH was impregnated on this activated carbon (10 wt%) using incipient wetness method and the sample was dried in convection oven at 110^0C for 7 hours. This adsorbent was prepared to find out if activated carbon after such impregnation shows any improvement in the adsorption capacity for NO_2 as compared to bare activated carbon. Commercial Campure 6XL (6 wt% $KMnO_4/Al_2O_3$) sorbent was also tested for comparison purposes. Particle size of all the adsorbents tested was 180-250 µm.

III.1.1.2 Experimental setup

Same experimental setup that was used to carry out the SO_2 adsorption tests (figure II.1) was also used to perform the NO_2 breakthrough studies on selected sorbents. One more mass flow controller (Aalborg GFC-17) was used to measure and control the flow rate of NO_2 for the experiments that involved mixture of two gases (SO_2 + NO_2) in the challenge gas. Concentration of NO_2 in challenge gas was kept at 20 ppm and face velocity of 70 cm/s was used. All the sorbents were tested for NO_2 adsorption at room temperature and at 50% RH.

III.1.2 Results and Discussion

III.1.2.1 Comparison of NO_2 breakthrough capacity of adsorbents

Breakthrough curves of all the above-mentioned sorbents for NO_2 removal are shown in figure III.1 along with the operating conditions used.

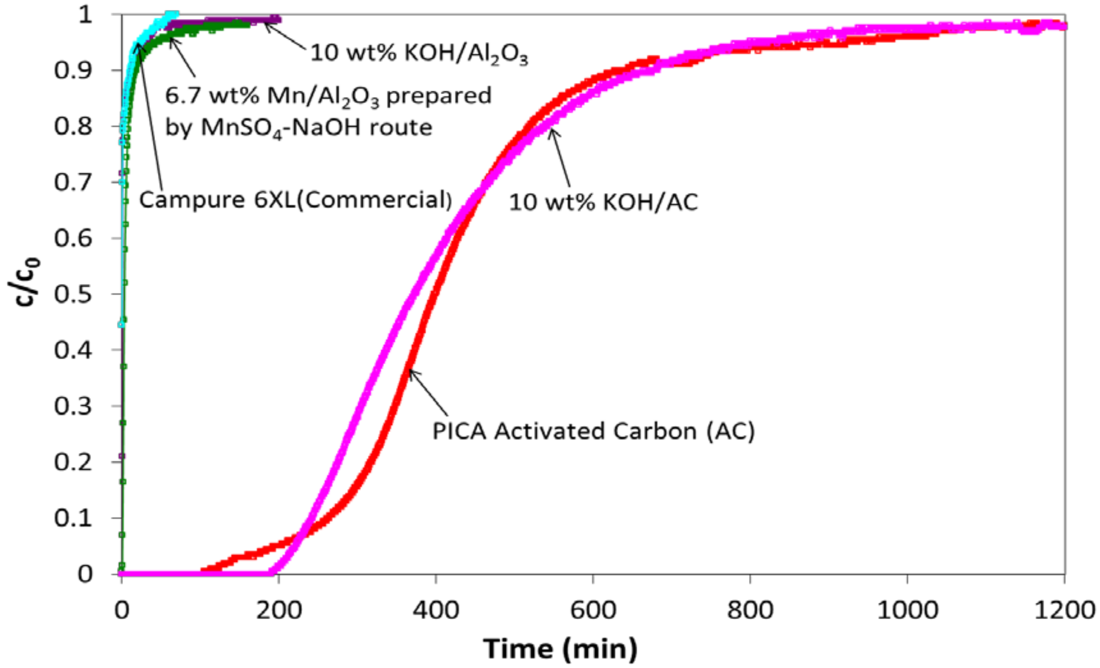

Column ID = 5/8″; W = 0.5g; V = 70 cm/s; C_{inlet} = 20 ppm NO_2; D_p = 180-250µm; RH = 50%; T = 25°C

Figure III.1: NO_2 breakthrough curves for γ-Al_2O_3 and PICA activated carbon supported sorbents

As can be seen from figure III.1, all Al_2O_3 based sorbents (KOH/Al_2O_3, MnOx(SO_4 route)/Al_2O_3 and commercial $KMnO_4/Al_2O_3$) showed immediate breakthrough of NO_2 and thus negligible breakthrough capacity for NO_2 removal. All these sorbents showed very little saturation capacity also. Since KOH/Al_2O_3 showed very little adsorption capacity for NO_2, it was concluded that KOH did not react with NO_2 at room temperature as it did in the case of SO_2 adsorption. Lee et al. [52] reported that NO_2 saturation capacity of KOH/Al_2O_3 prepared by incipient wetness impregnation method was 1.1 mol of NO_2/mol of KOH at temperature of 200°C and inlet NO_2 concentration of 500 ppm. Thus it was concluded that reaction between KOH and NO_2 is not feasible at room temperature and a high temperature of close to 200°C is required to overcome the activation energy barrier for this reaction.

PICA activated carbon based sorbents showed the significant breakthrough and saturation capacity for NO_2 removal. Breakthrough capacity of KOH/AC was found to be higher than that of bare activated carbon. However, saturation capacity of bare activated carbon was still higher as compared to KOH/AC. It has been reported in the literature that the surface of activated carbon itself is highly active for the chemisorption of NO_2 [48-51]. So, it was deduced that the impregnation of KOH on activated carbon actually blocked some of these active sites present on the surface of activated carbon and this resulted in decreased saturation capacity of KOH/AC sorbent for NO_2 removal. Adsorption capacities of all the sorbents tested for NO_2 removal are shown in table III.1.

Table III.1: Adsorption capacities of the sorbents tested for NO_2 removal

Sorbent	**Breakthrough Capacity at c/c_0=0.02 (mg of NO_2/cc)**	**Saturation Capacity (mg of NO_2/cc)**
PICA Activated Carbon	42.6	131.5
10 wt% KOH/AC	65.1	118.6
10 wt% KOH/Al_2O_3	0	1.4
MnO_x/Al_2O_3 Prepared by $MnSO_4$ route (6.7 wt% Mn)	0.2	3.8
Campure 6XL (6 wt% $KMnO_4/Al_2O_3$)	0	1.8

Based on the NO_2 saturation capacities of tested sorbents above, bare activated carbon (PICA AC) was selected as the NO_2 removal sorbent for cathode air filter application.

III.1.2.2 Generation of NO during removal of NO_2

Generation of considerable amount of NO was observed during the adsorption of NO_2 on activated carbon. This simultaneous generation of NO with NO_2 adsorption is shown in figure III.2.

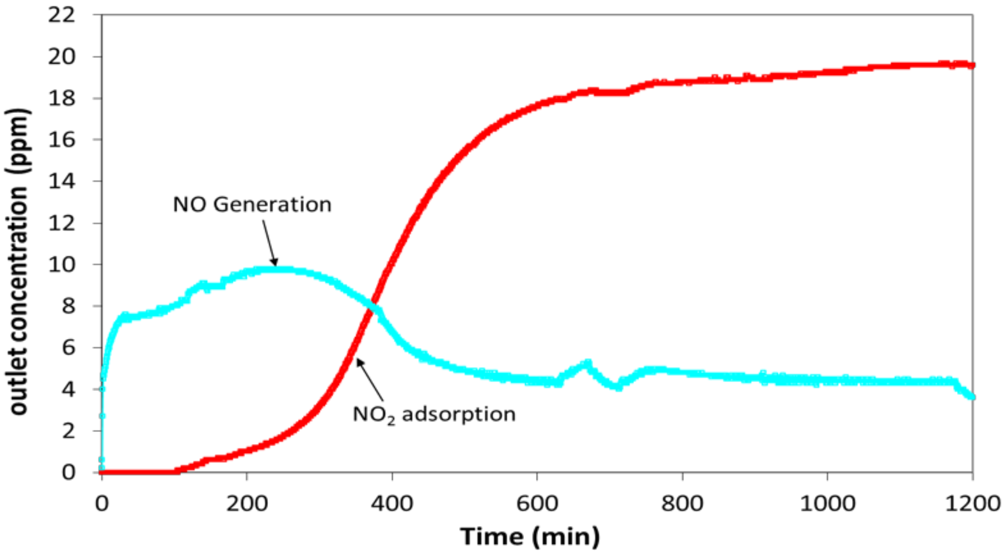

Column ID = 5/8″; W = 0.5g; V = 70 cm/s; C_{inlet} = 20 ppm NO_2; D_p = 180-250µm; RH = 50%; T = 25°C

Figure III.2: NO_2 breakthrough curve for PICA activated carbon along with the simultaneous NO generation curve

As can be seen from figure III.2, NO in very significant concentration was coming out of the bed even before the breakthrough of NO_2. Curve of outlet concentration of NO generated with respect to time goes through maxima. This formation of NO by reduction of NO_2 on the carbon surface during the adsorption of NO_2 at room temperature has also been reported in several previous studies [48-51]. This reduction of NO_2 also leads to the oxidation of carbon surface. It was also observed that the higher the saturation capacity of sorbent for NO_2 removal, more was the amount of NO generated.

As mentioned earlier, concentrations of both NO and NO_2 in the outlet stream were measured by plug-in electrochemical sensors installed in the multigas detector MultiRAE plus. Every such electrochemical sensor has some cross-sensitivity for the other gaseous species present in the sampling stream, where the sensor responds to the other gases that are not filtered out and that can react on the electrode [53]. Thus, if the gas stream being sampled by an electrochemical sensor contains another gas apart from the target gas being detected then it becomes very important to know the potential cross-sensitivity of electrochemical sensor due to presence of another gas. Cross-sensitivities of both NO and NO_2 sensors have been mentioned in the operating manual of MultiRAE Plus gas detector and these have been reproduced here table III.2 [53].

Table III.2: Cross-sensitivity of electrochemical sensors used in MultiRAE Plus gas detector

Sensor	Cross-sensitivity, %	
	Challenge gas: NO	Challenge gas: NO_2
NO	100	30
NO_2	0	100

As can be seen from table III.2, NO_2 sensor is not sensitive to NO but NO sensor has almost 30% cross-sensitivity for NO_2. In other words, NO_2 concentration measured by corresponding sensor is not affected if NO is also present in the gas stream. However, NO concentration measured by NO sensor would be affected to a certain degree if NO_2 is present in the same gas stream and concentration of NO displayed by using NO sensor in such case will be always higher (by ~ 30%) than the actual concentration of NO. To find out the details of cross-sensitivity of NO sensor for NO_2, NO sensor was exposed to air with varying concentrations of NO_2 (and without any NO gas present in those streams) for one hour. After one hour NO sensor showed steady value of NO concentration in each case due to its cross-sensitivity for NO_2. Plot of different NO_2 concentrations to which NO sensor was exposed versus steady values of NO concentrations detected by NO sensor is shown in figure III.3. In the same plot, a third order polynomial fit to actual curve with $R^2 = 0.9317$ is also shown. This third order polynomial equation was used to find out the cross-sensitivity values of NO sensor for different NO_2 concentrations. For each point on the NO generation curve in figure III.2, corresponding cross-sensitivity of NO sensor was then subtracted from the measured outlet concentration of NO to get the actual concentration of NO at the outlet.

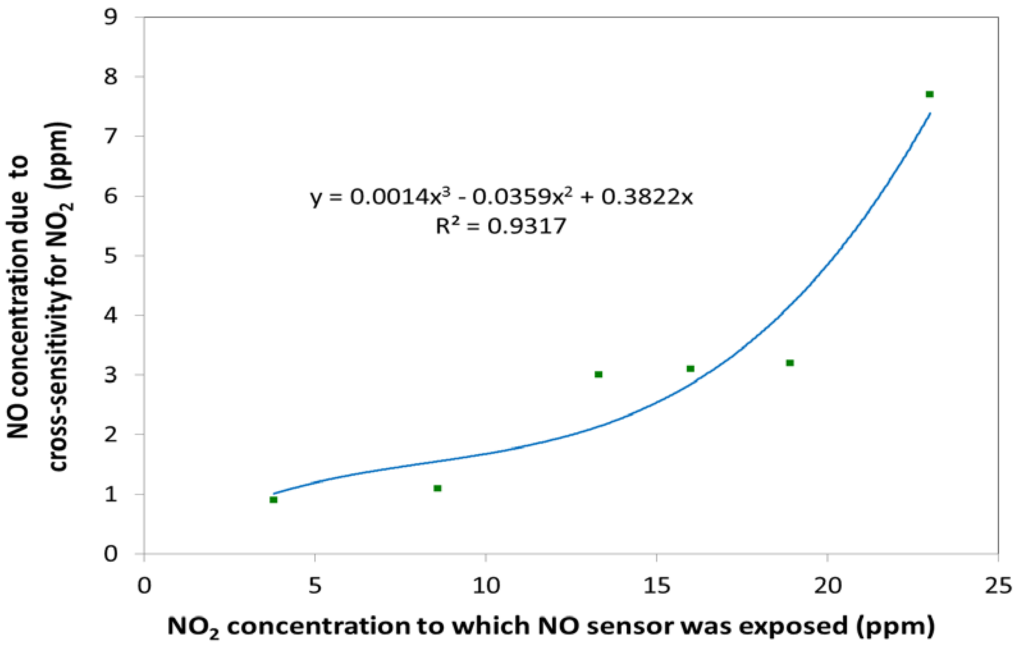

Figure III.3: Cross-sensitivity of NO sensor when exposed to different concentrations of NO_2 in the challenge gas

Figure III.4 shows the breakthrough curve for NO_2 adsorption on activated carbon along with two values of the outlet NO concentration; one is the concentration measured by NO sensor and the other one is the actual concentration of NO corrected for the cross-sensitivity of NO sensor.

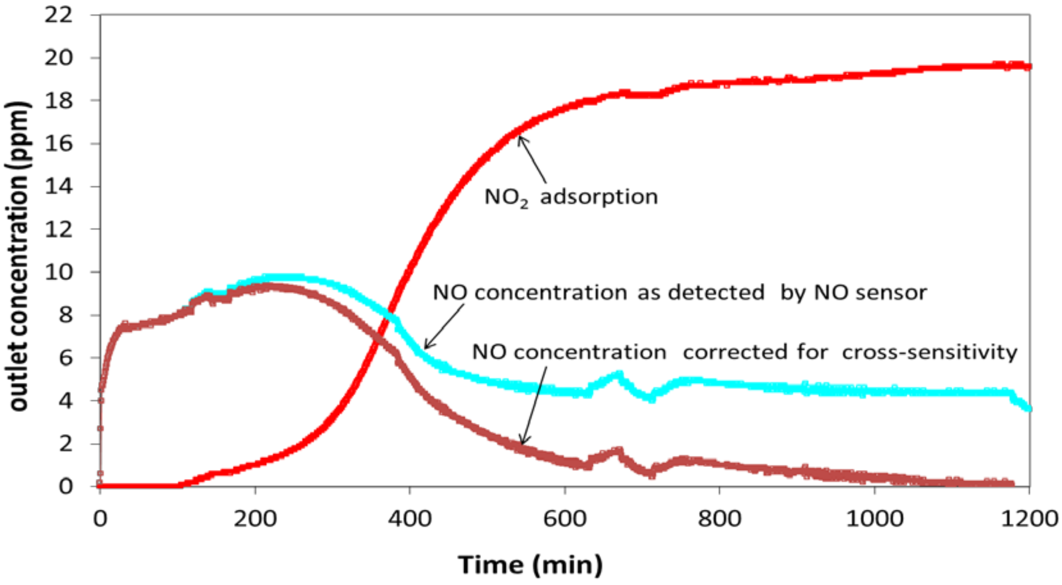

Column ID = 5/8″; W = 0.5g; V = 70 cm/s; C_{inlet} = 20 ppm NO_2; D_p = 180-250µm; RH = 50%; T = 25°C

Figure III.4: NO_2 breakthrough curve for PICA activated carbon along with the simultaneous NO generation curve corrected for cross-sensitivity of NO sensor

From figure III.4, it can be seen that the cross-sensitivity corrected actual concentration of NO in the outlet went to zero when NO_2 breakthrough curve reached the saturation point. So, it was concluded that no nitric oxide (NO) was coming out of the bed once the activated carbon was saturated by NO_2 adsorption and thus the nitrogen balance at the saturation point for NO_2 ($c/c_0 = 1$) was closed. This conclusion clearly shows the importance of correcting the outlet NO concentration values for the cross-sensitivity of NO sensor.

Two Different reaction mechanisms have been proposed in the literature [48, 50] to explain the generation of NO by reduction of NO_2 on carbon during the adsorption of NO_2. These two mechanisms are shown below

1. $4NO_2 + 2C^* \rightarrow 2NO_{gas} + (2NO\text{-}O_2)_{ads} + 2C(O)$ (Eq. III.5)

Zhang et al. [48] proposed the above reaction for NO_2 reduction on the carbon in the early stage of NO_2 adsorption. In this reaction, 50% of consumed NO_2 is released as NO gas (NO_{gas}) and the other 50% gets adsorbed as NO on the carbon surface ($(2NO\text{-}O_2)_{ads}$). The oxygen produced will either oxidize the carbon surface to form surface oxygen containing groups (C(O)) or it will be retained as molecular O_2 coadsorbed with NO on the carbon surface. Thus, carbon acts in part as a reducing agent during the adsorption of NO_2.

2. $-C^* + NO_2 \rightarrow -C(NO_2)$ (Eq. III.6)

$-C(NO_2) \rightarrow -C(O) + NO$ (Eq. III.7)

$-C(O) + NO_2 \rightarrow -C(ONO_2)$ (Eq. III.8)

Jeguirim et al. [50] postulated the above sequence of reactions for the formation of oxygen complexes during NO_2 adsorption on the carbon. According to this mechanism, equation III.6 is the first step of nitrogen complexes formation. However, due to rapid formation of NO, the $-C(NO_2)$ complex is most likely unstable and it rapidly decomposes according to equation III.7. This decomposition generates NO that appears in the outlet of the carbon bed. A significant fraction of the -C(O) surface complexes formed react further with NO_2 to form $-C(ONO_2)$ surface complexes.

Results for NO_2 adsorption on activated carbon suggest that the sorbent for efficient removal of NO must be found in order to protect the PEM fuel cell from NO which is coming in not only from cathode air but which also is generated during NO_2 adsorption on activated carbon.

III.2 Adsorbents for Removal of NO

III.2.1 Literature review

Since one of the major sources of nitrogen oxides (NO_x) emissions in the atmosphere are the stationary sources such as thermoelectric power plant and incinerator, large number of studies published in the literature on NO removal have focused their attention on the removal of NO released mainly from such stationary sources. Selective catalysts reduction (SCR) of nitric oxide (NO) has been generally recognized as the most effective and widely commercialized technology for the removal of NO emitted from the stationary sources. In order to convert NO in the flue gas to N_2, reducing agents such as NH_3, CO, H_2 and a variety of hydrocarbons such as methane, propylene etc. have been employed [54]. Although a number of reducing agents can be used in SCR of NO, ammonia is the most commonly used and the resultant process is called as SCR-NH_3 [55]. After intensive research on the development of SCR-NH_3 catalysts, vanadia supported on titania (V_2O_5/TiO_2) has been found to be the most effective and widely used commercial SCR catalyst due to its high activity and durability to sulfur compounds [54]. However, the disadvantage of this particular catalyst is that it exhibits the high conversion only in the high temperature range of 573-673 K. Consequently stack gas reheating is unavoidable for use of this SCR catalyst in retrofit applications. Hence, there has been a great interest in the development of SCR catalysts that are active at low temperatures (<473 K). Kijlstra et al. [56] reported that alumina supported manganese oxides are very active for this SCR reaction over the lower temperature range of 383-573 K. However, in the same study it was also observed that these low temperature SCR catalysts were strongly deactivated by small concentrations of SO_2 in the flue gas stream. It is also to be noted that the SCR process is applicable for NO removal only for very high concentrations of NO which are found in the flue gas (~ 500 ppm) and not for the low concentration of NO that is found in ambient air. Thus, it can be concluded from the above discussion that removal of NO by SCR process is not a feasible option in case of cathode air filter application, because SCR requires a much higher operating temperature (>383 K at least) and cathode air from which NO to be removed is always present at ambient temperature. Hence, some alternate route to effectively remove NO present in lower concentrations at room temperature must be found for cathode air filter applications.

One such effective alternative that has been described in the literature to remove NO at room temperature is the oxidation of NO to NO_2. Both activated carbon fibers (ACFs) and granular activated carbon (GAC) were reported to have good catalytic activity (~ 80% conversion of NO to NO_2 at steady state) for NO oxidation to NO_2 in dry air and at low temperatures (25-30^{o}C) [57-59]. Guo et al. [57] postulated that the apparent reaction rate of NO oxidation is the first order with respect to NO concentration and the 0.25th order with respect to the oxygen concentration. However oxidation of NO to NO_2 was reported to decrease significantly (conversion < 5%) with the increase in relative humidity (particularly for RH > 40%) and the decrease in NO concentration (particularly NO concentration below 100 ppm) [57, 58]. As the relative humidity of cathode air can often be higher than 40% in many operating environments of PEMFC and the concentration of NO in air is usually well below few ppm; activated carbon is expected to show very little activity for the oxidation of NO to NO_2.

Potassium permanganate ($KMnO_4$) is known to be a strong oxidizing agent and most of the applications involving $KMnO_4$ make use of its strong oxidizing ability. Oxidation of NO to NO_2 in gas phase using $KMnO_4$ has been rarely reported in the known literature. This may be because of low reactivity of NO. However few studies have been published on the oxidation of NO in the liquid phase as soon as it is absorbed into the aqueous solution containing $KMnO_4$. Uchida et al. [60] reported that when NO is absorbed into neutral solution containing $KMnO_4$ as an oxidizer, the possible reaction in the liquid phase is

$$NO + KMnO_4 \rightarrow KNO_3 + MnO_2 \qquad \text{(Eq. III.9)}$$

In this case, NO is oxidized into NO_3^- and $KMnO_4$ is reduced to MnO_2. In the same study, it was observed that the absorption reaction of NO with $KMnO_4$ taking place in an aqueous solution of mixture of $KMnO_4$ and NaOH is first order with respect to NO concentration in the gas phase as well as first order with respect to $KMnO_4$ concentration in liquid phase.

From the above discussion, it was decided to test $KMnO_4/Al_2O_3$ in addition to activated carbon for the oxidation of NO to NO_2.

III.2.2 Experimental section

III.2.2.1 Preparation of the adsorbents

As described in the previous section, both activated carbon and $KMnO_4$ are known to be active for NO oxidation to different extents depending on the operating conditions. Hence, coconut shell based activated carbon and $KMnO_4/Al_2O_3$ were tested for NO oxidation at room temperature. $KMnO_4/Al_2O_3$ was prepared by impregnating γ-Al_2O_3 with $KMnO_4$ using incipient wetness method and the sample was dried in convection oven at 110°C for 7 hours. $KMnO_4$ loading in this sorbent was 4 wt%. Additionally as MnO_x(SO_4 route)/Al_2O_3 with 6.7 wt% Mn was the sorbent selected for SO_2 removal, it was also tested for NO removal to see if a single adsorbent can be used to remove both NO and SO_2 simultaneously. Particle size of all the tested adsorbents was 180-250 µm.

III.2.2.2 Experimental setup

Same experimental setup that was used to carry out the SO_2 adsorption tests (figure II.1) was also used to perform NO oxidation studies on the selected sorbents. MultiRAE Plus gas detector was used to detect the concentrations of both NO and NO_2 simultaneously. Concentration detection range for NO_2 sensor is 0-20 ppm and that for NO sensor is 0-250 ppm. Concentration of NO in challenge gas was kept at 20 ppm and face velocity of 70 cm/s was used. All the sorbents were tested for NO oxidation at room temperature and 50% RH. As described earlier in the section on the adsorbents for NO_2 removal, outlet concentrations of NO shown on all the plots for NO oxidation were corrected for cross-sensitivity of NO sensor for NO_2.

III.2.3 Results and Discussion

III.2.3.1 Performance of selected adsorbents for NO oxidation

Breakthrough curves for NO removal on the selected sorbents are shown in figure III.5.

Nitric Oxide removal by oxidation

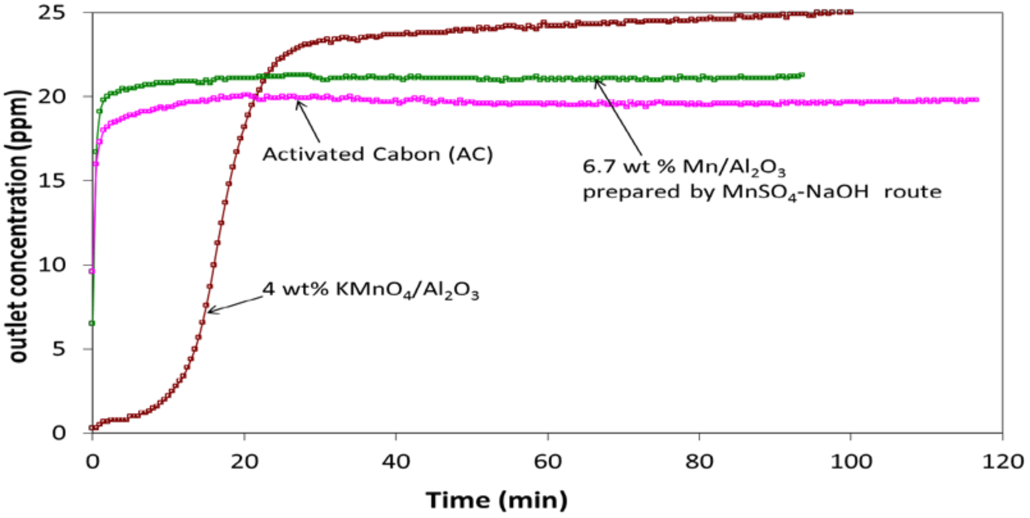

Nitrogen dioxide generation

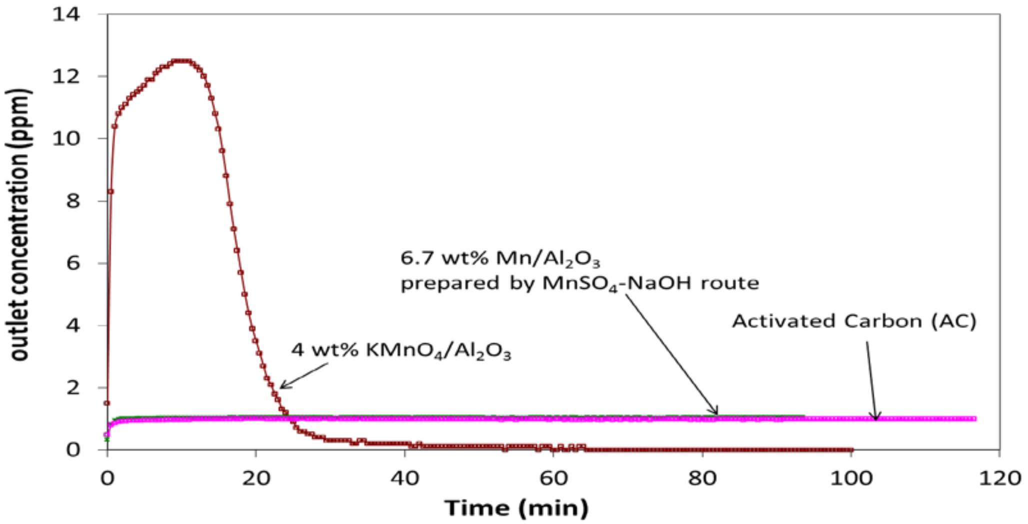

Column ID = 5/8″; W = 0.5g; V = 70 cm/s; C_{inlet} = 20-25 ppm NO; D_p = 180-250µm; RH = 50%; T = 25^{o}C

Figure III.5: NO breakthrough curves for γ-Al_2O_3 and PICA activated carbon supported sorbents along with the outlet concentration curves of NO_2 generated by NO oxidation

As can be seen from figure III.5, only 4 wt% $KMnO_4/Al_2O_3$ showed the reasonable breakthrough capacity for NO removal (1.2 mg of NO/cc at $c/c_0 = 0.02$) by oxidizing it to NO_2. Both the activated carbon and MnO_x(SO_4 route)/Al_2O_3 showed very quick breakthrough of NO with almost no capacity for NO removal. Saturation capacity of 4 wt% $KMnO_4/Al_2O_3$ was calculated to be 6.6 mg of NO/cc. It was also observed that the outlet concentration of NO_2 went through maxima with respect to time and its maximum value (12.5 ppm) observed was almost half of the inlet concentration of NO.

It would be preferable to develop only one sorbent that can remove both NO and NO_2 efficiently rather than to use a mixture of two different sorbents. Activated carbon was the selected adsorbent for NO_2 removal and strong oxidizer $KMnO_4$ was found to remove NO effectively by its oxidation to NO_2. So it was decided to impregnate PICA activated carbon with $KMnO_4$ to find out if along with NO_2, such sorbent can remove NO also and thus delay the appearance of NO in the exit gas stream. PICA activated carbon was impregnated with $KMnO_4$ by using incipient wetness method and the loading of $KMnO_4$ was 4 wt%. NO_2 breakthrough curves for both activated carbon and 4 wt% $KMnO_4$/AC are shown in III.6 along with the NO generation curves. NO_2 saturation capacity of 4% $KMnO_4$/AC (105.2 mg of NO_2/cc) was found to be less than that of bare activated carbon (131.5 mg of NO_2/cc). More importantly, 4% $KMnO_4$/AC did not show any breakthrough capacity for NO since NO appeared immediately in the exit gas steam during NO_2 adsorption on $KMnO_4$/AC, which was also observed in the case of bare activated carbon. So it was concluded that the loading of $KMnO_4$ on activated carbon do not help in delaying the appearance of NO in the exit gas stream and the physical mixture of PICA AC and $KMnO_4/Al_2O_3$ is required to remove NO_x (both NO and NO_2) completely from the cathode air stream.

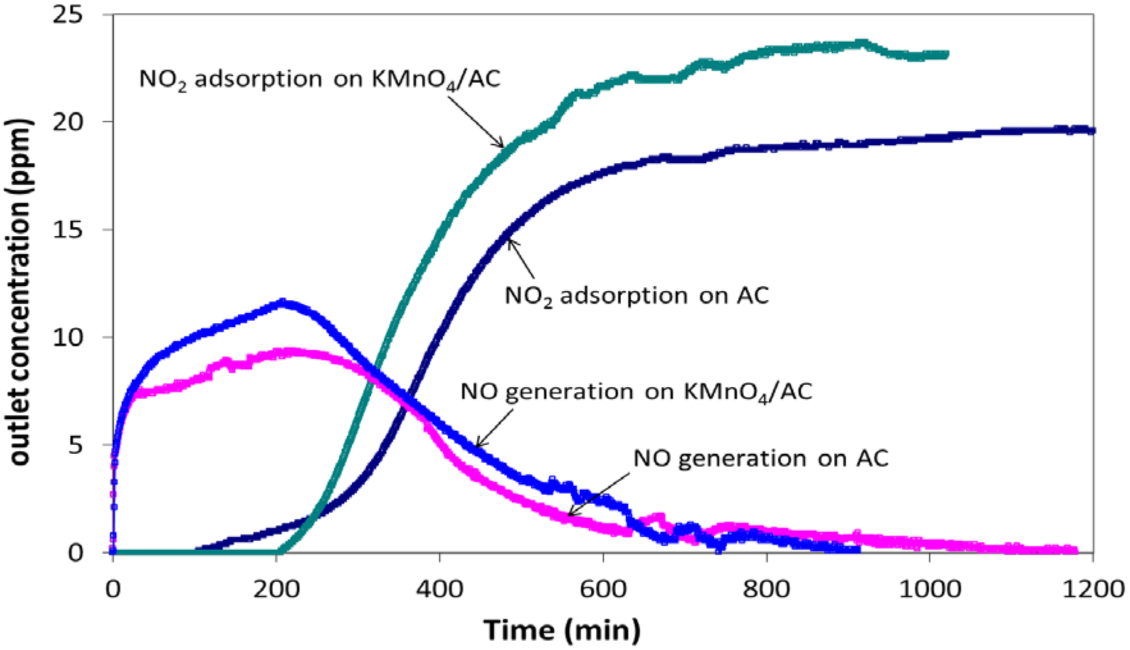

Column ID = 5/8″; W = 0.5g; V = 70 cm/s; C_{inlet} = 20 ppm NO_2; D_p = 180-250µm; RH = 50%; T = 25°C

Figure III.6: NO_2 breakthrough curves for PICA activated carbon and 4 wt% $KMnO_4$/AC along with the simultaneous NO generation curves

III.3 Mixture of the Selected Sorbents for Complete Removal of NO_x

Breakthrough test with NO_2 in the challenge gas was carried out on 50/50 wt% blend of PICA AC and 4 wt% $KMnO_4/Al_2O_3$ (0.5g of AC + 0.5g of $KMnO_4/Al_2O_3$) in order to find out the efficiency of such sorbent mixture to remove both NO (generated from NO_2 adsorption on activated carbon) and NO_2 (from the challenge gas). As shown in figure III.7, 50/50 wt% blend of these sorbents increased the NO_2 breakthrough time by almost 110% (t_b = 280 min at c/c_0 = 0.02) as compared to that of activated carbon alone (t_b = 131.5 min at c/c_0 = 0.02). More importantly, blend of the sorbents delayed the appearance of NO in exit gas stream by 25 minutes. When defined as mg of NO_2/g of sorbent, NO_2 saturation capacity of the blend of two sorbents was found to be 373.9 mg of NO_2/g whereas NO_2 saturation capacity of activated carbon alone was 305.8 mg of NO_2/g. NO_2 saturation capacity of the blend of sorbents was thus 22% higher than that of only activated carbon. Here it was assumed that only activated carbon in the blend was responsible for NO_2 adsorption and hence, weight of only activated carbon in the blend was used in calculating the NO_2 saturation capacity of the blend of sorbents. However, volume of the bed of blend of sorbents was higher than the volume of activated carbon bed. Hence when defined as mg of NO_2/cc , NO_2 saturation capacity of the blend of sorbents (93.7 mg of NO_2/cc) was found to be lower than that of activated carbon alone (131.5 mg of NO_2/cc).

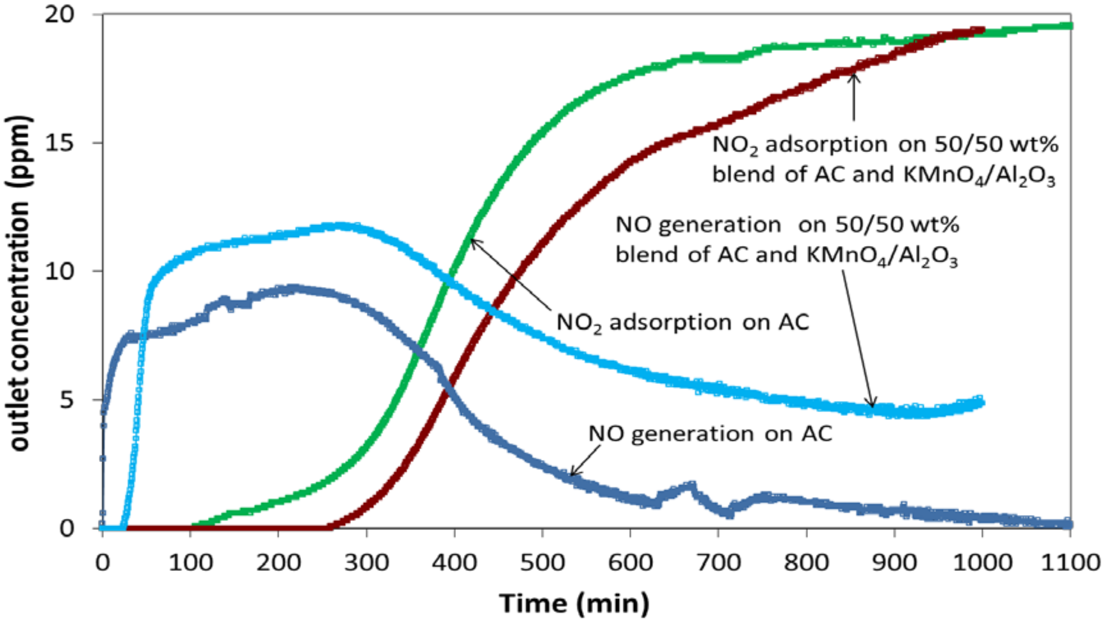

Column ID = 5/8″; V = 70 cm/s; C_0 = 20 ppm NO_2; D_p = 180-250µm; RH = 50%; T = 25°C; W = 0.5g for AC and 1g for blend (0.5g AC+ 0.5g $KMnO_4/Al_2O_3$)

Figure III.7: NO_2 breakthrough curves for PICA activated carbon and 50/50 wt% blend of sorbents (PICA activated carbon+$KMnO_4/Al_2O_3$) along with the simultaneous NO generation curves

In case of the blend of the sorbents, following processes were assumed to take place simultaneously.

1. NO is generated by NO_2 adsorption on activated carbon.

2. This generated NO gets immediately oxidized to NO_2 on the neighboring particles of $KMnO_4/Al_2O_3$ present in the blend.
3. This NO_2 formed as a result of NO oxidation again gets adsorbed on the adjacent activated carbon particles.

Thus it can be seen that in the case of blend of sorbents, there exists a dynamic relationship between NO_2 adsorption and NO generation. Because of superior breakthrough performance of the blend of sorbents for removal of NO as well as NO_2, it was decided to use this blend of activated carbon and $KMnO_4/Al_2O_3$ for effective removal of NO_x from the cathode air.

When expressed in vol%, 50/50 wt% blend of PICA AC and 4 wt% $KMnO_4/Al_2O_3$ corresponds to 58 vol% loading of activated carbon and 42 vol% loading of 4 wt% $KMnO_4/Al_2O_3$. Both NO and NO_2 breakthrough times of such blend of sorbents depend on the vol% loading of each sorbent in that blend. Higher the vol% loading of $KMnO_4/Al_2O_3$, higher is the breakthrough time for NO and similarly, higher the vol% loading of activated carbon, higher is the breakthrough time for NO_2. Thus it was important to understand the effect of vol% composition of this blend on its breakthrough performance for NO and NO_2. For this purpose, in addition to above-mentioned 58:42 vol% blend of activated carbon and 4 wt% $KMnO_4/Al_2O_3$, 30:70 vol% blend of the same sorbents (30 vol% activated carbon and 70 vol% $KMnO_4$/Al2O3) was tested for NO and NO_2 removal. NO_2 breakthrough curves and NO generation curves for both the compositions of the blend are shown in figure III.8. As expected, NO_2 breakthrough time of 58:42 vol% blend (t_b = 280 min at $c/c_0 = 0.02$) was found to be almost three times higher than that of 30:70 vol% blend (t_b = 100 min at $c/c_0 = 0.02$). However, NO breakthrough time of 30:70 vol% blend was found to be almost the same as that of 58:42 vol% blend (t_b = 26 min for

c_{NO} = 0.4 ppm). Increasing the loading of 4 wt% $KMnO_4/Al_2O_3$ in the blend from 42 vol% to 70 vol% did not improve the NO breakthrough performance of the blend but instead it caused the significant drop in the NO_2 breakthrough performance. Thus it was concluded that the overall breakthrough performance of 58:42 vol% blend was superior to that of 30:70 vol% blend for complete removal of NO_x and hence this superior vol% composition of the blend should be used in the cathode air filter to remove NO_x from cathode air.

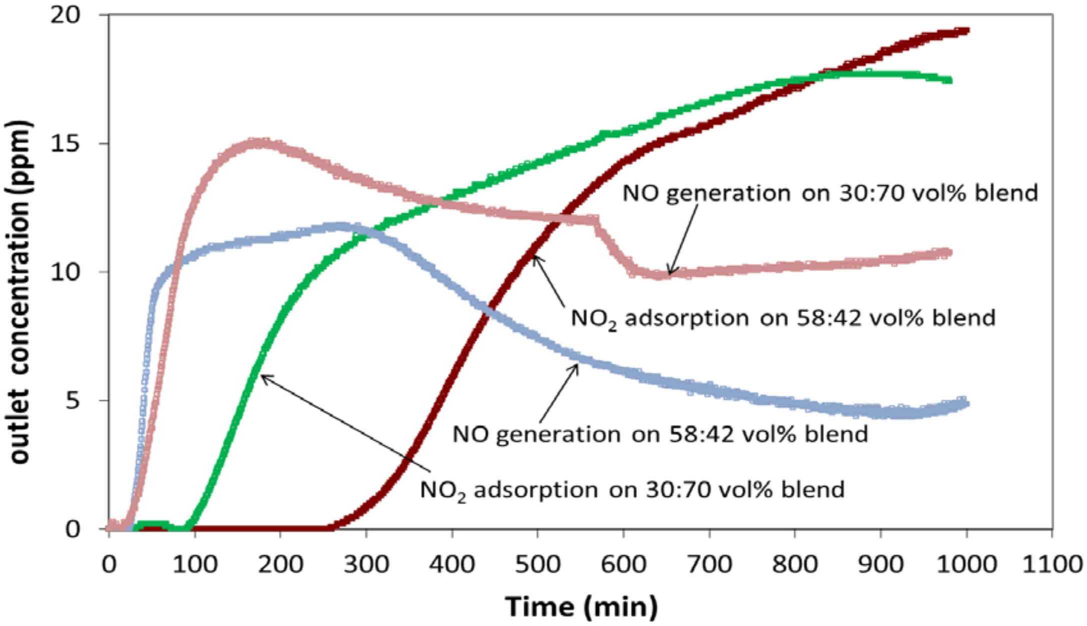

Column ID = 5/8″; V = 70 cm/s; C_0 = 20 ppm NO_2; D_p = 180-250µm; RH = 50%; T = 25°C;
W = 0.5g of Activated Carbon + 0.5g of 4%$KMnO_4/Al_2O_3$ for 58:42 vol% blend and
0.27g of Activated Carbon + 0.82g of 4%$KMnO_4/Al_2O_3$ for 30:70 vol% blend

Figure III.8: NO_2 breakthrough curves for 58:42 vol% blend and 30:70 vol% blend of PICA activated carbon and 4 wt% $KMnO_4/Al_2O_3$ along with the simultaneous NO generation curves

III.4 Adsorption Performance of Individual Sorbents when Exposed to Mixture of Gases (SO_2 + NO_2)

From the adsorption tests carried out on the different sorbents so far to effectively remove major contaminants in cathode air, following sorbents were finally selected for the removal of SO_2 and NO_x.

- $MnO_x(SO_4$ route$)/Al_2O_3$ for SO_2 removal by adsorption
- PICA activated carbon for NO_2 removal by adsorption
- $KMnO_4/Al_2O_3$ for NO removal by oxidation

However, each of the above-mentioned sorbents was tested for its adsorption performance with only one relevant contaminant present in the challenge gas. In practical applications of PEMFC, cathode air will most likely contain the mixture of contaminants rather than any single contaminant alone. Therefore it becomes important to make sure that the adsorption capacity of each of the selected sorbents for their respective contaminant remains largely unaffected when any one of these sorbents is exposed to mixture of contaminants. Two sets of experiments were carried out to confirm this performance requirement for each of the selected sorbents. In first set of experiments, $MnO_x(SO_4$ route$)/Al_2O_3$ sorbent was exposed to SO_2 as well as mixture of SO_2 and NO_2. Similarly in the second set of experiments, activated carbon was exposed to NO_2 as well as mixture of SO_2 and NO_2. Results of both sets of experiments are shown in figure III.9 and figure III.10.

SO_2 adsorption on $MnO_x(SO_4$ route$)/Al_2O_3$

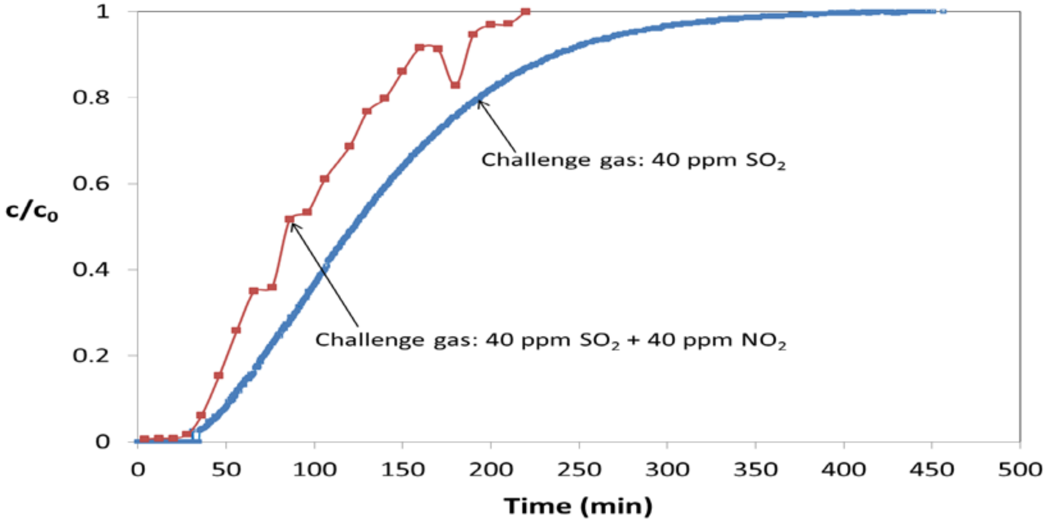

Column ID = 5/8″; W = 0.5g; V = 70 cm/s; Dp = 180-250µm; RH = 50%; T = 25°C

Figure III.9: SO_2 breakthrough curves for MnO_x(SO_4 route)/Al_2O_3 with and without NO_2 present in the challenge gas

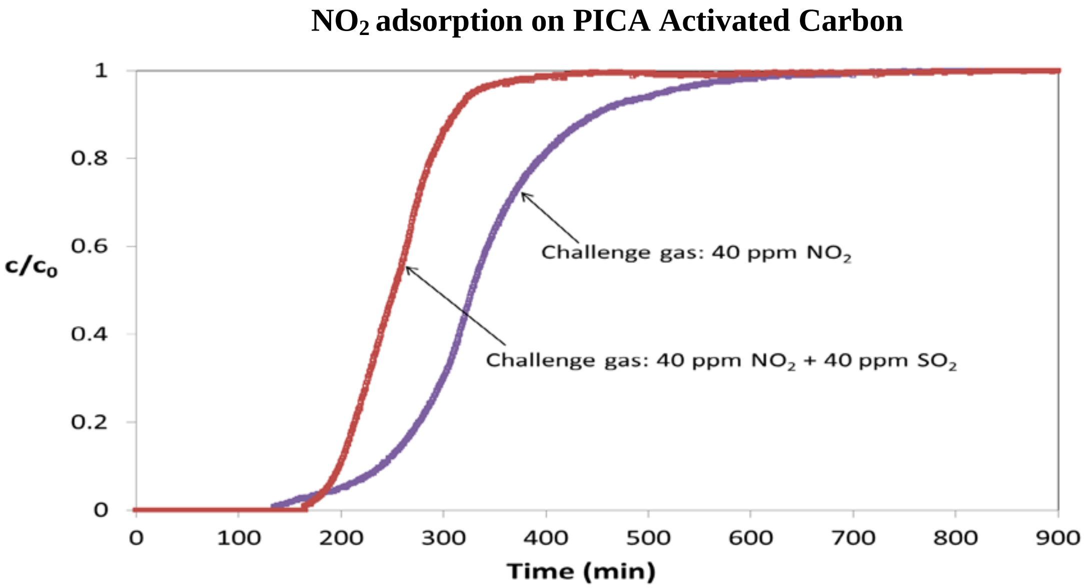

Column ID = 5/8″; W = 0.5g; V = 70 cm/s; Dp = 180-250µm; RH = 50%; T = 25°C

Figure III.10: NO_2 breakthrough curves for PICA activated carbon with and without SO_2 present in the challenge gas

GasAlertMicro 5 gas detector was used to measure the concentration of both NO_2 and SO_2 in the above sets of experiments. SO_2 sensor used in this detector has a very high cross-sensitivity (-100%) for NO_2. However, NO_2 sensor used in this gas detector does not have any cross-sensitivity for SO_2. For this reason, when MnO_x(SO_4 route)/Al_2O_3 was exposed to mixture of SO_2 and NO_2; outlet concentration of SO_2 was measured by using PFPD detector on GC (Varian). Microliter syringe was used to take the sample from outlet stream and then this sample was injected in the corresponding port of PFPD on GC. SO_2 breakthrough curve obtained in this way was not as smooth as the one obtained from SO_2 measurements by gas detector. It is because in the case of PFPD each sampling cycle lasts for 6 minutes. On the other hand, data logging interval in GasAlertMicro 5 gas detector can be set anywhere between 10 seconds to 120 seconds.

As observed from figures III.9 and III.10, when both MnO_x(SO_4 route)/Al_2O_3 and activated carbon were exposed to the mixture of SO_2 and NO_2; breakthrough time of each of this sorbent for its corresponding contaminant did not change significantly. However, a small drop in the saturation capacities of both the sorbents was observed after the exposure to gas mixture. These results are summarized in table III.3.

Table III.3: Adsorption capacities of selected sorbents after exposure to mixture of gases (SO_2 + NO_2)

Adsorbent	Gas for which adsorption capacities are calculated	Breakthrough capacity for different challenge gases ($c/c_0 = 0.02$) (mg of gas/cc)			Saturation capacity for different challenge gases (mg of gas/cc)		
		40 ppm SO_2	40 ppm NO_2	40 ppm SO_2 + 40 ppm NO_2	40 ppm SO_2	40 ppm NO_2	40 ppm SO_2 + 40 ppm NO_2
MnO_x(SO_4 route)/Al_2O_3	SO_2	40.7	-	37.2	158.9	-	116.1
Activated carbon	NO_2	-	58.2	66.8	-	203.9	154.9

From the table III.3, it can be seen that the saturation capacity of each sorbent for the removal of corresponding contaminant (SO_2 capacity of MnO_x(SO_4 route)/Al_2O_3 and NO_2 capacity of activated carbon) decreased by approximately 25% when that sorbent was exposed to mixture of SO_2 and NO_2. However change in the breakthrough capacity of each sorbent after its exposure to gas mixture was less than 10%. Thus, it can be concluded that the adsorption capacities of individual sorbents did not change drastically when the sorbents were exposed to mixture of SO_2 and NO_2.

In conclusion, it was decided to use the mixture of three different sorbents in cathode air filter to remove SO_2, NO and NO_2 from cathode air. This mixture consists of MnO_x(SO_4 route)/Al_2O_3 to remove SO_2, PICA AC to remove NO_2 and $KMnO_4/Al_2O_3$ to remove NO.

Chapter IV: Construction and Testing of Different Configurations of Cathode Air Filter

IV.1 Background

Once the high capacity adsorbents were selected to remove each of the three major contaminants (SO_2 and NO_x) from cathode air, the next important step is to package these sorbents into different configurations of cathode air filter to find out the optimal configuration with lower pressure drop and the highest adsorption capacity and removal efficiency. Two different layers of filtration media are required to remove particulate as well as gaseous impurities from air. They are

1. Particulate filtration media

Commercial HEPA (High Efficiency Particulate Arrestance) filter media can be used for the removal of particulates from air. HEPA filters have MERV rating of 17-20. The Minimum Efficiency Reporting Value, also known simply as MERV, measures the performance of air purifiers in terms of particulate removal efficiency. Higher number of MERV rating translates into more effective air filtration. By definition, MERV 17 should remove at least 99.97% of airborne particles of diameter 0.3 μm or less. This HEPA filter media is composed of fibers made from fiberglass with diameters between 0.5 and 2.0 micron. As a result of use of such small diameter fibers, HEPA filter media usually has a significant pressure drop across it. Hence, particulate filter media with bit lower particle removal efficiency (MERV 13-14) but that is still effective enough to protect PEMFC should be tested for its use in cathode air filter.

2. Gas removal (adsorptive) filtration media

As have been mentioned earlier in section I.6, two basic types of bed design options available to remove gaseous impurities from cathode air are packed bed and microfibrous media (MFM). Benefits and limitations of both these beds have been mentioned in the same section. Beneficial features of both these beds can be synergistically combined in the form of composite bed, which has been discussed earlier. Additionally, microfibrous media can be pleated to construct a pleated air filter configuration to remove gaseous impurities. A pleated filter uses a highly folded media to increase the available filtration area and to extend the filter's useful life. The extra media area also confers the additional advantage of reducing the pressure drop across the filter and the resultant energy consumption. One such pleated filter structure is shown in figure IV.1 below.

Figure IV.1: Schematic of a typical pleated air filter

Thus two separate layers of filter media to remove particulate and gaseous contaminants can be incorporated into different design combinations for the cathode air filter. They are

1. Particulate filter (for particulate filtration) + packed bed (for gaseous filtration) (PF+PB)
2. Particulate filter + pleated MFM filter (for gaseous filtration) (PF+MFM)
3. Particulate filter + composite bed (for gaseous filtration) (PF+CB)

Design space and footprint for cathode air filter

From the practical applications point of view, it was decided to construct the different configurations of cathode air filter mimicking the dimensions of particulate air filter that is installed on one of the existing PEMFC system. This will give better insight into volume constraints that will be placed on the cathode air filter to retrofit it into existing filter slot of PEMFC system. Thus it will give a more realistic basis to compare the pressure drop and contaminant removal performance of different configurations of cathode air filter in a fixed volume.

Particulate air filter installed in the Ballard's NEXA^{TM} power module as shown in figure IV.2 was taken as the design prototype to construct different configurations of cathode air filter. Any new design of cathode air filter must retrofit in existing filter slot of PEMFC. NEXA power module, produced by Ballard Power Systems is the world's first volume produced PEMFC module. This module is intended to be used in the applications such as back-up power generators and stationary power supply systems. This module provides 1200 W of DC power output at a nominal output voltage of 26 V. This module has 43 cells in its stack. The dimensions of the existing particulate air filter installed in this module are also shown in figure IV.2. Air flow rate required to operate this module at full load was calculated to be 100 SLPM (standard liters per min).

Design Space for cathode air filter

Footprint:	4.25″ x 3″ x 5/8″
Power:	1200 W
Flow Rate:	100 SLPM

Figure IV.2: Particulate air filter installed in Ballard's NEXA^{TM} PEM fuel cell stack

IV.2 Theoretical Explanation for the Advantages of Composite Bed over Packed Bed

As described earlier, it is postulated that for a fixed volume of the filter the composite bed design will give much higher log removal efficiency for the contaminants than the packed bed with a little increase in pressure drop. This expected significant increase in the breakthrough times of composite bed as compared to packed bed for contaminant removal can be explained by proposing an equal area theory. According to this theory, when polisher layer alone is exposed to the inlet concentration of challenge gas; amount of this gas adsorbed on the polisher till the breakthrough point will be same as the quantity of gas adsorbed on this polisher layer when it is added downstream of the packed bed. However in the latter case, polisher will now be exposed to the lower concentrations of challenge gas that is coming out of the packed bed. Hence, as this polisher layer will see decreased concentrations of the challenge gas at its inlet and the cumulative amount of the gas adsorbed on it before breakthrough will still be the same as in the case of polisher alone, addition of this polisher layer at the end of packed bed is expected to increase the breakthrough time of the resultant composite bed significantly.

This equal area theory is demonstrated in figure IV.3 by using typical breakthrough curves found for the polisher layer, packed bed and composite bed. Referring to figure IV.3, area of the region highlighted with green color shows the quantity of challenge gas adsorbed on the polisher till the breakthrough point when this polisher alone is exposed to inlet concentration of challenge gas. When this polisher layer is added downstream of a packed bed, concentration of challenge gas seen by this polisher at its inlet now is decreased to the concentration of challenge gas at the exit of packed bed. This polisher in the composite bed configuration will still adsorb similar quantity of contaminant before the breakthrough point as it does when it alone is exposed to the inlet concentration of challenge gas. In other words, area of the region highlighted with green color is equal to area of the region highlighted with blue color and both these areas correspond to the amount of contaminant adsorbed on the polisher before breakthrough.

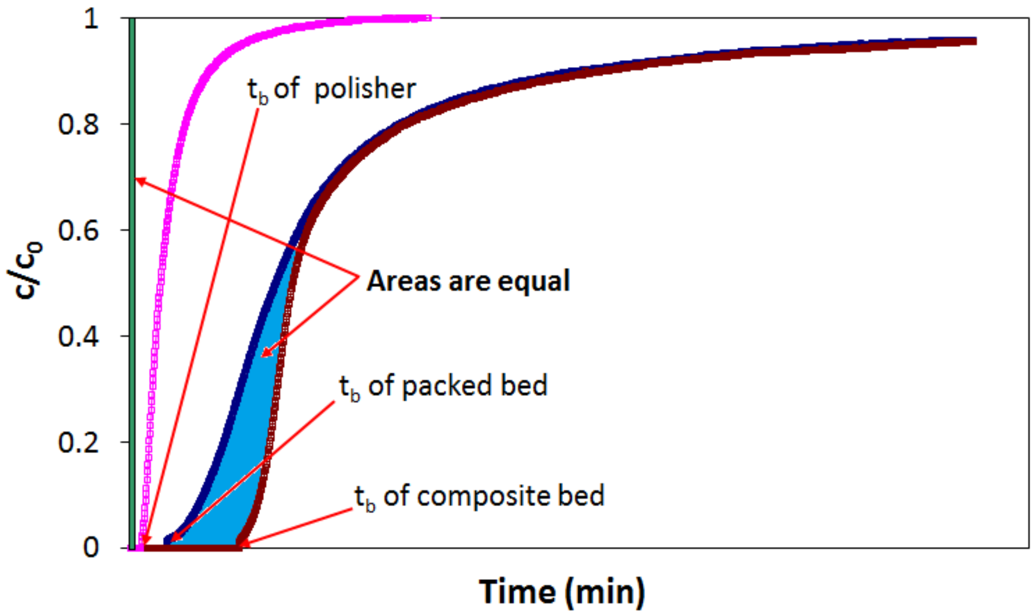

Figure IV.3: Increase in the breakthrough time of composite bed by addition of polisher layer explained with the equal area theory

IV.3 Experimental

A preliminary experiment was carried in a tubular adsorption column to compare breakthrough performance of packed bed and composite bed for SO_2 removal over MnO_x(SO_4 route)/Al_2O_3 (with 6.7 wt% Mn). This was done to find out the extent of improvement in the breakthrough performance of the composite bed. Here, packed bed was consisting of 0.85-1.4 mm size particles of MnO_x(SO_4 route)/Al_2O_3 with the bed depth of 1.5 cm. Composite bed consisted of above-mentioned packed bed and additional polisher layer of MFM downstream of this packed bed. This polishing layer was prepared by entrapping 150-180 μm Al_2O_3 particles in the matrix of 13 μm polymer fibers. Polymer fibers used here were sheath-core type bicomponent fibers. Sheath-core bicomponent fibers are those fibers where one of the components (core, made of PET in this case) is fully surrounded by the second component (sheath, made of LLDPE in this case). The detailed procedure to make this MFM is described below.

A blender was filled with 1 liter of water and 4 ml of dispersant (Cruwik SYN) was added to it at low speed of stirring. This dispersing agent was required to make the hydrophobic surface of polymer fibers hydrophilic and to help them disperse in the water. 3g of polymer fibers was added in blender to make the aqueous slurry. This slurry was then transferred to a head box already filled with water. 6g of Al_2O_3 particles were added to the head box and were mixed with the slurry using hand dasher. Water was then drain quickly to get a preform. This preform was then sintered in convection oven at 170^oC for 15 minutes. MFM prepared by this way was then impregnated with $MnSO_4$ and NaOH in successive steps by soaking the sheet in the solutions of respective chemicals. The method of impregnating the Al_2O_3 particles entrapped in this MFM with MnO_x by using $MnSO_4$ as a precursor was exactly the same as the method of preparation of powder sample of the same sorbent.

SO_2 breakthrough curves for both the packed bed and composite bed are shown in figure IV.4 and their respective breakthrough times are listed in table IV.1. Face velocity for this set of experiments was set at 50 cm/s and inlet concentration of SO_2 in the challenge gas was kept 70 ppm. Thus the operating conditions used for this set of experiments were similar to those used for the screening of adsorbents to find a high capacity sorbent for SO_2 removal.

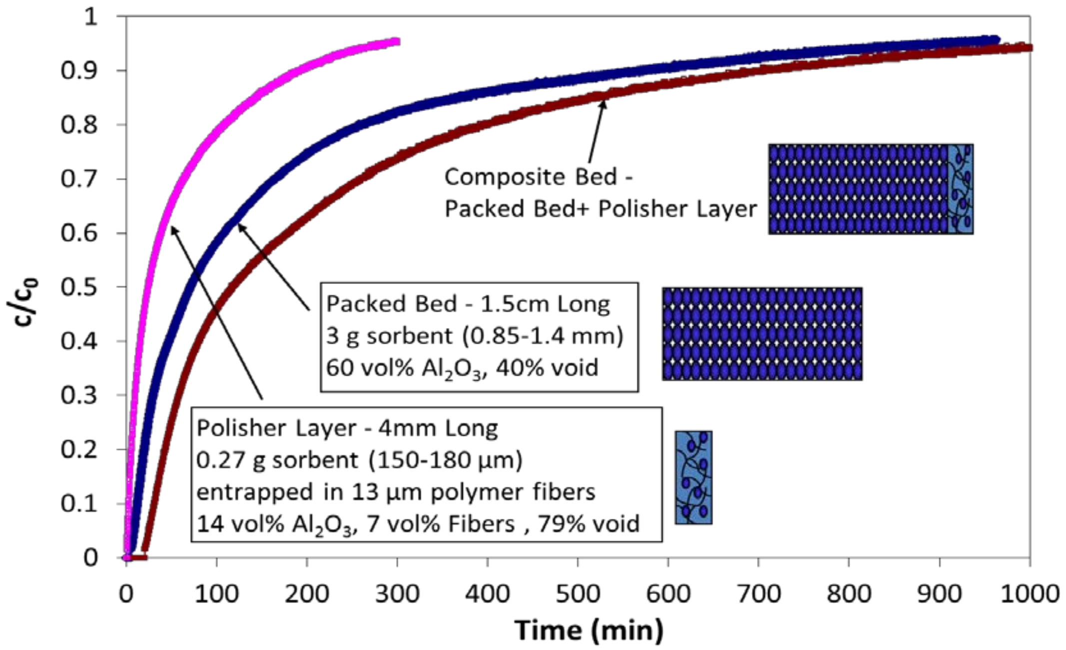

Column ID = ¾″; V = 50 cm/s; C_{inlet} = 70 ppm SO_2; RH = 50%; T = 25°C

Figure IV.4: Comparison of SO_2 breakthrough performance of $MnO_x(SO_4$ route)/Al_2O_3 in packed bed configuration and composite bed configuration for $c_0 = 70$ ppm

The composite bed showed 3.4 times higher breakthrough time than the packed bed in this case. Thus it was confirmed that the addition of thin polisher layer downstream of packed bed leads to significant increase in the breakthrough performance along with little increase in the total volume of the bed. Increase in the pressure drop across composite bed due to additional polisher layer was not significant because of the relatively smaller thickness of the polisher layer.

Table IV.1: SO_2 breakthrough times of $MnO_x(SO_4$ route)/Al_2O_3 in the packed bed and composite bed configuration for $c_0 = 70$ ppm and V = 50 cm/s

Bed Configuration	**Breakthrough Time (min) for $c/c_0 = 0.02$**
Packed Bed	6.5
Composite Bed	22

Second set of breakthrough experiments were carried out to compare the breakthrough performance of packed bed and composite bed under the operating conditions that are close to those found in the real-life applications of cathode air filter. Face velocity was set at 20 cm/s which is same as the face velocity of air passing through the prototype design of cathode air filter that is installed on Ballard's NEXA^{TM} PEMFC stack. Also, lower inlet concentration of 20 ppm was used for SO_2 in the challenge gas since concentrations of the contaminants found in the actual operating environments of PEMFC are typically few ppms. SO_2 breakthrough curves for both the packed bed and the composite bed under these operating conditions are shown in figure IV.5 and their respective breakthrough times are listed in table IV.2.

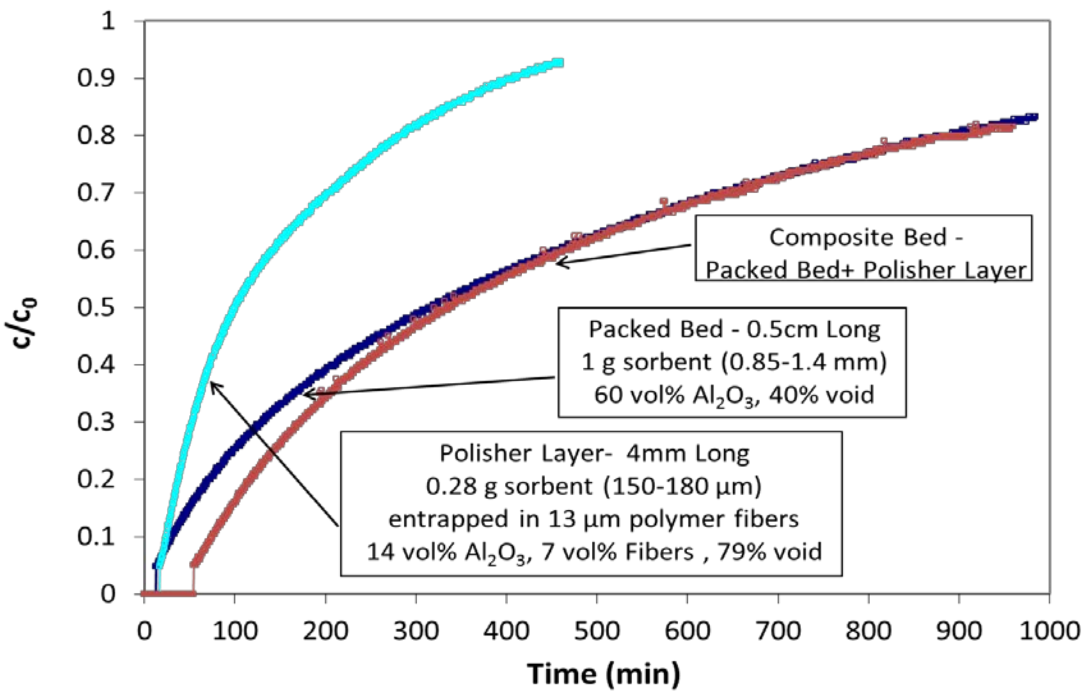

Column ID =¾″; V = 20 cm/s; C_{inlet} = 20 ppm SO_2; RH = 50%; T = 25°C

Figure IV.5: Comparison of SO_2 breakthrough performance of $MnO_x(SO_4$ route$)/Al_2O_3$ in packed bed configuration and composite bed configuration for $c_0 = 20$ ppm

Referring to figure IV.5, the composite bed showed almost 3.6 times higher SO_2 breakthrough time than the packed bed even under the second set of operating consitions.

Table IV.2: SO_2 breakthrough times for MnO_x(SO_4 route)/Al_2O_3 in the packed bed and composite bed configuration for c_0 = 20 ppm and V = 20 cm/s

Bed Configuration	**Breakthrough Time (min) for c/c_0=0.05**
Packed Bed	15
Composite Bed	55

These results indicate that the composite bed configuration always displays considerably higher breakthrough time than the packed bed for a wide range of SO_2 concentrations and face velocities. This significant improvement in the breakthrough performance of composite bed as compared to packed bed occurs with the slight increase in the volume of adsorber system and with little increase in the pressure drop across the adsorbent bed. Comparison of pressure drops across packed bed and composite bed is discussed in the detail in the next chapter.

Chapter V: Pressure Drop across Different Configurations of Cathode Air Filter

Pressure drop is one of the important parameters for selecting the optimal configuration of cathode air filter. It is because pressure drop across the filter increases the power consumed by the compressor of PEM fuel cell in compressing the inlet air to its final pressure. As power supplied to the compressor is part of the electric energy generated by PEM fuel cell itself, this power is considered as the type of parasitic power loss. Thus, pressure drop across filter should not be exceedingly high as it will lead to increased parasitic power loss with reduced efficiency of PEM fuel cell. Importance of the pressure drop while considering the performance expectations from cathode air filter was discussed in detail in section I.5.

V.1 Pressure Drop across Packed Bed

Pressure drop across a porous packed bed is calculated by using the Ergun's equation [12] shown below.

$$\frac{\Delta P}{L} = \frac{u_0}{D_p}\left(\frac{1-\varepsilon}{\varepsilon^3}\right)\left[\frac{150(1-\varepsilon)\mu}{D_p} + 1.75\rho u_0\right] \qquad \text{(Eq.V.1)}$$

where

ΔP = Pressure drop across packed bed

L = Bed depth

u_0 = Fluid superficial velocity

ε = Voidage of the bed

D_p = Particle diameter

μ, ρ = Viscosity and density of the fluid respectively

Substituting the following values for the variables in the Ergun's equation, pressure drop per unit length for packed bed was found.

u_0 = 20.3 cm/s = 40 FPM, which is the face velocity for the cathode air filter installed in Ballard's NEXA PEMFC stack when operated at full load of 1.2 kW,

ε =0.4, which is the typical value of void fraction for packed beds ,

$\rho = 1.2$ kg/m^3 and $\mu = 18.2\times10^{-6}$ kg/m-s for air at 298K

These predicted pressure drops across the packed beds of different particle sizes are shown in table V.1.

Table V.1: Pressure drop per unit length of packed bed predicted by using Ergun's equation

Particle size range (microns)	**Log mean particle size (microns)**	**ΔP/L (″H_2O/cm)**
180-250	213	2.9
350-500	420	0.79
850-1400	1102	0.13

As can been seen from table V.1, ΔP across packed bed increased by almost four times when the particle size was reduced by half; thus giving the dependence of ΔP ~ $\propto \frac{1}{D_P^2}$. So, decrease in the sorbent particle size leads to increased single pass removal efficiency and higher breakthrough time but this improvement in the breakthrough performance comes at the expense of increased pressure drop. Such overly high ΔP for packed beds of smaller size particles (~ 200 μm) are not acceptable for cathode air filter application and hence other configurations of cathode air filter need to be tested in order to find out the filter design which will give high contacting efficiency at an acceptable pressure drop.

V.2 Pressure Drop across Polisher Layer of Microfibrous Media

The detailed procedure to prepare a polisher layer of microfibrous media using bicomponent polymer fibers is mentioned earlier in the section IV.3. Voidage in the microfibrous media (MFM) is usually higher (typically >70 %) than the typical voidage in a packed bed (~40%). This voidage in MFM can go as high as 98% depending on the fiber and particle loading in it. It has been reported that the experimental data for pressure drop deviate sharply from the values predicted by Ergun's equation for void volumes greater than 80% because the Ergun's equation does not account for form drag [61]. So the Ergun's equation is applicable only to beds with voidages 50% or less because it does not include the form drag losses, which are small in packing materials of low porosity. Cahela et al. [61] have developed a model equation known as porous media permeability (PMP) equation to predict the pressure drop over the entire range of possible bed voidages. PMP equation can also predict the pressure drop for the structures consisting of mixture of fibers and particles of any shape such as MFM. Although pressure drop across MFM can be predicted using PMP equation, it was decided to measure the pressure drop across a layer of MFM experimentally for different values of face velocity.

V.2.1 Experimental

A sheet of microfibrous media was prepared by entrapping 180-250 μm γ-Al_2O_3 particles in the matrix of 13 μm polymer fibers as per the procedure mentioned in section IV.3. Thickness of this sheet was found out to be 2 mm by using vernier caliper. 2″ disc was cut out from this sheet and house air was passed through it at different flow rates. Pressure drop across this sample was measured at increasing values of face velocity. The experimental set up constructed and used by Karwa et al. [62] from the same lab was used to obtain the pressure drop data in the present study. Details of this experimental setup are mentioned below.

The setup used the compressed house air for testing. House air was dehumidified using silica gel desiccators and then, HEPA filtered to remove any background aerosol contaminants. The air flow was controlled by mass flow controller (MFC). The sample holder was made from stainless steel 1″ (ID) pipes and flanges. A 2″ diameter sample was used to provide a seal around the edges of the 1″ diameter area. The sample was held between the two flanges with closed-cell foam gaskets to form an air-tight seal. The pressure drop across the filter media was measured at different face velocities using an Omega (Product # PX154-010DI) pressure transducer. Schematic of this experimental setup is shown in figure V.1.

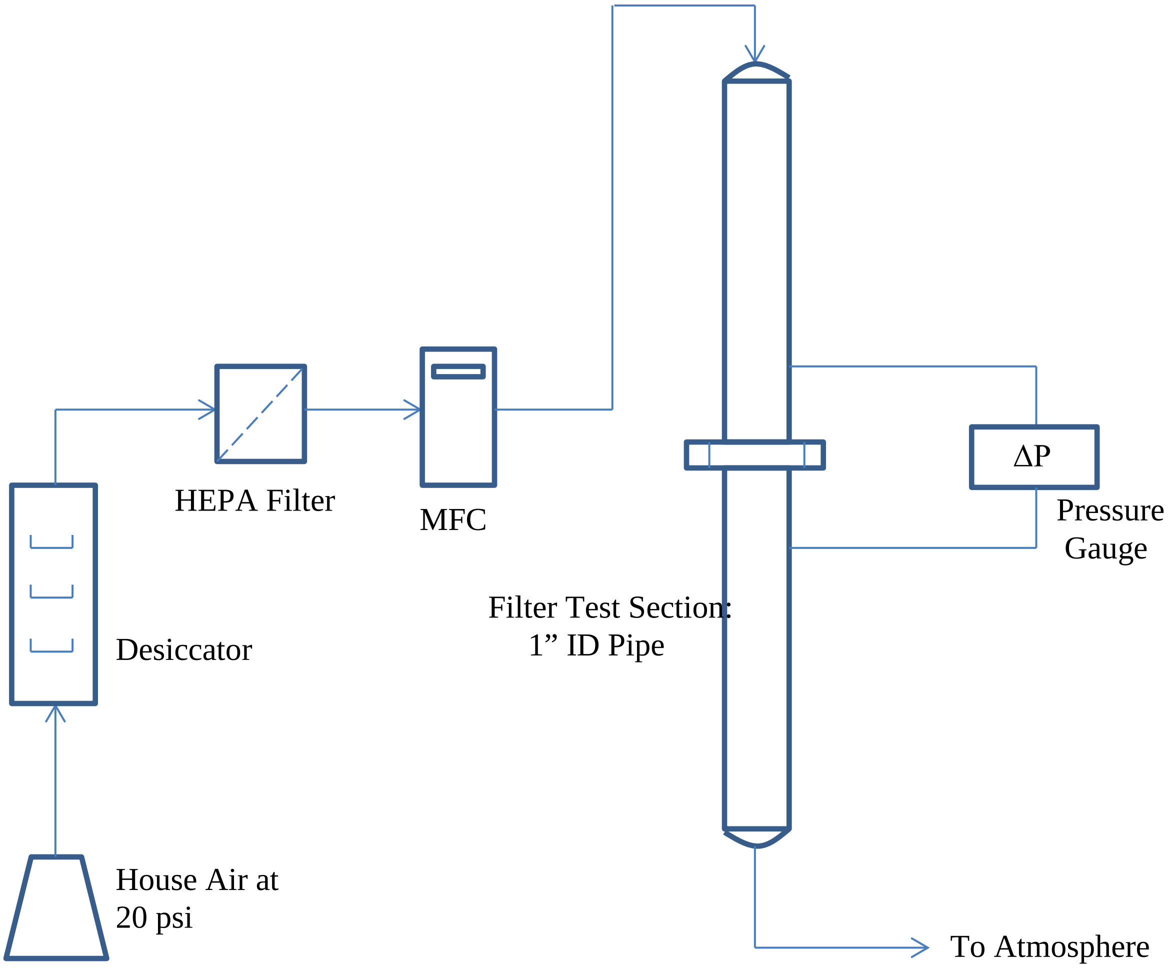

Figure V.1: Experimental setup for pressure drop testing

V.2.2 Results and Discussion

Pressure drop performance of a clean filter is called the “initial” performance of the filter. The performance of filter at the end of its service life is called “final” performance of the filter. The study performed in the present work focuses only on the initial performance of the filter. The typical acceptable initial pressure drop for HEPA filters is around 1″ of H_2O and for ULPA it is around 1.1″ of H_2O at 500 FPM. Pressure drop measured across 2″ sample of polymer microfibrous media at increasing air flow rates is shown in figure V.2. Face velocity was expressed in FPM (Feet Per Minute) and corresponding pressure drop was measured in ″ of H_2O.

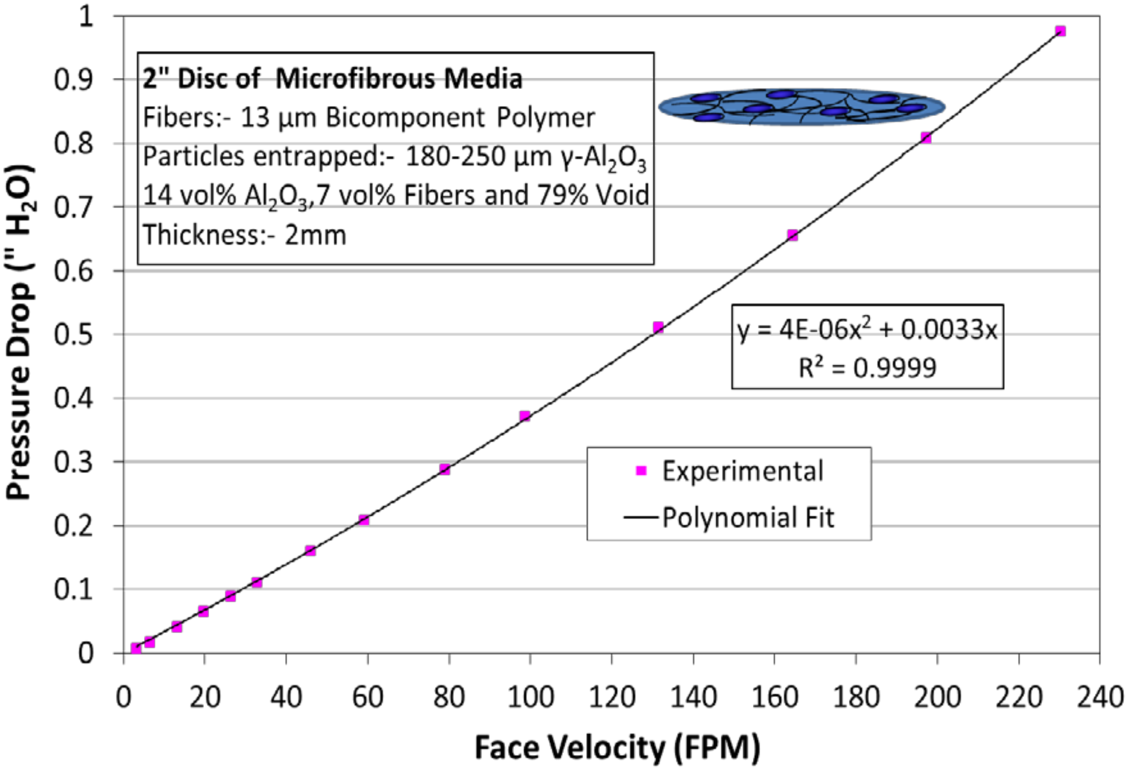

Figure V.2: Pressure drop across 2″ disc of polymer microfibrous media with respect to face velocity

As can be seen from figure V.2, pressure drop across polymer MFM increases linearly with face velocity of air for lower face velocities. At higher face velocities, pressure drop dependence of face velocity is seen to become quadratic. This is because at lower face velocities, the pressure drop across filter typically varies linearly with face velocity of air as per Darcy's law [63] as shown in equation V.2.

$$\Delta P = \frac{\mu L}{k} V_m \qquad \text{(Eq.V.2)}$$

Where,

ΔP = Pressure drop across media

μ = Viscosity of air

L = Thickness of media

k = Permeability of media

V_m = Face Velocity

However, higher face velocities result in nonlinear deviations from Darcy's law for flow through the media. Rivers et al. [64] concluded that these deviations in filtration media were the product of fiber compression due to air's inertial force compressing the media's fibers together at higher face velocities. This compression changes the internal void volume and tortuosity of the media which leads to higher superficial velocities, decreased permeability and a nonlinear increase in resistance. One way to account for nonlinear deviations from Darcy's law is the addition of a second-order term to Darcy's law [65] as shown in equation V.3.

$$\Delta P = AV_m + BV_m^2 \qquad \text{(Eq.V.3)}$$

Equation V.3 is known as Forchheimer- extended Darcy's law. The A is equivalent to Darcy's law constant ($\mu L/k$). The B accounts for the nonlinear deviations due to inertial effects. Various theoretical equations exist that attempt to relate the physical significance of the media constant B, but they require extensive knowledge of media’s fiber dimensions and packing densities [64]. Therefore for practical purposes, it is preferable to model these media constants using a quick, empirical approach. Thus the curve of pressure drop versus face velocity shown in figure V.2 was fitted to second-order polynomial and the fitted constants and R-squared values are shown in the same plot. These fitted media constants are taken as A and B in the Forchheimer- extended Darcy’s law. In other words, Forchheimer- extended Darcy’s law was applied to the experimental pressure drop versus face velocity data. R-squared value of 0.9999 shows very good fit of second-order polynomial to the experimental data. Thus, here

$A = 0.0033$ ″of H_2O.min/ft and $B = 4\times10^{-6}$ ″of H_2O. min^2/ft^2

Face velocity for the cathode air filter installed in Ballard’s NEXA PEMFC stack is 40 FPM when the stack is operated at full load of 1.2 kW. From the above values of A and B, pressure drop across the same polymer MFM layer was calculated at face velocity of 40 FPM; which came out to be 0.14” H_2O.

V.3 Pressure Drop across Pleated Filter Constructed using Polymer Microfibrous Media

For a pressure drop across a single pleated filter, Sothen et al. [66] have developed a semi-empirical pressure drop model, which can predict pressure drop for a pleated filter with a depth of 3.5″ or less. In developing this model, air flow through a pleated filter was divided into seven regions of varying cross-sectional flow area. These cross-sectional areas correspond to flow of air into and out of grating, into and out of pleat and flow through media. When air flows from one region into the other region, it results in the resistance because of change in the cross-sectional area. The pressure drop across a pleated filter was then calculated as a summation of individual resistances. Semi-empirical pressure drop model reported in that study [66] is shown in its final form below.

$\Delta P_F = 1/2\ \rho\ [(2K_G)V_1^2 + (K_C+K_E+K_P)V_3^2] + AV_4 + BV_4^2$ (Eq.V.4)

Where,

ΔP_F = Pressure drop across a pleated filter

ρ = Density of air at ambient conditions

K_G = Coefficient of friction for flow through a perforated plate, which is calculated as per eq.V.5

$K_G = (1.707-A_{Free}/A_{Total})\ (A_{Free}/A_{Total})^{-2}$ (Eq.V.5)

K_C = Coefficient of friction for sudden contraction, which is calculated as per eq.V.6

$K_C = 0.5 \times (1-A_{Free}/A_{Total})^{0.75}$ (Eq.V.6)

K_E = Coefficient of friction for sudden expansion, which is calculated as per eq.V.7

$K_E = (1-A_{Free}/A_{Total})^2$ (Eq.V.7)

K_P = Coefficient of friction for flow into a pleat of filter, which is calculated as per eq.V.8

$K_P = 0.11\times (P_L/P_O)^{4/3}\ (F_{HD}/F_D)$ (Eq.V.8)

$F_{HD} = (2F_HF_D) / (F_H+F_D)$

F_H, F_W, F_D = Filter height, filter width and filter depth respectively

P_L = Pleat length

P_O = Pleat opening

A, B = Filter media constants calculated by fitting pressure drop across media versus face velocity curve to second-order polynomial

V_1 = Face velocity at the front of the filter

V_3 = Velocity at which air enters and exits each pleat

V_4 = Velocity through filter media

This model needs only few empirical parameters to predict the pressure drop for a pleated filter at given face velocity. These empirical parameters required as inputs for this model are filter media thickness, media permeability constants A and B, dimensions of the pleated filter (width, height and depth of filter) and the dimensions of the air duct in which this filter is installed. Detailed calculations of different cross-sectional areas, corresponding velocities and various pleat parameters are described in the same paper [66].

Particulate air filter installed in the Ballard NEXA^{TM} power module (figure IV.2) was taken as a design prototype in the present study to compare the overall performance of different configurations for cathode air filter. Hence, the dimensions of the filter to be used in the model equation V.4 were $F_H = 3''$, $F_W = 4.25''$, $F_D = 0.625''$. Polymer microfbrous media described in section V.2 was assumed to be the filtration media for the pleated filter under consideration. Therefore values of the media related empirical parameters to be used in the model were: media thickness = 2 mm, A = 0.0033 ″of H_2O.min/ft and $B = 4 \times 10^{-6}$ ″of H_2O. min^2/ft^2.

Substituting values of all the above parameters in the model equation V.4, pressure drop across the pleated filter was predicted with respect to face velocity and the resulting plot is shown in figure V.3. There are five different pressure drop curves in figure V.3 which correspond to five different pleat counts of the pleated filter (from 5 pleats to 25 pleats).

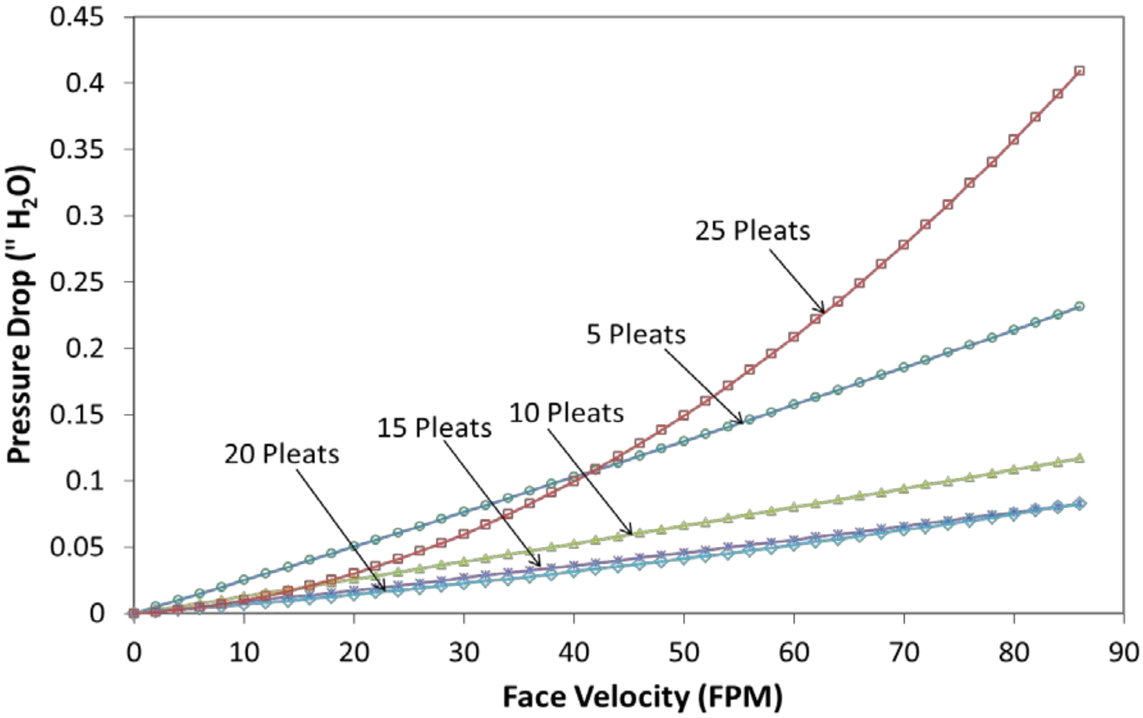

Figure V.3: Pressure drop across the pleated filters predicted by semi-empirical model [66] with respect to face velocity

At a constant face velocity, as the pleat count of a filter is increased, media-induced pressure loss starts decreasing and at the same time, viscous-induced pressure losses (mainly pleat loss) start increasing. Due to this trade-off between media losses and viscous-induced pleat losses, a pleated filter will experience a minimum pressure drop corresponding to an optimal pleat count. Thus, plot of pressure drop versus pleat count for a constant face velocity results in “U” shaped curve as shown in figure V.4. Similar type of “U” shaped pleating curves have been reported in the previous studies related to modeling of pressure drop in a pleated filter [67, 68]. In figure V.4, total resistance versus pleat count graph clearly indicates the lowest value of pressure drop at the optimal pleat count of 20. Lower pleat count region to the left of this optimal number can be considered as the media-dominated regime and the region to the right of optimal pleat count with the higher pleat count can be considered as viscosity-dominated regime.

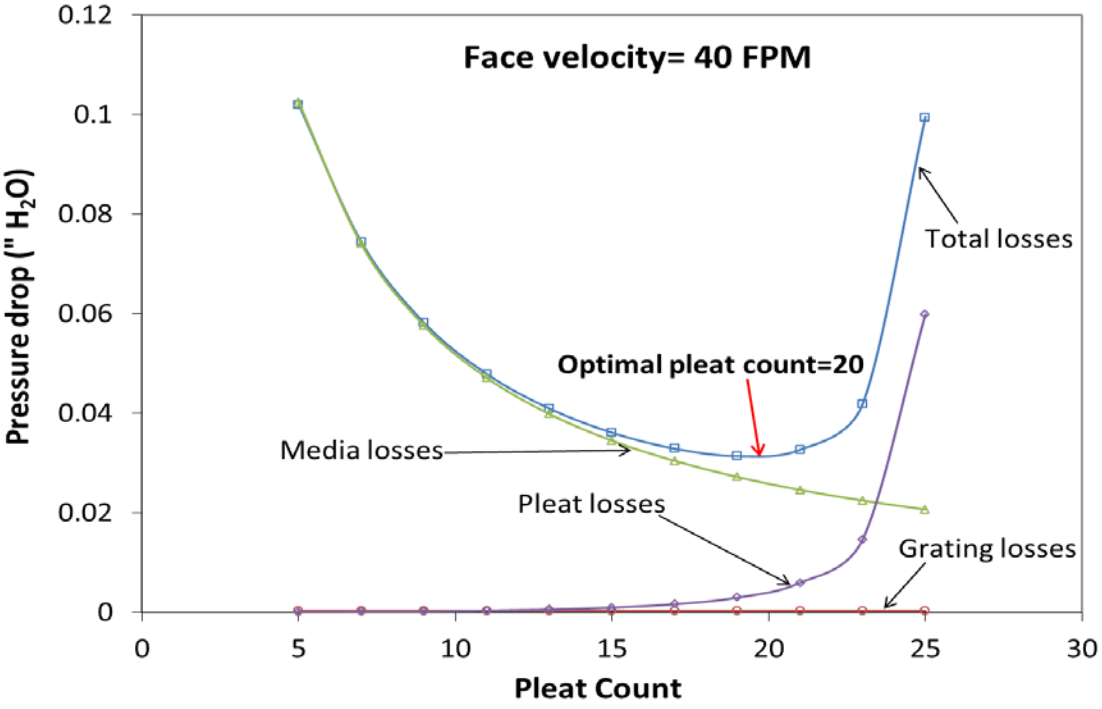

Figure V.4: Pressure drop across the pleated filter along with the individual resistances predicted by semi-empirical model [62] with respect to pleat count at face velocity of 40 FPM

Although the optimal pleat count in figure V.4 is 20, given the small dimensions of the prototype of cathode air filter under consideration (4.25″×3″×0.625″), construction of a pleated filter with 20 pleats does not look feasible. Hence, for comparing the pressure drop performance of pleated filter with the other configurations of cathode air filter; pleated filter with the pleat count of 9 was selected.

V.4 Comparison of the Pressure Drop Performances and Parasitic Power Losses for Three Configurations of Cathode Air Filter

After discussing individually the pressure drops across each of three possible configurations for cathode air filter, it was important to compare their pressure drop performances with each other to select the optimal configuration of cathode air filter. As mentioned earlier the pressure drop across cathode air filter results in increase in the parasitic power loss for PEM fuel cell system. This parasitic power loss is calculated by using equation V.9 below.

Parasitic power loss = ΔP across cathode air filter × Flow Rate of Air supplied to (Eq.V.9)
for PEMFC the cathode side of PEMFC

Pressure drop across cathode air filter can either be experimentally found or can be predicted by using the different model equations described in section V.1 and V.3. Flow rate of oxygen required to operate a fuel cell can be found by number of faradays provided by a mole of oxygen. Through substitution and simplification, the equation for the required air flow rate is derived [2] and is shown below. This equation can be used for all types of fuel cells regardless of the size as an estimate for air flow rate requirements.

Air flow rate = $1.82 \times 10^{-2} \times \lambda \times P_e / V_c$ (SLPM) (Eq.V.10)

where

λ = Stoichiometric ratio defined as the total amount of oxygen flow divided by oxygen used. A good approximation for the minimum stoichiometric ratio to operate a fuel cell is 3.

P_e = Power output of fuel cells in Watts

V_c = Average voltage across each cell in the stack. The figure of 0.65 V can be used as a good approximation for average voltage if this value is not given [2].

For Ballard's NEXA^{TM} PEMFC stack, P_e = 1200 W and substituting for $\lambda = 3$ and V_c = 0.65 V, the air flow rate required to operate this stack at full load was found to be 100 SLPM, which is equal to 1.67×10^{-3} m^3/s. The face velocity of air through the cathode air filter installed in this stack was then found by dividing the air flow rate by cross-sectional area of the filter. This face velocity was calculated to be 40 FPM.

Since cathode air filter installed in Ballard's NEXA^{TM} PEMFC stack was taken as the prototype for the cathode air filter design, volume constraints related to this prototype were taken into account while finding out the pressure drop across different configurations of the cathode air filter. The depth of this filter (0.625″) was given the most important consideration when calculating the pressure drops for different configurations. In addition to estimation of the pressure drop, parasitic power loss related with such pressure drop was also calculated for each configuration of cathode air filter.

V.4.1 Parasitic power loss for packed bed

If a packed bed configuration is selected for cathode air filter then the sorbents used in it will be of particle size range 0.85-1.4 mm. This is because use of smaller size particles results in the exceedingly high values of pressure drop and also it leads to problems of cluster formation and channeling in the packed beds. As shown in table V.1, pressure drop calculated for the particle size range of 0.85-1.4 mm by using the Ergun's equation at face velocity of 40 FPM is 0.13 ″of H_2O/cm. This was done by substituting the log mean particle size of this range for the particle diameter D_p in the Ergun's equation.

The filter depth of prototype design of cathode air filter is 0.625″ that is, 1.6 cm. Hence, the pressure drop across packed bed configuration = 0.13 ″of H_2O/cm × 1.6 cm

= 0.21 ″of H_2O = 52.3 Pa

Therefore, parasitic power loss for packed bed configuration = Air flow rate × Pressure drop

$= 1.67 \times 10^{-3}\ m^3/s \times 52.3\ Pa$

= 0.09 W

As can be seen from the above calculations, parasitic power loss caused by the pressure drop across packed bed configuration is negligible.

V.4.2 Parasitic power loss for composite bed

The composite bed configuration for the cathode air filter will consist of packed bed of large size particles (0.85-1.4 mm) followed by a thin polisher layer of polymer microfibrous media containing small size particles (180-250 microns). So, the packed bed part of this composite bed configuration will be same as the packed bed configuration mentioned in section V.4.1 and it will consist of sorbent particles of 0.85-1.4 mm size. Sheet of polymer microfibrous media described in section V.2 will be considered as the polisher layer in this composite bed configuration. Thus, this polisher layer will be microfibrous sheet of 180-250 micron sorbent particles entrapped in the matrix of 13 micron polymer fibers. As the thickness of the polisher layer here will be 2 mm, the length of the packed bed would be 1.4 cm.

Again referring back to table V.1, pressure drop across the packed bed part of the composite bed at face velocity of 40 FPM is 0.18 ″of H_2O, which is equal to 44.8 Pa. Also, the pressure drop across the polisher layer at different face velocities was found experimentally and the resultant curve is shown in figure V.2. From this figure V.2, pressure drop across the polisher layer at the face velocity of 40 FPM was found to be 0.14 ″of H_2O. So, the pressure drop across the entire composite bed configuration is calculated to be 0.32 ″of H_2O (equal to 79.7 Pa).

Therefore, parasitic power loss for composite bed configuration = 1.67×10^{-3} $m^3/s \times 79.7$ Pa

= 0.13 W

Again, it can be seen that the parasitic power loss caused by the pressure drop across the composite bed configuration is negligible.

V.4.3 Parasitic power loss for pleated filter

As mentioned in section V.3, pleated filter with the pleat count of 9 is selected for comparing the pressure drop performance of pleated filter with the other configurations of cathode air filter. Polymer microfibrous media described in section V.2 (180-250 micron sorbent particles entrapped in the matrix of 13 micron polymer fibers) will be assumed to be the filter media of the pleated air filter under consideration. Figure V.4 shows the pressure drop curve with respect to the pleat count of the pleated filter for a constant face velocity of 40 FPM. Pressure drop values in this plot were predicted by using the semi-empirical model mentioned in section V.3. From this plot, predicted pressure drop across the pleated filter with 9 pleats was found to be 0.06 ″of H_2O (equal to 15 Pa).

Therefore, parasitic power loss for pleated filter configuration = 1.67×10^{-3} $m^3/s \times 15$ Pa

= 0.02 W

Above calculations clearly show that amongst the three possible configurations of cathode air filter, parasitic power loss is predicted to be the lowest for the pleated filter configuration.

V.4.4 Selection of the optimal configuration of cathode air filter

Parasitic power losses calculated for all the three configurations of cathode air filter were found to be negligible (all of them < 0.2 W). So, it was concluded that the pressure drop across any configuration of cathode air filter is not a very significant criterion for the final selection of the optimal configuration of cathode air filter. At the same time it must be mentioned that in the absence of an adsorptive cathode air filter, drop in the output power of PEM fuel cell as a result of the exposure to various cathode air contaminants would be really huge. Thus, the cost of not having an adsorptive cathode air filter installed in the PEMFC system is much higher than the cost incurred due to additional parasitic power loss resulting from the incorporation of cathode air filter.

Two other important criteria to select the optimal configuration of cathode air filter are the breakthrough times and the high log removal efficiency of the sorbents packaged in a given configuration of the cathode air filter. Breakthrough times for different contaminants present in cathode air depend on both the particle size of the sorbent as well as the volumetric loading of the sorbents in given filter configuration. Sorbents of smaller particle size (~ 200 microns) show higher breakthrough times for the packed bed configuration because of lower intraparticle diffusion resistance in such smaller size particles. However, use of such smaller sorbent particles results in excessively high pressure drop as indicated by Ergun's equation. Hence it is assumed that the packed bed will always consist of large size particles (~ 1 mm). Polymer microfibrous media has higher contacting efficiency compared to packed bed and its use leads to a much sharper breakthrough curve and greater sorbent utilization. One drawback of MFM is the lower volumetric loading of adsorbent as compared to packed bed.

Composite bed makes the best use of the individual beneficial features of packed bed and MFM. As shown in section IV.3, significantly higher breakthrough capacity can be achieved by the use of composite bed as compared to the packed bed with little increase in the total volume of the bed. Also in case of composite bed, the polisher layer added downstream of packed bed efficiently removes low levels of contaminants by at least one more log further. Thus it is clear that the composite bed configuration will always be preferred over the packed bed configuration for cathode air filter applications.

However when it comes to the comparison of breakthrough performance of pleated filter configuration and composite bed configuration, no such comparative studies have been reported in the literature. Moreover there are not any known models mentioned in the literature that can be used to predict the breakthrough performance of the pleated air filter. So the only way to compare the breakthrough performance and high log removal efficiency of both the pleated filter and composite bed configuration is to do it experimentally. It is recommended to carry out the breakthrough experiments on the composite bed as well as the pleated filter configuration of cathode air filter before selecting the optimal configuration.

Chapter VI: Summary and Conclusions

1. Several sorbents impregnated with different transition metal oxides and caustic chemicals were tested for their SO_2 adsorption capacity to find out a high capacity sorbent for SO_2 removal, which will be used in the cathode air filters. MnO_x(SO_4 route)/Al_2O_3 prepared by deposition precipitation route with $MnSO_4$ as a precursor was found to have the highest breakthrough capacity as well as the highest saturation capacity for SO_2 removal over wide range of relative humidity (up to 75%RH) and inlet SO_2 concentrations (5-70 ppm). Oxidation state of Mn in MnO_x(SO_4 route)/Al_2O_3 varies between 3 and 4 because of non-stoichiometry characteristic of most oxides of manganese.
2. SO_2 breakthrough capacity of MnO_x(SO_4 route)/Al_2O_3 was found to increase significantly at higher moisture content of air. It was proposed that at high RH values, $MnSO_4$ formed as a product due to reaction between SO_2 and MnO_x gets dissolved in the water present in many pores of sorbent due to capillary condensation. These dissolved Mn(II) ions then act as the catalyst for SO_2 oxidation by using the oxygen dissolved in aqueous phase, which results in the observed increase in breakthrough as well as saturation capacity of MnO_x(SO_4 route)/Al_2O_3 at high values of RH.
3. PICA Activated Carbon (derived from coconut shell) showed the highest saturation capacity for NO_2 removal. However, generation of significant amount of NO was also observed during NO_2 adsorption on activated carbon. It was suspected that the surface of activated carbon acts partially as a reducing agent and converts part of NO_2 from the challenge gas to NO. $KMnO_4$/Al_2O_3 which is a strong oxidizing agent was selected as the

sorbent for NO removal as it showed the highest breakthrough capacity as well as the highest saturation capacity for NO. Addition of $KMnO_4/Al_2O_3$ to activated carbon was found to delay the appearance of NO in exit gas stream because of oxidation of NO to NO_2 by $KMnO_4$.

4. It is concluded that mixture of three different sorbents is required to remove SO_2, NO and NO_2 simultaneously from cathode air. These sorbents are
    i. $MnO_x(SO_4$ route$)/Al_2O_3$ for SO_2 removal by adsorption
    ii. PICA activated carbon for NO_2 removal by adsorption
    iii. $KMnO_4/Al_2O_3$ for NO removal by its oxidation to NO_2
5. Breakthrough times for air contaminants, high log removal efficiency and pressure drop are some of the important criteria in selecting the optimal design for cathode air filter. Different types of filter configurations were tested for their SO_2 breakthrough performance and pressure drop performance. It was found that the composite bed design increased the SO_2 breakthrough time by almost 3.4 times when compared with packed bed configuration and it was done with little increase in the volume and pressure drop of the filter.
6. Particulate air filter installed in Ballard's NEXA^{TM} PEMFC stack was taken as the prototype for the cathode air filter design and to compare the performances of different configurations of cathode air filter. Pressure drops across all the three configurations of the cathode air filter were either found experimentally or were predicted by using model equations. Parasitic power losses were then calculated for all the three configurations of cathode air filter and all of these power losses were found to be negligible (< 0.2 W). So it was concluded that the pressure drop across cathode air filter is not an important

criterion for the final selection of the optimal configuration of cathode air filter. On the other hand two more important criteria to select the optimal configuration of cathode air filter are the contaminant breakthrough times and the high log removal efficiency.

Chapter VII: Recommendations for Future Work

VII.1 Selection of the Optimal Configuration of Cathode Air Filter Installed in Ballard's NEXA^{TM} PEMFC Module

Particulate air filter installed in Ballard's NEXA^{TM} PEMFC stack is taken as the prototype for the cathode air filter design in this study. Three different design configurations of cathode air filter are discussed in section IV.1. These configurations are:

i. Particulate filter (for particulate filtration) + packed bed (for gaseous filtration) (PF+PB)
ii. Particulate filter + pleated MFM filter (for gaseous filtration) (PF+MFM)
iii. Particulate filter + composite bed (for gaseous filtration) (PF+CB)

These three configurations for the filter with the dimensions as that of the prototype need to be tested for their pressure drop and breakthrough performances. These experiments should be carried out by using a small-scale air duct as shown in figures VII.1 and VII.2. As the concentration of contaminants in cathode air is usually in sub-ppm range in many operating environments, both SO_2 and NO_x breakthrough experiments in this duct should be carried out with the inlet challenge gas concentration in the range of 1-2 ppm. These sets of breakthrough experiments along with the pressure drop measurements would give better understanding about the feasibility of using different configurations of cathode air filter for the specific applications of PEM fuel cells. Type of air contaminants and contaminant concentrations may vary greatly from one specific application to another. Lastly, such testing should help in selecting the optimal configuration of cathode air filter for PEMFCs which are operated in the distinct operating environments.

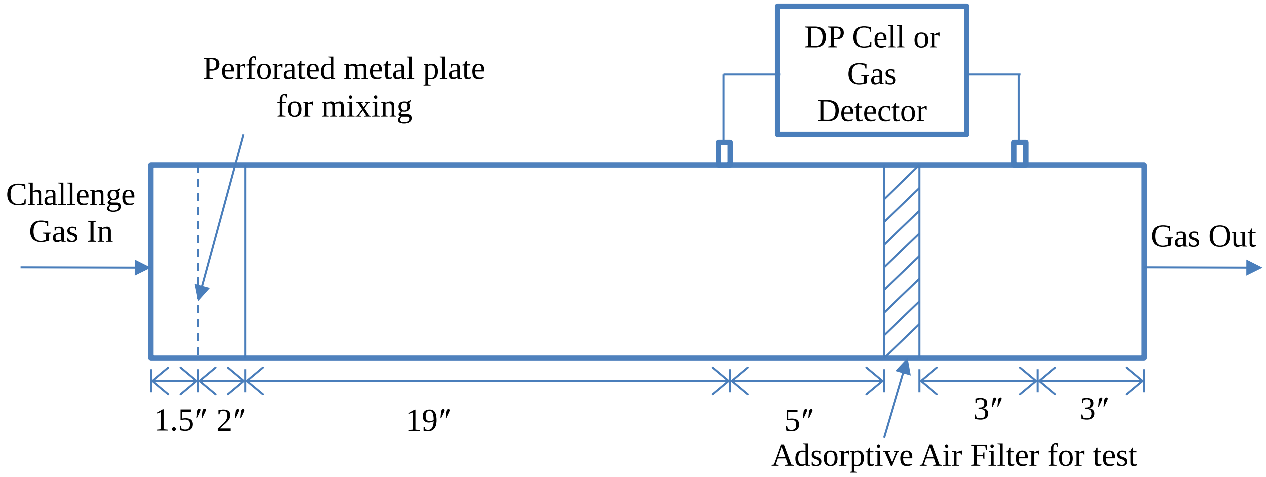

Figure VII.1: Schematic of an air duct to be used to test different cathode air filter configurations

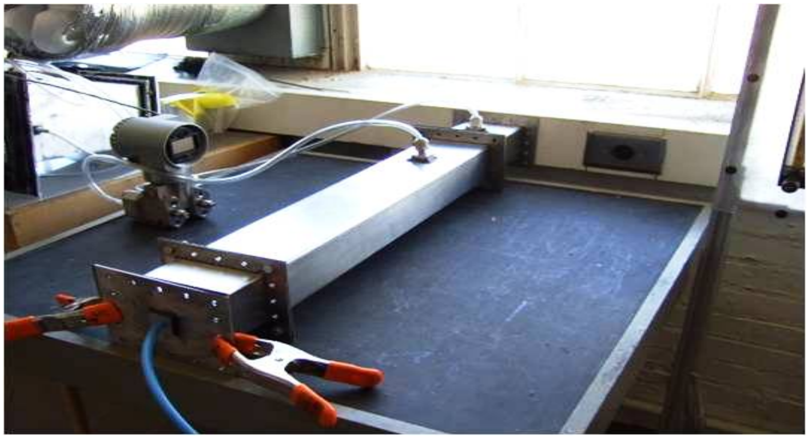

Figure VII.2: Air duct with the attached DP cell for testing different cathode air filter configurations

VII.2 Selection of Sorbents and/or Catalysts for Removal of other Cathode Air Contaminants

High capacity sorbents were developed in the present study for removal of SO_2, NO and NO_2 from cathode air. However there are other air contaminants such as VOCs and CO, which are also commonly found in many operating environments of PEMFC. Effect of these contaminants on the performance of PEMFC is not as severe as that of SO_2 and NO_x. Still exposure to these contaminants lead to a temporary drop in the output power of PEMFC and passing of clean air for some time is required to recover this drop in the performance. Hence it is necessary to have sorbents and/or catalysts in the cathode air filter to remove both VOCs as well as CO from cathode air.

Adsorption process has been found to be effective for removal of low concentration (ppm) levels of VOCs. GAC (Granular activated carbon) and ACF (Activated carbon fibers) have been widely reported in literature for their efficient removal of large number of VOCs by adsorption. Narrow microporosity of activated carbons has been found to be the most important property for controlling adsorbate uptake [69]. Also, removal of oxygen functional groups from the surface of such activated carbons was found to enhance the adsorption of benzene and toluene significantly [70]. PICA activated carbon derived from coconut shell is selected in the present study for removal of NO_2 from cathode air. The same sorbent should be tested for its adsorption capacity to remove some of the most commonly found VOCs such as toluene and benzene. It will be of great interest to know the extent to which NO_2 adsorption capacity of PICA AC will be affected if this sorbent is selected for VOC removal also. In addition to this sorbent, several other commercially available sorbents should also be tested before selecting a high capacity sorbent for VOC removal from cathode air.

Catalytic oxidation of CO to CO_2 is the most viable option for CO removal at ambient conditions. Some of the well-known CO oxidation catalysts available commercially are Carulite® (CuO_x–MnO_x catalyst from Carus Chem.), Aurolite® (Au/TiO_2 from Strem Chemicals) and NanAuCat^{TM} (a nano-gold catalyst from 3M). These catalysts should be tested for their CO oxidation activity at room temperature and for different RH of air, to select a catalyst for effective removal of CO from cathode air. However it should be kept in mind that negative effect of CO from cathode air on the performance of PEMFC is minor (4% drop in the power output after exposure to 20 ppm CO for 15 minutes [8]) and such small drop in the performance of PEMFC can be recovered by passing contaminant-free clean air. So before placing one of these commercial CO oxidation catalysts in the cathode air filter, its economic feasibility must be considered.

VII.3 Performance Evaluation of Cathode Air Filter Prototype on Actual PEM Fuel Cell Stack

Once the optimal configuration of cathode air filter prototype (which is installed in Ballard's NEXA^{TM} PEMFC module) is decided, its overall performance should be evaluated on one of the actual PEM fuel cell stacks. The performance of this cathode air filter prototype can be defined in terms of few parameters such as pressure drop, time length for which there is no significant drop in the output power of PEMFC stack etc. For such kind of performance evaluation, the prototype should be connected to the cathode inlet of the stack and a simulated air contaminated with few ppms (or several ppbs) of SO_2 and NO_x should be passed through filter and then to the stack. Testing of the prototype on actual PEM fuel cell stack will give much clearer idea about the performance of cathode air filter in real-life applications.

References

1. Cacciola G., Antonucci V., Freni S., Journal of Power Sources, 100(2001), 67-69.
2. Larminie J., Dicks A., Fuel cell system explained, Second edition, Wiley: England, 2003, 14-17.
3. Litster S., McLean G., Journal of Power Sources, 130(2004), 61-76.
4. Jing F., Hou M., Shi W., Fu J., Yu H., Ming P., Yi B., Journal of Power Sources,166:1(2007), 172-176.
5. Mohtadi R., Lee W.K., Zee J.W., Journal of Power Sources, 138(2004), 216-225.
6. Yang D., Ma J., Xu L., Wu M., Wang H., Electrochimica Acta, 51(2006), 4039-4044.
7. Nagahara Y., Sugawara S., Shinohara K., Journal of Power Sources, 182:2(2008), 422-428.
8. Moore J.M., Adlock P.L., Lakeman J.B., Mepsted G.O., Journal of Power Sources, 85(2000), 254-260.
9. Kennedy D.M., Cahela D.R., Zhu W.H., Westrom K.C., Nelms R.M., Tatarchuk B.J., Journal of Power Sources, 168(2007), 391-399.
10. Exposure Investigation Report, Weyerhaeuser Pulp & Paper Mill, Plymouth NC,March 22, 2007 ,U.S. Department Of Health and Human Services.
11. Minoura H., Ito A., Proceedings of seventh international conference on urban climate,29 June-3 July 2009, Yokohoma, Japan.
12. Fogler H.S., Elements of Chemical Reaction Engineering, Third edition, Prentice Hall of India: New Delhi, 2004, 154-155.

13. Tatarchuk B.J., Rose M.F., Krishnagopalan A., Zabasajja J.N., Kohler D., US Patent 5,096,663,March 17, 1992.
14. Tatarchuk B.J., Rose M.F., Krishnagopalan A., Zabasajja J.N., Kohler D., US Patent 5,080,963,January 14, 1992.
15. Harris D.K., Cahela D.R., Tatarchuk B.J., Composites: Part A, 32(2001), 1117-1126.
16. Wieckowska J., Catalysis today, 24(1995), 405-465.
17. Lin Y. S., Deng S.G., Separation and Purification Technology, 13(1998), 65-77.
18. Jeong S.M., Kim S.D., Ind. Eng. Chem. Res., 36(1997), 5425-5431.
19. Bueno-Lopez A., Garcia-Martinez J., Garcia-Garcia A., Linares-Solano A., Fuel, 81(2002), 2435-2438.
20. Lizzio A.A., DeBarr J.A., Energy & Fuels, 11(1997), 284-291.
21. Zhang P., Wanko H., Ulrich J., Chem. Eng. Technol., 30(2007), 635-641.
22. Martin C., Perrard A., Joly J.P., Gaillard F., Delecroix V., Carbon, 40 (2002), 2235-2246.
23. Lee Y.W., Park J.W., Choung J.H., Choi D.K., Environ. Sci. Technol., 36(2002), 1086-1092.
24. Fortier H., Zelenietz C., Dahn T.R., Westreich P., Stevens D.A., Dahn J.R., Applied Surface Science., 253(2007), 3201-3207.
25. Guo J., Lua A.C., Separation and Purification Technology, 30(2003), 265-273.
26. Davini P., Carbon, 39 (2001), 419-424.
27. Carabineiro S.A.C., Ramos A.M., Vital J., Loureiro J.M., Orfao J.J.M., Fonseca I.M., Catalysis Today, 78 (2003), 203-210.
28. Karge H.G., Lana I.D., J. Phys. Chem., 88(1984), 1538-1543.
29. Chang C.C., Journal of Catalysis, 53(1978), 374-385.

30. Nam S.W., Gavalas G.R., Applied Catalysis, 55(1989), 193-213.
31. Rao S.N.R., Waddell E., Mitchell M.B., White M.G., Journal of Catalysis, 163(1996), 176-185.
32. Mitchell M.B., Sheinker V.N., White M.G., Journal of Catalysis, 163(1996), 176-185.
33. Iannicelli J., US Patent 5,112,796, May 12, 1992.
34. Bienstock D., Field J.H., US Patent 3,150,923, September 29, 1964.
35. Kohler G.A., Anders L.W., US Patent 4,133,309, January 9, 1979.
36. Hammel C.F., Tuzinski P.A., Boren R.M., US Patent 2003/0219368 A1, November 27, 2003.
37. Tikhomirov K., Krocher O., Elsener M., Widmer M., Wokaun A., Applied Catalysis B: Environmental, 67 (2006), 160–167.
38. Takashi I., Barnes H.M., Atmospheric Environment, 18:1(1984), 145-151.
39. Huss A., Lim P.K., Eckert C.A., The Journal of Physical Chemistry, 86:21(1982), 4224-4228.
40. Matteson M.J., Stober W., Luther H., Ind.Eng.Chem.Fundamen., 8:4(1969), 677-687.
41. Berglund J., Elding L.I., Atmospheric Environment, 29:12(1995), 1379-1391.
42. Yang R.T., Gas Adsorption by Adsorption Processes, Imperial College Press: London, 2008, 10-11.
43. Ho T.C., White B.S., Chem.Eng.Sci., 46(1991), 1861-1863.
44. Akosman C., Walters J.K., Chem.Eng.Process, 43(2004), 181-185.
45. Kalluri R.R., Cahela D.R., Tatarchuk B.J., Separation and Purification Technology, 62(2008), 304-316.
46. Matsumato J., Kosugi N., Nishiyama A., Isozaki R., Sadanaga Y., Kato S., Bandow H., Kajii Y., Atmospheric Environment, 40(2006), 3230-3239.

47. Muller C., England W., ASHRAE Journal, 37:2 (1995), 24-31.
48. Zhang W., Bagreev A., Rasouli F., Ind.Eng.Chem.Res., 47(2008), 4358-4362.
49. Pietrzak R., Energy & Fuels, 23(2009), 3617-3624.
50. Jeguirim M., Tschamber V., Brilhac J.F., Ehrburger P., J. Anal. App. Pyrolysis , 72(2004), 171-181.
51. Zawadzki J., Wisniewski M., Skowronska K., Carbon, 41(2003), 235-246.
52. Lee M.R., Allen E.R., Wolan J.T., Hoflund G.B., Ind.Eng.Chem.Res., 37(1998), 3375-3381.
53. Technical note TN-114 from RAE systems: Sensor specifications and cross-sensitivities.
54. Bosch H., Janssen F., Catal. Today, 2(1988), 369-379.
55. Armor J., Applied Catalysis B: Environmental, 1(1992), 221-256.
56. Kijlstra W., Biervliet M., Poels E., Bliek A., Applied Catalysis B: Environmental, 16(1998), 327-337.
57. Guo Z., Xie Y., Hong I., Kim J., Energy Conversion and Management, 42(2001), 2005-2018.
58. Mochida I., Kawabuchi Y., Kawano S., Matsumura Y., Fuels, 76:6(1997),543-548.
59. Mochida I., Kisamori S., Hironaka M., Kawano S., Matsumara Y., Yoshikawa M., Energy and fuels, 8(1994), 1341-1344.
60. Uchida S., Kobayashi T., Kageyama S., Ind. Eng. Chem. Process Des. Dev., 22(1983), 323-329.
61. Cahela D.R., Tatarchuk B.J., Catalysis Today, 69(2001), 33-39.
62. Karwa A.N., Tatarchuk B.J., Separation and Purification Technology, 86 (2012), 55–63.

63. Carman P.C., Flow of gases through porous media, Butterworths Scientific Publications, 1956.
64. Rivers D.R., Murphy D.J., ASHRAE Transactions, 106:2 (2000), 131-144.
65. Scheidegger A., The Physics of Flow through Porous Media, Third edition, University of Toronto Press: Toronto, 1974.
66. Sothen R.A., Tatarchuk B.J., HVAC&R Research, 14:6(2008), 841-860.
67. Del Fabbro L., Laborde J.C., Merlin P., Ricciardi L., Filtration and Separation, 39:1(2002), 34-40.
68. Tronville P., Sala R., HVAC&R Research, 9:1(2003), 95-106.
69. Marsh H., Rodriguez-Reinoso F., Activated Carbon, First edition, Elsevier, 2006.
70. Lillo-Rodenas M.A., Cazorla-Amoros D., Linares-Solanao A., Carbon, 43:8(2005), 1758-1767.
71. Yoon Y.H., Nelson J.H., Am. Ind. Hyg. Assoc. J., 45:8(1984), 509-516.
72. Yoon Y.H., Nelson J.H., Am. Ind. Hyg. Assoc. J., 45:8(1984), 517-524.

Appendix A: Calculation of Breakthrough Capacity and Saturation Capacity

1. Breakthrough capacity

SO_2 breakthrough capacity of an adsorbent in mg/g

$$= \frac{\left(volumetricflowrateofSO_2 \left(\frac{m^3}{\min} \right) \times \left(\frac{P}{RT} \right) \left(\frac{mol}{m^3} \right) \times breakthroughtime(\min) \times MWofSO_2 \left(\frac{g}{mol} \right) \times 10^3 \left(\frac{mg}{g} \right) \right)}{Wt.ofsorbent(g)}$$

Same formula can be used to calculate the breakthrough capacity for any other adsorbate by substituting the corresponding value of molecular weight of that adsorbate.

2. Saturation Capacity

The shape of the breakthrough curve decides the method that can be used to calculate saturation capacity of the sorbent. Since some breakthrough curves in the present work do not have the perfect sigmoidal shape (S-shape), $t_{1/2}$ method cannot be used here to calculate the saturation capacity. The method used here to calculate the saturation capacity involves finding the approximate area under the breakthrough curve using numerical integration.

Typical breakthrough curve is shown in figure A.1. Area under the breakthrough curve from the time of breakthrough ($t_{breakthrough}$) till the time of saturation ($t_{saturation}$) is the cumulative amount of challenge gas coming out of the adsorbent bed. Thus, this area indicates the quantity of challenge gas that has not been adsorbed on the adsorbent. Region corresponding to this area on the breakthrough plot in figure A.1 is marked with the lines. Region of the plot in figure A.1 that is confined between c/c_0 from o to 1 on y axis, time (t) from 0 to $t_{saturation}$ on x axis and area lying above the breakthrough curve, gives the amount of challenge gas that has been adsorbed on the sorbent. This region has been highlighted on the breakthrough plot in figure A.1. Area of this region needs to be found to calculate the saturation capacity. So firstly, area under the breakthrough curve bound between time t=0 and $t=t_{saturation}$ is calculated approximately by using trapezoidal rule.

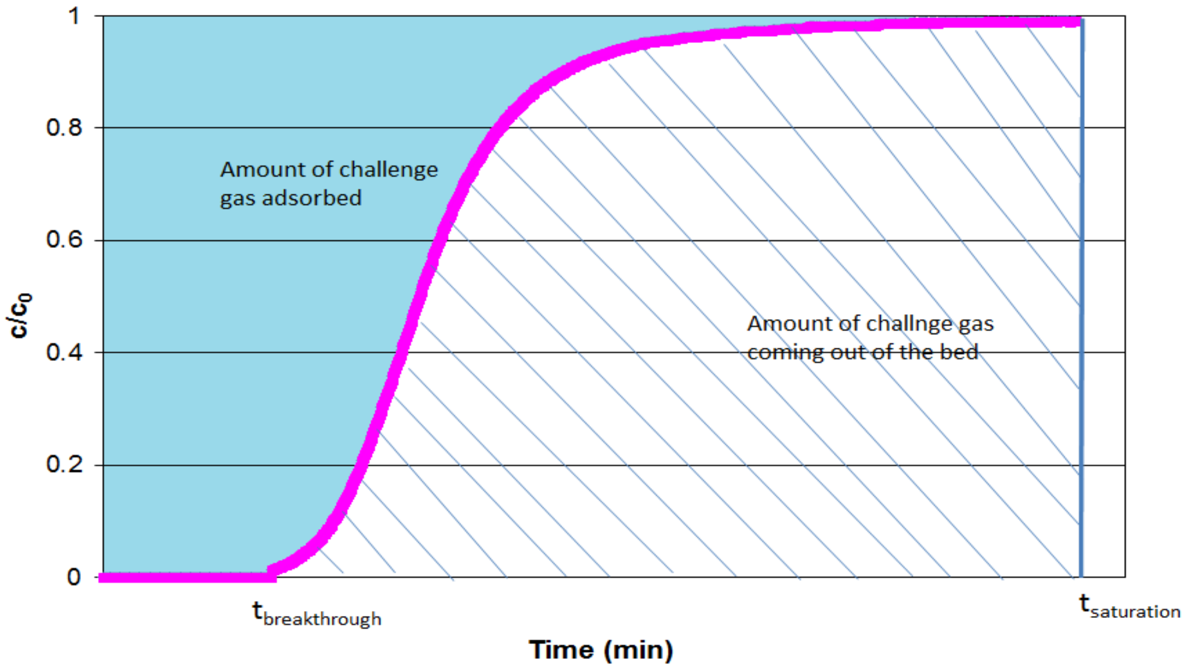

Figure A.1: Saturation capacity calculations demonstrated with a typical breakthrough curve

Trapezoidal rule is a technique in numerical analysis for approximating the definite integral. The trapezoidal rule works by approximating the region under the curve for the function $f(x)$ as a trapezoid and calculating its area. Therefore area under the curve between points a and b is calculated as,

$$\int_a^b f(x)dx \approx (b-a)\frac{f(a)+f(b)}{2} \qquad \text{(Eq. A.1)}$$

For a domain discretized into N equally spaced intervals or N+1 grid points (1, 2, ..., N+1), where the grid spacing is $h=(b-a)/N$, the approximation for definite integral becomes

$$\int_a^b f(x)dx \approx \frac{h}{2}\sum_{k=1}^{N}\left(f(x_{k+1})+f(x_k)\right)=\frac{b-a}{2N}\left(f(x_1)+2f(x_2)+2f(x_3)+\ldots+2f(x_N)+f(x_{N+1})\right)$$

… (Eq. A.2)

Since in the present study outlet concentration of challenge gas measured by the multigas detector is recorded at a fixed predefined data logging interval, above approximation for the definite integration can be used. In this case, b = $t_{saturation}$, a=0 and N is the time interval for data logging. Each of f(x) represents the outlet concentration of challenge gas at the time t=x. c/c_0 = 0.95 is chosen as the upper limit for the outlet concentrations by assuming that the sorbent is practically saturated at this point.

As all the relevant data is available, equation A.2 can be used to calculate the area under breakthrough curve approximately. Unit of this calculated area is ppm-min. This area is then subtracted from the cumulative amount of challenge gas that has been introduced into the sorbent bed till the saturation point. This subtraction gives the amount of challenge as adsorbed till the saturation point in the units of ppm-min. Thus at the saturation point,

Total amount of gas adsorbed = Total amount of gas introduced - Total amount of gas that has
(ppm-min) in the bed (ppm-min) come out the bed (ppm-min)

= $c_0 \times t_{saturation}$ - Area under the breakthrough curve calculated by trapezoidal rule

Amount of gas adsorbed found from above equation is then used in the final equation to calculate the saturation capacity.

SO_2 saturation capacity of an adsorbent in mg/g

$$=\frac{\left(QtyofSO_2adsorbed(ppm-\min)\times volumetricflowrateofgas\left(\frac{lit}{\min}\right)\times 10^{-6}\times MWofSO_2\left(\frac{g}{mol}\right)\times 10^{3}\left(\frac{mg}{g}\right)\right)}{\left(\frac{RT}{P}\right)(\frac{m^3}{mol})\times Wt.ofsorbent(g)\times 10^{3}\left(\frac{lit}{m^3}\right)}$$

Pressure and temperature values at STP conditions are used (P= 100 kPa, T= 273.15 K) to calculate both the breakthrough capacity and saturation capacity. SO_2 is used just as an example here and the above equation is applicable to any other adsorbate.

Notations:

P - Pressure (Pa)

R - Universal gas constant (8.314 J/mol K)

T - Temperature (K)

MW - Molecular weight (g/mol)

$t_{breakthrough}$ - Breakthrough time (min)

$t_{saturation}$ - Saturation time (min)

c_o - Challenge gas concentration at the inlet (ppmv)

Appendix B: Adsorption Kinetic Parameters of Sorbents Tested for SO_2 Removal

Gas adsorption kinetic parameters of an adsorbent give information about the adsorption rates in the particles of sorbent and hence they are important to compare the breakthrough performance of different sorbents. Bed depth service time equation developed by Yoon and Nelson [71, 72] was used here to determine adsorption kinetics parameters k and τ. This equation is shown below

$$t = \tau + \frac{1}{k}\ln\left(\frac{C_b}{C_0 - C_b}\right) \qquad \text{--- (Eq.B.1)}$$

where,

t = Breakthrough time (min)

τ = Time required for 50% contaminant breakthrough (min)

k = Lumped adsorption rate constant (min^{-1})

C_b = Breakthrough concentration of contaminant (ppm)

C_0 = Challenge concentration of contaminant (ppm)

Large value of k indicates the faster adsorption kinetics which results in the sharper breakthrough curve. On the other hand, low value of k shows more sluggish nature of breakthrough curve. Thus parameter k gives an idea about the shape of the breakthrough curve. Parameter τ is directly related to saturation capacity of adsorbent. Large value of τ indicates higher saturation capacity and vice a versa. Hence, τ gives an idea about the position of the breakthrough curve. Bed depth service equation was applied to breakthrough curves of all the sorbents which are shown in figures II.2 and II.3. k and τ for these sorbents along with their breakthrough and saturation capacities are shown in table B.1. These values of k and τ are valid for only those operating at which corresponding breakthrough experiments were carried out. It is because both k and τ are dependent on the flow rate and the concentration of challenge gas.

Table B.1. Adsorption capacities and kinetic parameters of all sorbents tested for SO_2 removal

Sorbent(All sorbents supported on γ-Al_2O_3)	**Breakthrough Capacity at $c/c_0=0.02$ (mg of SO_2/cc)**	**Saturation Capacity (mg of SO_2/cc)**	**k (min^{-1})**	**τ (min)**
Fe Oxide(6.7 wt% Fe)	8.2	19.2	0.42	16.4
Cu Oxide (6.7 wt% Cu)	10.7	28.6	0.21	24.6
4 wt% $KMnO_4$	11.5	70.7	0.022	94.9
MnO_x prepared by $Mn(NO_3)_2$ Route (6.7 wt% Mn)	13.4	78	0.028	83.9
Ni Oxide (6.7 wt% Ni)	13.5	35.7	0.11	35.6
Zn Oxide (6.7 wt% Zn)	14.2	30.6	0.31	25.4
Campure 6XL commercial sorbent (6 wt % $KMnO_4$)	23.1	77.3	0.047	75.8
10 wt% KOH	29.8	52.2	0.16	44.5
MnO_x prepared by $MnSO_4$ Route (6.7 wt% Mn)	33.7	124.1	0.027	127.8

As can be seen from the table B.1, sorbents impregnated with MnO_x and $KMnO_4$ have high saturation capacity for SO_2 (large τ) but their breakthrough curves are sluggish in nature (small k). On the other hand KOH/Al_2O_3 has lower saturation capacity for SO_2 (small τ) but it shows sharper breakthrough curve (large k).

Appendix C: Details of the Gas Detectors Used to Measure Challenge Gas Concentrations

1. SO_2 Electrochemical Sensor installed in the GasAlertMicro5 Multi-gas Detector

Performance Characteristics

Nominal Range	0-20 ppm
Maximum Overload	150 ppm
Expected Operating Life	Two years in air
Output Signal	0.5 ± 0.1 µA/ppm
Resolution	0.1ppm
Temperature Range	-20^{o}C to +50^{o}C
Pressure Range	Atmospheric ± 10%
T90 Response Time	<75 seconds
Relative Humidity Range	15 to 90% non-condensing
Long Term Output Drift	<2% signal loss/month
Recommended Load Resistor	10 Ω
Bias Voltage	Not required
Repeatability	<2% of signal
Output Linearity	Linear

2. NO_2 Electrochemical Sensor installed in the GasAlertMicro5 Multi-gas Detector

Performance Characteristics

Nominal Range	0-20 ppm
Maximum Overload	150 ppm
Expected Operating Life	Two years in air
Output Signal	0.6 ± 0.15 μA/ppm
Resolution	0.1ppm
Temperature Range	$-20^{o}C$ to $+50^{o}C$
Pressure Range	Atmospheric ± 10%
T90 Response Time	<25 seconds
Relative Humidity Range	15 to 90% non-condensing
Long Term Output Drift	<2% signal loss/month
Recommended Load Resistor	33 Ω
Bias Voltage	Not required
Repeatability	<2% of signal
Output Linearity	Linear

3. PFPD (Pulsed Flame Photometric Detector) installed in GC used to Detect SO_2

Gas Chromatography Model	Varian CP3800
Column	Restek XTI (30mm×0.25mm×0.5µm)
Oven Temperature Program: 60^oC for 1 min, Ramp to 90^oC at the rate of 20^oC/min and stay at 90^oC for 3.5 min. Total runtime is 6 minutes.	
Injector Temperature	80^oC
Air Flow Rate	17 cm^3/min
H_2 Flow Rate	13 cm^3/min
Split Ratio	200
Tube Voltage	510 V
Trigger level	200 mA
Sample Delay	4 ms
Sample Width	10 ms
Gain Factor	2
Syringe Size	250 µL

4. Calibration curve for SO_2 concentration measured by using PFPD installed on Varian CP3800